

PAULO ROBERTO REFACHINHO DE CAMPOS

**A rigid body and a master-master contact formulation for multibody railway
applications**

São Paulo
2018

PAULO ROBERTO REFACHINHO DE CAMPOS

A rigid body and a master-master contact formulation for multibody railway applications

Dissertation presented to the Graduate Programme in Civil Engineering at Escola Politécnica da Universidade de São Paulo to obtain the degree of Master of Science.

Area of concentration: Engineering of Structures.

Advisor: Prof. Dr. Alfredo Gay Neto

São Paulo

2018

Autorizo a reprodução e divulgação total ou parcial deste trabalho, por qualquer meio convencional ou eletrônico, para fins de estudo e pesquisa, desde que citada a fonte.

Este exemplar foi revisado e corrigido em relação à versão original, sob responsabilidade única do autor e com a anuência de seu orientador.

São Paulo, _____ de _____ de _____

Assinatura do autor: _____

Assinatura do orientador: _____

Catálogo-na-publicação

Refachinho de Campos, Paulo Roberto

A rigid body and a master-master contact formulation for multibody railway applications / P. R. Refachinho de Campos -- versão corr. -- São Paulo, 2018.

136 p.

Dissertação (Mestrado) - Escola Politécnica da Universidade de São Paulo. Departamento de Engenharia de Estruturas e Geotécnica.

1.Contact 2.Master-master 3.Multibody systems 4.Wheel-rail
I.Universidade de São Paulo. Escola Politécnica. Departamento de Engenharia de Estruturas e Geotécnica II.t.

ACKNOWLEDGEMENTS

I am grateful for all the support provided by Professor Alfredo Gay Neto, who has motivated my pursuit of knowledge since we first met several years ago. Without this, I wouldn't have started myself in the field of computational mechanics and probably, I wouldn't have received so many opportunities in my career.

In addition, I would like to thank Vale S.A. for the financial support through the Wheel-Rail Chair project and Altair Brazil for providing full access to the HyperWorks suite.

ABSTRACT

In computer simulation the term “multibody system” is usually employed to describe a system of interconnected bodies. Several examples of multibody systems can be found in railway engineering. A wheelset interacting with a track through a contact interface is just one example of practical interest. Modelling mechanical systems in a virtual environment contributes to the understanding of subjects such as dynamic behaviour, stability, durability, wear, fatigue, etc. In the context of a rigid-flexible multibody system mathematically described by a weak-form, the purpose of the present work is to evaluate the contributions due to rigid bodies considering their contact interactions. Inertial contributions due to distribution of mass of a rigid body are fully developed, considering a general pole position associated with a single node, representing a rigid body element. Rodrigues rotation parameters are used to describe finite rotations, by an updated Lagrangian description. Then, the so-called master-surface to master-surface contact formulation is adapted to be used in conjunction with the rigid body element and flexible bodies, aiming to consider their interaction in a rigid-flexible multibody environment. New surface parameterizations are proposed to establish contact pairs, permitting pointwise interaction in a frictional scenario. The proposed formulation is used to represent mechanical systems from different contexts, including a numerical example of the wheel-rail contact interface. The obtained results show the robustness and applicability of the methods.

Keywords: Contact. Master-master. Multibody systems. Wheel-rail.

RESUMO

Em simulação computacional o termo “sistema multicorpos” é usualmente empregado para descrever um sistema de corpos interconectados. Diversos exemplos de sistemas multicorpos podem ser encontrados no campo da engenharia ferroviária. Um rodeiro interagindo com a via através de uma interface de contato é apenas um dos exemplos de interesse prático. A modelagem de sistemas mecânicos em um ambiente virtual contribui para o entendimento de assuntos como comportamento dinâmico, estabilidade, durabilidade, desgaste, fadiga, etc. No contexto de um sistema multicorpos rígido-flexível descrito matematicamente por uma forma fraca, o propósito do presente trabalho é avaliar as contribuições devido à presença de corpos rígidos considerando interações de contato. Contribuições inerciais devido à distribuição de massa do corpo rígido são desenvolvidas e apresentadas em totalidade, considerando um polo genérico associado a um único nó, representando o corpo rígido. Parâmetros de rotação de Rodrigues são usados para descrever rotações finitas em uma descrição Lagrangiana atualizada. A formulação de contato *master-surface to master-surface* é adaptada para ser usada em conjunto com o elemento de corpo rígido e corpos flexíveis, estabelecendo a interação entre esses corpos em um ambiente de simulação multicorpos. Novas parametrizações de superfícies de contato são desenvolvidas para estabelecer os pares de contato, assumindo-se interações pontuais, em um cenário de contato com atrito. A formulação proposta é usada para representar sistemas mecânicos em diferentes contextos, incluindo um exemplo numérico do caso de contato roda-trilho. Os resultados obtidos mostram a robustez e a aplicabilidade dos métodos.

Palavras-chave: Contato. *Master-master*. Sistemas multicorpos. Roda-trilho.

LIST OF FIGURES

Figure 2.1: Typical wheelset configuration.	25
Figure 2.2: Typical bogie configurations: (a) Primary suspension. (b) Secondary suspension.	26
Figure 2.3: Typical section of a track.	27
Figure 2.4: Track segments.	27
Figure 2.5: The main regions of wheel profiles.	28
Figure 2.6: Detailed wheel profile.	29
Figure 2.7: Detailed rail profile.	30
Figure 2.8: Typical contact positions.	31
Figure 2.9: Relationship between traction and creep.	33
Figure 3.1: Contact in finite deformation context.	38
Figure 3.2: Bodies getting in touch.	39
Figure 3.3: Convex definition: (a) Convex region. (b) Non-convex region.	40
Figure 3.4: Contact path over the master-surface.	44
Figure 3.5: Contact normal force x normal gap.	45
Figure 3.6: Coulomb's friction law.	46
Figure 3.7: Parameterized surfaces candidate to contact.	49
Figure 3.8: Parameterized surfaces candidate to contact in the configuration " $i + 1$ ".	52
Figure 4.1: Rigid body movement in a three-dimensional space.	55
Figure 4.2: Centre of mass of a rigid body.	59
Figure 4.3: Arbitrary "pilot point".	63
Figure 4.4: Rigid body (a) Reference configuration " r " (b) Deformed configuration " i " (c) Deformed configuration " $i + 1$ ".	67
Figure 4.5: Rigid node set constraint typical usage ("spider").	73
Figure 4.6: Example 4.1 - Spinning top.	76
Figure 4.7: Example 4.1 - Trajectory of the centre of mass.	77
Figure 4.8: Example 4.1 - Kinematic information.	78
Figure 4.9: Example 4.1 - Mechanical energy and angular momentum magnitude. ...	79
Figure 4.10: Example 4.2 - (a) Front view of the double pendulum. (b) Isometric view of the double pendulum.	80
Figure 4.11: Example 4.2 - Global X displacements.	81

Figure 4.12: Example 4.2 - Global Y displacements.....	82
Figure 4.13: Example 4.2 - Angular speed around global Z axis.	82
Figure 5.1: (a) An example of an extruded arc. (b) An example of a revolved arc.....	84
Figure 5.2: A 2D arc defined in a local coordinate system.	85
Figure 5.3: (a) A profile composed by a set of extruded arcs. (b) A revolved surface composed by a set of arcs.....	86
Figure 5.4: Example 5.1 - Global overview of the model.	89
Figure 5.5: Example 5.1 - (a) Contact arc for rigid floor. (b) Contact arcs for ball.....	90
Figure 5.6: Example 5.1 - Trajectory of the centre of mass.	93
Figure 5.7: Example 5.1 - Kinetic energy and angular momentum magnitude.	93
Figure 5.8: Example 5.1 - Contact forces.	94
Figure 5.9: Example 5.2 - Overhead conveyor.	95
Figure 5.10: Example 5.2 - (a) Contact arc for I-beam. (b) Contact arc for wheel.	97
Figure 5.11: Example 5.2 - Global deformation of the guide rail.....	99
Figure 5.12: Example 5.2 - Conveyor kinematics.	99
Figure 5.13: Example 5.2 - Conveyor energy and linear momentum magnitude (main body plus wheels).....	100
Figure 5.14: Example 5.2 - Contact forces magnitudes (left wheel).	100
Figure 6.1: Hunting phenomenon.	101
Figure 6.2: Hunting scenarios.....	102
Figure 6.3: Model degrees of freedom.	102
Figure 6.4: Time evolution of lateral displacements y for an initial lateral offset of 0.01m. Below critical speed: $V = 30.0$ m/s.	105
Figure 6.5: Time evolution of lateral displacements y for an initial lateral offset of 0.01m. At critical speed: $V = 74.26$ m/s.	106
Figure 6.6: Time evolution of lateral displacements y for an initial lateral offset of 0.01m. Above critical speed: $V = 75.0$ m/s.....	106
Figure 6.7: Nonlinear model: (a) General overview of wheelset model. (b) Wheel profile dimensions.	107
Figure 6.8: Frictional behaviour. (a) Coulomb's law. (b) Coulomb's law in a penalty approach.	109
Figure 6.9: Nonlinear model response: time evolution of lateral displacements for different tangential penalty factors. Speed: 15.0 m/s.....	110
Figure 6.10: Nonlinear model response: time evolution of lateral displacements for $\epsilon T = 3.6e+007$ N/m. Speed: 15.0 m/s.	111
Figure 6.11: Wheelset example - Global overview of the model.....	112

Figure 6.12: Wheelset example – contact arcs for wheel.	114
Figure 6.13: Wheelset example – contact arcs for rail.....	115
Figure 6.14: Wheelset example – contact detection.....	119
Figure 6.15: Wheelset example – contact detection.....	120
Figure 6.16: Wheelset example – lateral position of centre of mass.	121
Figure 6.17: Wheelset example – contact normal force for the right side.....	122
Figure 6.18: Wheelset example – contact normal force for the left side.	123

LIST OF TABLES

Table 4.1: Example 4.2 - Global coordinates of points.	80
Table 5.1: Example 5.1 - Global coordinates of points.	89
Table 5.2: Example 5.1 - Local coordinates of contact arcs.	90
Table 5.3: Example 5.1 - Force time history.	91
Table 5.4: Example 5.2 - Global coordinates of points.	95
Table 5.5: Example 5.2 - Local coordinates of contact arcs.	97
Table 6.1: Railway wheelset properties.	103
Table 6.2: Nonlinear models.	109
Table 6.3: Wheelset example - Global coordinates of points.	113
Table 6.4: Wheelset example - Local coordinates of contact arcs for wheel.	115
Table 6.5: Wheelset example - Local coordinates of contact arcs for rail.	116
Table 6.6: Wheelset example - Force time history.	117

CONTENTS

1. INTRODUCTION	18
1.1. Motivation.....	18
1.2. Research objective.....	21
1.3. The GIRAFFE project.....	22
1.4. Outline.....	23
2. BASIC CONCEPTS OF RAILWAY SYSTEMS	25
2.1. Global overview.....	25
2.2. Wheel and rail geometry	28
2.3. Wheel-rail contact.....	30
3. COMPUTATIONAL CONTACT MECHANICS	35
3.1. Introduction and historical background.....	35
3.2. Contact kinematics	38
3.2.1. Normal contact in three-dimensional bodies.....	38
3.2.2. Tangential contact in three-dimensional bodies.....	43
3.3. Constitutive equations for contact	44
3.4. Contact constraint enforcement	47
3.5. Master-surface to master-surface contact formulation	47
4. RIGID BODY ELEMENT FORMULATION	54
4.1. Inertial contribution.....	54
4.2. Rigid node set constraint.....	66
4.3. External field loading on the rigid body element.....	73
4.4. Numerical Examples	75
5. PARAMETERIZATION OF SURFACES	84
5.1. Extruded rigid or flexible contact surface.....	86
5.2. Revolved rigid contact surface	87
5.3. Numerical Examples	88
6. RAILWAY CASE	101
6.1. Hunting phenomenon	101
6.1.1. Analytical model for hunting.....	103
6.1.2. Nonlinear simplified model for hunting.....	107
6.2. Wheelset example.....	111

7. SUMMARY AND OUTLOOK.....	124
A. APPENDIX: VECTORS AND TENSORS.....	127
B. APPENDIX: RODRIGUES ROTATION TENSOR.....	130

NOMENCLATURE

In the present work, the following nomenclature is employed: bold lowercase Latin or Greek letters are used to represent vectors in 3-dimensional Euclidean space or column matrices (e.g.: \mathbf{u} , $\boldsymbol{\alpha}$); bold uppercase Latin or Greek letters are used to represent second order tensors in 3-dimensional Euclidean space or matrices with distinct line and columns dimensions (e.g.: \mathbf{Q} , $\boldsymbol{\Xi}$). Scalars are represented by non-bold Latin or Greek letters (e.g.: k , T , α).

The Leibniz's notation for differentiation is used throughout this work, i.e., the differential operator $\frac{d}{d\Box}$ is used. The symbol ∂ is used for partial derivatives. For the case of derivatives with respect to time, the Newton's notation is also used ($\dot{\Box}$). Variations of any quantity are represented by $\delta\Box$ and the consistent linearization of any quantity is represented by $\Delta\Box$.

Every time that a right-superscript “ r ” appears with a quantity, it is implied that this quantity is associated with a reference configuration in an updated Lagrangian scheme. Last known configuration is denoted by a right-superscript “ i ”, while the next configuration (still unknown) is denoted by a right-superscript “ $i + 1$ ”. Updating (incremental) quantities are represented with an upper-right index “ Δ ”.

A list of the main symbols is provided in the following.

$\mathbf{0}_n$	n-dimension null vector.
$2b$	The distance between the bearings in a wheelset.
$2l$	The distance between the tapelines in a wheelset.
$\bar{\mathbf{a}}_1^1, \bar{\mathbf{a}}_2^1$	Tangential directions at $\bar{\mathbf{x}}^1$.
$\mathcal{B}^1, \mathcal{B}^2$	Body 1 and body 2 in a contact interaction.
$\mathbf{b}^{config.}$	A vector connecting the origin of a rigid body to its centre of mass in the specified configuration.
$\mathbf{B}^{config.}$	Skew symmetric of $\mathbf{b}^{config.}$ in the specified configuration.

\mathbf{c}	Position vector of the centre point of a bi-dimensional arc in a local coordinate system.
$\mathbf{c}^{config.}$	Vector that collects all the convective coordinates in the specified configuration.
c_1	Local x coordinate of the centre point of a bi-dimensional arc.
c_2	Local y coordinate of the centre point of a bi-dimensional arc.
$\mathbf{c}_A, \mathbf{c}_B$	Set of convective coordinates used in the parameterization surfaces Γ_A and Γ_B .
D	Nominal wheel diameter (measured at the tapeline).
$\mathbf{d}^{config.}$	Vector that collects all the generalized coordinates in the specified configuration.
$\mathbf{d}_A, \mathbf{d}_B$	Set of generalized coordinates used in the parameterization surfaces Γ_A and Γ_B .
\mathbf{d}_A^A	Vector in Γ_A , at current configuration, that points from the current solution of the local contact problem to the previous one.
\mathbf{d}_B^A	Vector in Γ_B , at current configuration, that points from the current solution of the local contact problem to the previous one.
$\mathbf{d}_k^{config.}$	A vector connecting the origin of a rigid body to a generic point within the rigid body in the specified configuration.
$\mathbf{D}_k^{config.}$	Skew symmetric of $\mathbf{d}_k^{config.}$ in the specified configuration.
\mathbf{f}	Position vector of the final point of a bi-dimensional arc in a local coordinate system.
f_{11}	Linear longitudinal creep parameter in Carter's model.
f_{22}	Linear lateral creep parameter in Carter's model.
\mathbf{f}_A	Function that describes the arc used to generate an extruded surface.
\mathbf{f}_B	Function that describes the arc used to generate a revolved surface.
F_n, F_N	Normal component of contact force.
F_T	Tangential component of contact force.
F_{Tmax}	Maximum tangential force supported before any sliding occurs.

F_{Ttry}	Friction force that is compared with F_{Tmax} to decide between stick-slip.
g	Gravitational field.
g_n	Normal gap function (scalar).
\mathbf{g}_n	Vector normal gap function in the master-master contact formulation.
g_n	Scalar measure obtained by computing the norm of \mathbf{g}_n .
\mathbf{g}_T	Tangential gap function (vector).
\mathbf{g}_T^Δ	Incremental tangential gap.
$\mathbf{g}_T^{config.}$	Tangential gap function in the master-master contact formulation in the specified configuration.
h_1, h_2	Interpolation factors used to generate an extruded surface.
\mathbf{i}	Position vector of the initial point of a bi-dimensional arc in a local coordinate system.
\mathbf{I}_3	Identity matrix of order 3.
I_x, I_y, I_z	Inertia components computed for a symmetric rigid body.
$\mathbf{J}^{config.}$	Inertia tensor of a 3-dimensional body in the specified configuration.
k_y	Lateral stiffness parameter in Carter's model.
k_ψ	Yaw stiffness parameter in Carter's model.
m	Total mass of a body.
$\bar{\mathbf{n}}^1$	Normal vector of master surface at $\bar{\mathbf{x}}^1$.
$\mathbf{n}_B^{config.}$	Exterior normal of surface Γ_B in the specified configuration.
\mathbf{O}_n	n-dimension null matrix.
P_k	A generic point in a rigid body.
P_P	The origin (pole) of a rigid body.
\mathbf{Q}	Composed rotation tensor, accounting for the transformation between local and global coordinate systems and also the rotation experienced by the attached node in a revolved surface.

\mathbf{Q}_k^Δ	Rotation tensor used to update the previous tangential gap to the next configuration.
$\mathbf{Q}_1, \mathbf{Q}_2$	Rotation tensors that account for the transformation between local and global coordinate systems and also the rotation experienced by the attached nodes of an extrude surface.
$\mathbf{Q}_k^{config.}$	Rotation tensor used to map a generic material point in the specified configuration.
R	Effective radius of a rolling wheel.
\mathbf{r}	Local contact problem equation in the master-master contact formulation.
r	Radius of the bi-dimensional arc used to generate extruded and revolved surfaces.
\mathbf{r}_{1k}	Constraint in displacement degrees of freedom to enforce a rigid body condition.
\mathbf{r}_{2k}	Constraint in rotation degrees of freedom to enforce a rigid body condition.
r_o	Nominal wheel radius (at the tapeline).
t	Time.
T	Total kinetic energy in a 3-dimensional body.
T_1	Translational parcel of the kinetic energy in a 3-dimensional body.
T_2	Rotational parcel of the kinetic energy in a 3-dimensional body.
T_3	Coupling parcel of the kinetic energy in a 3-dimensional body.
$\bar{\mathbf{u}}^1$	Vector of displacement that results in $\bar{\mathbf{x}}^1$ when applied to a projection point in the master surface in the previous configuration.
\mathbf{u}^2	Vector of displacement experienced by point X^2 .
$\mathbf{u}_k^{config.}$	Vector of displacement experienced by a generic point in the specified configuration.
\mathbf{u}_k^Δ	Incremental displacement experienced by a generic point.
\mathbf{u}_P^Δ	Incremental displacement experienced by point P.
u_T	Tangential displacement relative to two surfaces.
V_{cp}	The velocity at the contacting point in a rolling wheel.

\mathbf{x}	Position vector of a node associated to a revolved surface.
$\bar{\mathbf{x}}^1$	Position vector of the orthogonal projection of the slave point onto the master surface in the current configuration.
$\mathbf{X}^1,$	Arbitrary points in bodies \mathcal{B}^1 and \mathcal{B}^2 in the previous configuration.
\mathbf{x}_2	Position vector of a slave point in body \mathcal{B}^2 in the current configuration.
\mathbf{X}^2	Position vector of slave point in body \mathcal{B}^2 in the previous configuration.
\mathbf{x}^k	Position vector of a generic point in the current deformed configuration.
\mathbf{X}^k	Initial position vector of a generic point in the previous configuration.
$\mathbf{x}^1, \mathbf{x}^2$	Position vectors of nodes associated to an extruded surface.
x_{factor}	Distortion factor in local x direction of a revolved surface.
$\mathbf{x}_k^{\text{config.}}$	Position vector of a generic point in a rigid body in the specified configuration.
$\mathbf{x}_P^{\text{config.}}$	Position vector of the origin (pole) of a rigid body in the specified configuration.
y	Lateral degree of freedom in the Carter's model.
z_{factor}	Distortion factor in local z direction of a revolved surface.
α_k^Δ	Incremental rotation experienced by a generic point.
α_P^Δ	Incremental rotation experienced by point P.
\mathbf{A}_P	Skew symmetric of α_P^Δ .
β	The angle between rails and sleepers.
γ	Wheel conicity.
Γ_A, Γ_B	Surfaces candidate to contact in the master-master contact formulation.
$\Gamma_A^{\text{config.}},$ $\Gamma_B^{\text{config.}}$	Surfaces candidate to contact in the master-master contact formulation in the specified configuration.
Γ_C	Contact region in a 3-dimensional body.
ϵ_N	Normal penalty factor.

ϵ_T	Tangential penalty factor.
ζ	Convective coordinate along with the extrusion of a surface.
ζ_A, θ_A	Convective coordinates used in the parameterization of surface Γ_A .
θ	Convective coordinate used in the parameterization of a bi-dimensional arc.
$\lambda_{1k}, \lambda_{2k}$	3-dimensional Lagrange multipliers vectors, unknown, and used to enforce the constraints.
μ	Coefficient of friction.
ξ^1, ξ^2	Convective coordinates used in the parameterization of a generic master surface.
$\bar{\xi}^1, \bar{\xi}^2$	Convective coordinates at \bar{x}^1 .
Ξ_P	Operator relating angular velocity to the rotation degree of freedom parameterized using Rodrigues parameters.
Π_C^P	Contact potential using a penalty method.
ρ	Volumetric mass density function of the material considered for the body.
φ	Evolution operator in the deformation process.
ϕ	Convective coordinate along the revolution of a surface.
$\varphi(\mathcal{B}^1), \varphi(\mathcal{B}^2)$	Evolution operator applied to bodies \mathcal{B}^1 and \mathcal{B}^2 .
φ^1, φ^2	Evolution process for bodies \mathcal{B}^1 and \mathcal{B}^2 .
ϕ_B, θ_B	Convective coordinates used in the parameterization of surface Γ_B .
ψ	Yaw degree of freedom in the Carter's model.
ω	Angular velocity of a rolling wheel.
$\boldsymbol{\omega}$	Vector of angular velocity of a rigid body.
$\boldsymbol{\Omega}$	Skew symmetric of angular velocity.

1. INTRODUCTION

1.1. Motivation

Computer simulation is part of the design process of companies and research centres in the most diverse segments. A myriad of methods has emerged with the advancing of digital computing. Just to name a few of the most popular methods, one can think about the finite element method (FEM) and the multibody dynamic (MBD) technique. Particularly, FEM and MBD are widely used in the simulation of systems of bodies. On one hand, MBD has been successfully employed to describe the dynamic behaviour of mechanical systems of interconnected bodies (usually assumed as rigid bodies). On the other hand, FEM became an indispensable tool in the analysis of deformable parts, permitting evaluation of strains, stresses and becoming useful for structural analysis.

Although such kinds of methods are now well established, they are usually developed on the basis of different techniques and using distinct mathematical frameworks. Nonetheless, the demand for combining rigid and flexible bodies in the same environment was the starting point for the modern research field of flexible multibody dynamics. A flexible multibody system, as defined in [1], may consist of elastic and rigid components connected by joints and connector elements. Real life is plentiful of systems that can be represented in such kind of virtual environment. Automotive, biomedical, machinery, manufacturing and many other fields have practical applications for rigid-flexible multibody simulation. Indeed, an interminable number of examples could be listed here. Just to mention some interesting cases, one can observe the study of animal locomotion in biology, where complex interactions between skeleton and muscles take place to create motion. Another very distinct example can be found in the crash and safety analyses performed in the automotive industry. A full car model is composed of numerous parts and several of these parts are treated as deformable bodies, while some of them are assumed to be rigid during the analysis.

Regarding the background presented above, different research lines can be identified. A rough idea is that if one chooses the MBD formalism, it is necessary to develop techniques capable of considering flexible bodies in that context. On the other hand, if a FEM basis is the choice, it is necessary to develop computationally efficient methods for handling large multibody systems in this scenario. Undoubtedly, both approaches have advantages and disadvantages one over another. Nevertheless, it is far from the scope of the present work making such comparisons. The point that is definitely worth commenting here, as already pointed out by several authors (e.g.: [2] and [3]), is the fact that when the analysis of stresses, strains and wave propagation is not critical for a component, the use of rigid bodies becomes very attractive. Since the movement of the whole body can be described by a maximum of 6 degrees of freedom in a rigid approach, significant computational time can be saved.

This work is not intended to provide a broad review on rigid-flexible multibody modelling. For that purpose we refer to [1], [4], [5] and [6]. However, for a quick overview, it is important to mention that the mostly widely used method for flexible multibody simulation is the floating (or moving) frame approach. This method is classically described in text books such as [7] and [8], and it is available in general purpose multibody programs (e.g.: [9]). In this approach, the large nonlinear overall motion of each body is expressed by a set of rigid body variables, while another set of deformation variables expresses the state of deformation of the body with respect to the moving frame. Nodal variables resulting from linear finite element analyses can be taken as deformation variables (nodal approach), or model reduction can be employed using standard techniques (see, e.g.: [10]) to reduce the size of the problem in a modal approach [11].

An influential work, which represents a departure from traditional approaches, is that presented in [12], where the concept of finite element models is generalized to systems made of structural components connected through kinematic joints, i.e., the work proposes to describe flexible multibody systems from the concept of finite elements. Unifying structural analysis and rigid body dynamics has been considered by other authors. In [13], for example, it was shown that the classical formulations for the two fields can be derived from the same weak form of Lagrange's equation. Furthermore, groups conducting research into FEM presented a series of approaches,

which are based on geometrically-exact theory. Their main purpose is to develop nonlinear finite elements to be used in a multibody dynamic context. In [14], internal constraints in a three-dimensional geometrically-exact beam model are formulated as holonomic constraint relationships. The work includes general joint constraints between beams and rigid components. In their rigid body formulation, both [13] and [14] employ the traditional approach of assuming centre of mass coordinates to decouple the translational and rotational degrees of freedom. Although this assumption is extensively used, it represents a limitation with respect to the possible positions of the node used as pole for the rigid body element. One of the contributions of the present work is to eliminate this restriction. Multibody systems involving geometrically-exact shell elements are presented in [15], where the kinematic nonlinearities associated with large displacements and large rotations in shells are addressed. Moreover, in that work the proposed schemes are designed to meet exact satisfaction of the constraints, unconditional stability and to include high frequency numerical dissipation. Successful applications in multibody systems within the framework of nonlinear finite element methods have been demonstrated for different applications, e.g.: [16] and [17]. In addition, in the same context of nonlinear finite elements, in [18] one can find mechanisms modelled by geometrically-exact beam elements and the mathematical models for joints, springs, dashpots and follower loads.

Contact interactions may occur between distinct bodies or within a single body (self-contact). Contact is a multi-scale phenomenon, rich in complexity. Its mathematical modelling is commonly enforced by mechanical constraints written as inequalities, leading to non-smooth responses. Even in case of linear elasticity models, contact occurrence leads to nonlinearities (see e.g.: [19]). One may find in literature many distinct ways to circumvent the difficulties on mathematical and computational issues, while trying to obtain solution to models involving contact interactions. Each community is usually more inclined to particular methods and techniques to solve their contact models.

Contact involving rigid to rigid and rigid to deformable interactions is a subject of interest of different brands of computational mechanics (see e.g.: [20] and [21] for FEM; [22], [23] and [24] for MBD and [25], [26] and [27] for discrete element methods - DEM) and computer graphics/animation (see e.g.: [28]). In this work, we treat the

case of contact involving rigid bodies using FEM. However, differently from previous works, we employ the master-surface to master-surface contact formulation, which is entirely presented in [29] and [30] and extended here to the context of rigid-flexible interactions. For that, two new surface parameterizations are proposed to establish external surface geometries of extruded/revolved bodies, which represent a large range of applicability.

The whole context introduced above, i.e., a rigid-flexible multibody environment allowing contact interactions, is interesting for railway applications, especially those applications related to the wheel-rail interface and its influence over the dynamic behaviour of railway vehicles. In [31], a comprehensive discussion on the influence of the structural flexibility of various components, including the wheelset, the bogie frames and the tracks, over the dynamics of railway vehicles is presented. Several formulations and computer techniques for modelling structural flexibility are discussed. The investigation is motivated by the fact that the structural flexibility can have a significant effect on the overall dynamics of railway vehicles, ride comfort, lateral stability, track response to vehicle forces, stress analysis, wheel-rail contact forces, wear and crashworthiness. Other works presenting studies of the same nature can be found in [32], [33], [34] and [35]. In addition, in [31] the authors highlight the fact that rigid body models of railway vehicles are adequate to analyse low frequency dynamic phenomena such as lateral stability. In these models, the only source of flexibility is the suspension systems of the vehicle. Other dynamic effects, in the mid and high-frequency ranges and possibly in the low-frequency range, may require modelling the structural flexibility.

1.2. Research objective

The main purpose of present research is to expand the range of applicability of the master-surface to master-surface contact formulation, allowing its application in several distinct contexts, including railway engineering. This objective is achieved through the development of new surface parameterizations suitable for multibody systems and capable of representing complex geometries based on arcs. The work also comprises the full development of a rigid body formulation, in the context of

nonlinear finite elements, completely compatible with the master-surface to master-surface contact formulation.

Several different examples can be represented by the proposed models. A three-dimensional isolated railway wheelset, with realistic wheel profiles, is one of these examples. For this, the wheelset is idealized as a rigid body composed by two wheels rigidly attached to an axle and the rails are represented by rigid or flexible geometrically-exact beam finite elements. The new surface parameterizations are used to draw both rail and wheel profiles, making it possible to establish the wheel-rail contact in a frictional master-surface to master-surface approach.

Due to its innovative treatment of normal and tangential gap functions, the master-surface to master-surface contact formulation is proved to be efficient in representing rolling contact, as well as the transition between rolling and sliding. The possibility of combining this formulation with structural finite elements, such as beam elements, brings an opportunity to save computational time by reducing the number of degrees of freedom of the model, but still being able to consider global flexibility effects when necessary.

In summary, in this work the master-surface to master-surface contact formulation is expanded into cases involving complex contact surfaces based on arcs. This kind of surface is appropriate for representing wheel and rail profiles and it can be seen as an opening for further studies, highlighting the possibility of studying the dynamics of full railway vehicles, which is an essential step in the design process of vehicle components, the investigation of vehicle stability and can also provide valuable inputs for wheel and rail profile optimization.

1.3. The GIRAFFE project

The numerical models developed in this work were implemented in GIRAFFE, which is the acronym for Generic Interface Readily Accessible for Finite Elements [36]. It is coded in C++ language and it has been created by Professor Alfredo Gay Neto at the University of São Paulo. GIRAFFE is a platform for multibody simulation based on nonlinear finite elements. The program has features such as beam and shell finite

elements formulated on a geometrically-exact basis, several kinds of connector elements (e.g.: spring, dashpot and revolute joints) as well as contact formulations based on the master-master concept. For more information about GIRAFFE capabilities see [37].

The power of object-oriented programming (OOP) is explored in GIRAFFE, which makes the inclusion of new formulations very friendly. Moreover, the platform can be easily used together with a hybrid symbolic-numerical (HSN) approach. The basic idea of HSN is to combine symbolic and algebraic computational (SAC) systems, such as Mathematica®, with automatic code generators, such as AceGen®. In this approach, the role of the SAC system is to perform (automatically) differentiations necessary to the development of nonlinear finite elements. When these systems are combined with automatic code generators, the obtained codes can be incorporated into the chosen finite element environment, for example, in GIRAFFE. For further details about the automation of finite element methods, we refer to [38].

1.4. Outline

Basic concepts of railway systems are introduced in Chapter 2. We do not intend to provide an in-depth study on this subject, but only to familiarize the reader with the essential characteristics of the wheel-rail interface, which will appear throughout this work. Then, in Chapter 3, the subject of computational contact mechanics is addressed. Classical concepts are extracted from literature, providing the necessary background for what follows and the master-surface to master-surface contact formulation is reviewed in details.

Nevertheless, the main contribution of the work is presented from Chapter 4 onwards. A rigid body formulation is developed for implementation in the context of a finite element environment. Inertial contributions due to distribution of mass of a rigid body are fully developed, considering a general pole position associated with a single node, representing a rigid body element. Additionally, a mechanical constraint is presented to connect a rigid region composed by several nodes, which is useful for linking rigid/flexible bodies in a finite element environment. Rodrigues rotation parameters are used to describe finite rotations, by an updated Lagrangian description.

In Chapter 5, new surface parameterizations are presented to establish contact pairs in a master-surface to master-surface contact approach, permitting pointwise interaction in a frictional scenario, combining the rigid body element and flexible bodies and aiming to consider their interaction in a rigid-flexible multibody environment. Numerical examples are provided to show robustness and applicability of the methods in both chapters.

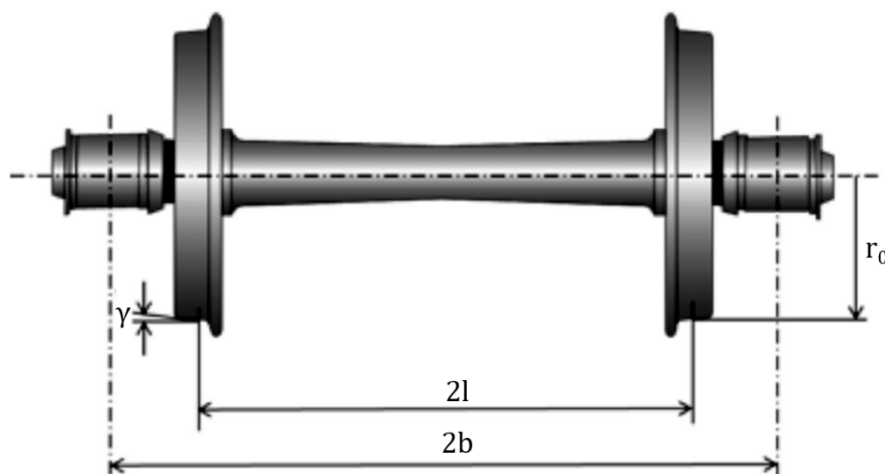
In Chapter 6, the lateral oscillations observed in railway vehicles are introduced and the computational models developed during this work are employed in a try to better understand this behaviour, the so-called hunting phenomenon. Finally, in Chapter 7, some conclusions on what have been presented, as well as an outlook for future developments are drawn.

2. BASIC CONCEPTS OF RAILWAY SYSTEMS

2.1. Global overview

It is well known that railway vehicles differ from others due to the fact they operate on rails. The fundamental mechanism to guide these vehicles is the wheelset configuration, which consists of two conical wheels rigidly attached to an axle (Figure 2.1).

Figure 2.1: Typical wheelset configuration.



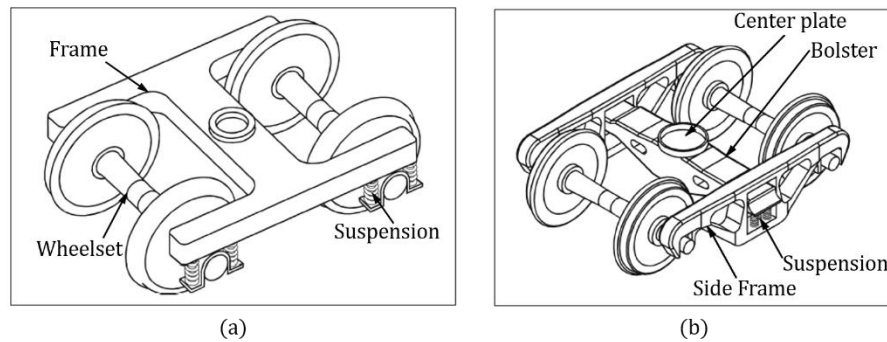
Source: [39]

The wheelset geometry, resulting from the assemblage of the two opposed conical wheels, provides characteristics that are unique to this system. The wheelset has a self-centring capability. Moreover, it can negotiate curves, i.e., the rolling radii can be adjusted in curves by the introduction of small lateral displacements. These lateral displacements allow each wheel to travel a different distance for the same rotation.

If the running gear of a railway vehicle is mounted on a separate structure, allowing relative movement with respect to the vehicle body/wagon, then, this vehicle is named as a “bogied” vehicle. The most common number of wheelsets connected by

a bogie is two. Moreover, freight trains usually have two bogies of two axles per wagon. Each bogie has its own suspension system that can be of one or two stages. In addition, the elastic elements of the suspension system can be placed between the wheelset and the structure of the bogie (frame), as shown in Figure 2.2(a), or, between a side frame and another structure called bolster, as shown in Figure 2.2(b). For a more comprehensive description of the running gear system, we refer to [40].

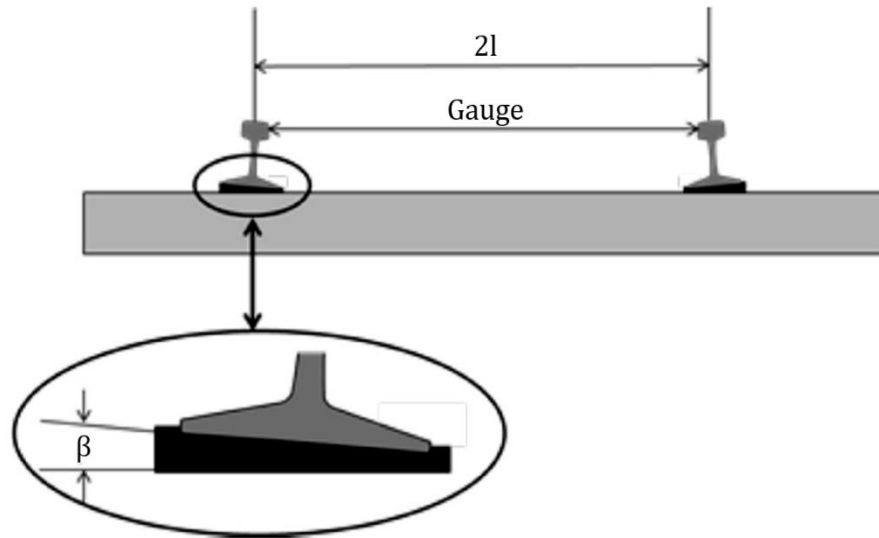
Figure 2.2: Typical bogie configurations: (a) Primary suspension. (b) Secondary suspension.



Source: [39]

The wheels interact with the track and the track is a very complex system, explored in depth in [41]. It consists of several elements and its design involves the science of soil mechanics. In a simplified view, the main components of a typical track are the rails, which are mounted over sleepers at a particular distance known as gauge. A reduced illustration of a typical track is shown in Figure 2.3, where one can see the rails and the sleepers. Between these two components, there are the rail pads.

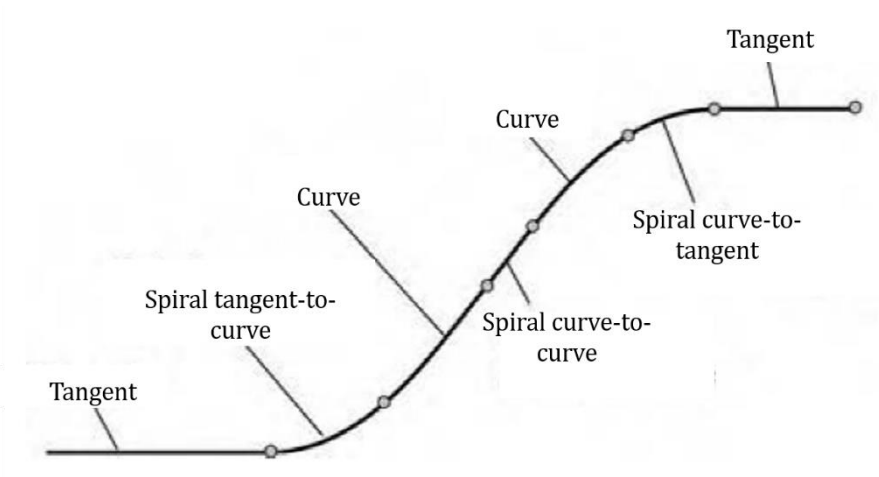
Figure 2.3: Typical section of a track.



Source: [39]

Tracks are usually composed of segments such as those illustrated in Figure 2.4.

Figure 2.4: Track segments.



Source: [42]

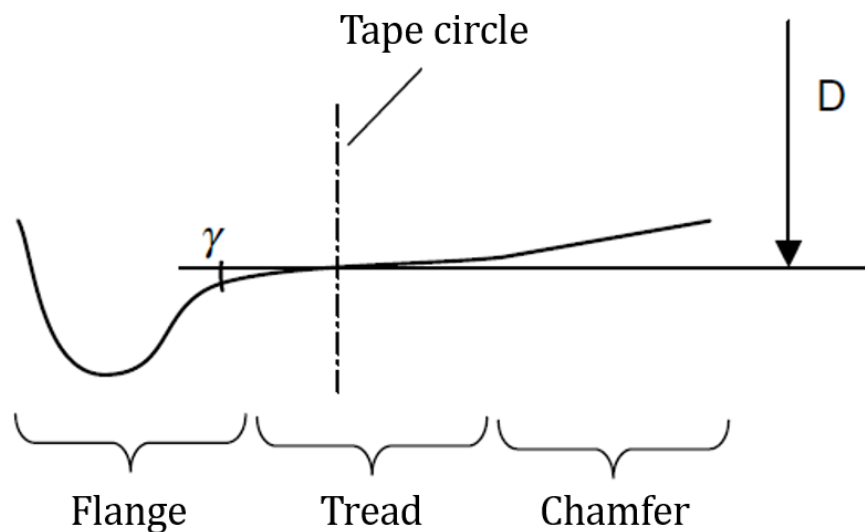
In [39], Tournay shows that the angle β between rails and sleepers (Figure 2.3) in conjunction with the angle γ , i.e., the wheel conicity shown in Figure 2.1, permits that

the contact interaction is centralized on the top of the rails when operating on tangent tracks.

2.2. Wheel and rail geometry

As pointed out by Wickens [43], the most important characteristic incorporated into the design of wheels along its evolution in railway history is the conical profile with an internal flange. Three main regions can be identified in current designs of wheels: the flange, the tread and the chamfer, as illustrated in Figure 2.5. In addition, in this figure the position of the tape circle (or taping line) is indicated. In practice, this line usually represents the lateral position where the wheel circumference is measured and the wheel diameter is inferred from this circumference.

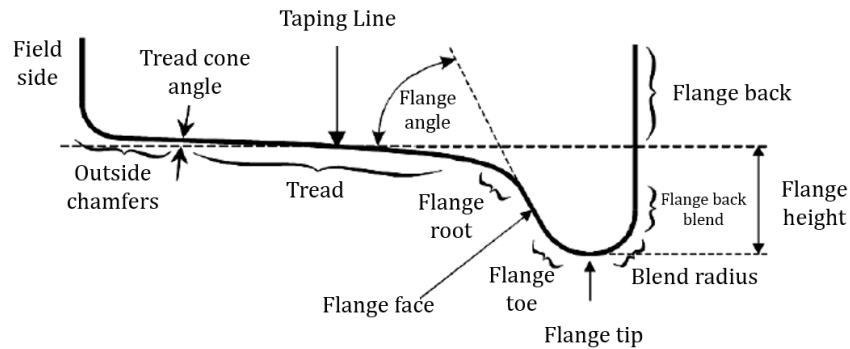
Figure 2.5: The main regions of wheel profiles.



Source: [40]

In a more detailed illustration, features of a typical wheel are named in Figure 2.6.

Figure 2.6: Detailed wheel profile.

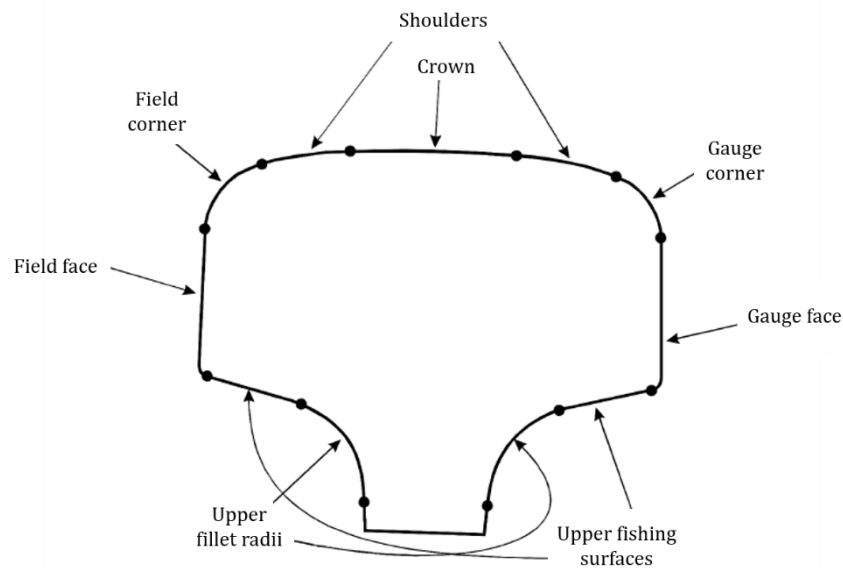


Source: [39]

On the side of rails, according to Dahlberg [41], the most common design is due to Charles Vignoles, and the term “Vignole profile” is usual. This kind of profile is similar to an I-profile where the upper flange is converted to form the top of the rail. Rails have the fundamental function of providing a smooth surface for the rolling wheels. Moreover, they have to guide the wheelset along the track. Rails are also the first to receive the loads coming from the vehicle; therefore, they are also responsible for distributing these loads onto the sleepers.

Features of a typical rail profile are named in Figure 2.7.

Figure 2.7: Detailed rail profile.



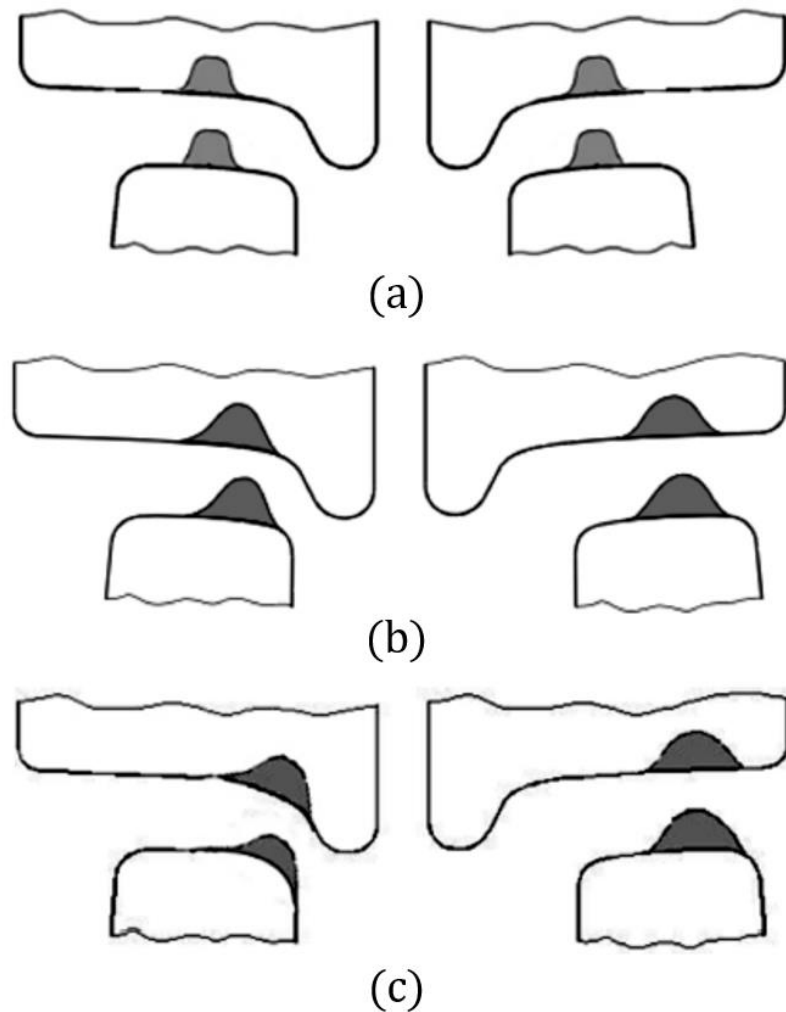
Source: [39]

2.3. Wheel-rail contact

Wheel-rail contact represents an open tribo-system susceptible to the external environment conditions. This interface has critical importance over the dynamic behaviour of the vehicle and the safety of the operation. Although tangential and normal contact directions are coupled in practice, some fundamental properties of wheel-rail interface can be studied decoupling these phenomena [44].

The contact point in a wheel-rail interface varies continuously, not only along the track, but also laterally. As long as the train is moving, the contact point is changing. Moreover, each wheel experiences different contact conditions, resulting in different wear rates [45]. Although more complex situations can be observed in practice (due to wearing, defects, etc.), the most common contact conditions are those illustrated in Figure 2.8.

Figure 2.8: Typical contact positions.



Source: [39]

According to Tournay [39], Figure 2.8(a) represents the condition expected for tangent tracks, where the wheel tread should make contact with the top of the rail (crown). The condition illustrated in Figure 2.8(b) is commonly observed in curves with large radii of curvature, while Figure 2.8(c) represents the case of curves with small ones.

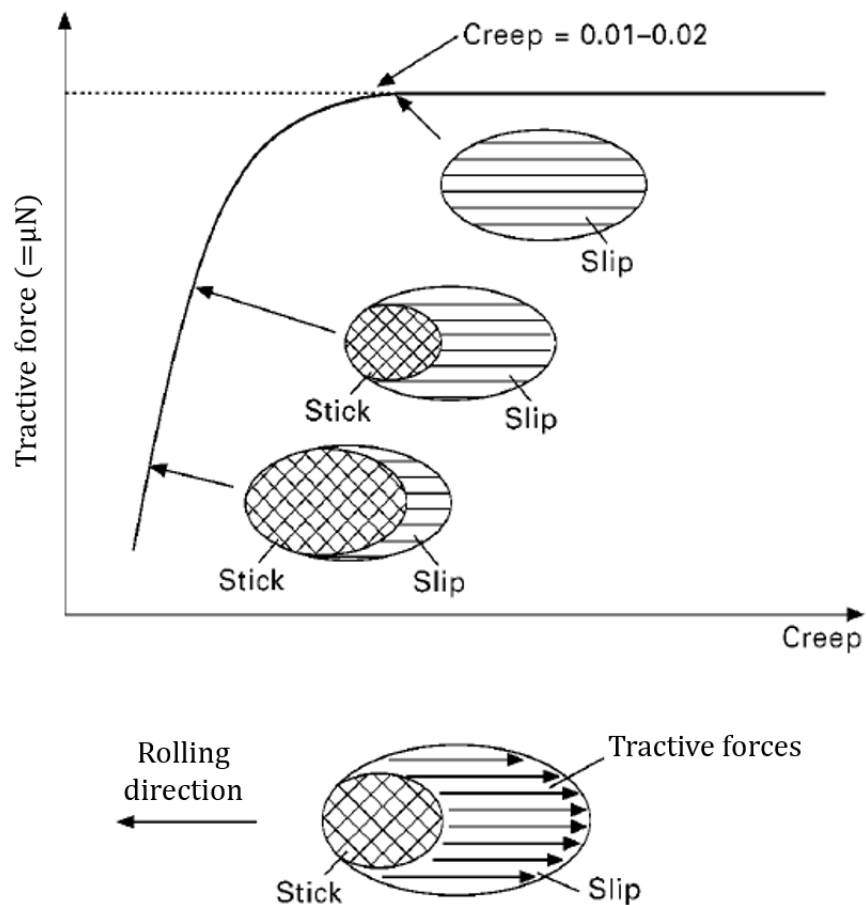
As mentioned in [45], the simplest model employed in the study of normal contact stresses is the Hertz model. The hypotheses assumed by this model are: (i) surfaces are continuous and non-conforming, (ii) strains are small, (iii) each solid is considered as an elastic half-space and (iv) frictionless interaction is assumed. Hypothesis (iii) is commonly followed in contact theories and by this assumption the

highly concentrated stresses of the contact region can be treated separately from the general stress distribution of the bodies. Therefore, hypothesis (iii) implies that contact area should be small when compared with the dimensions of each body and with the radii of curvature of each surface. Even though wheel-rail contact violates Hertz's hypotheses in several ways, this approach is a very good starting point nevertheless.

When tangential direction is considered, tractions in other two directions are also needed. If two bodies are put in contact by a normal load and then subjected to an increasing tangential load, the bodies can, eventually, start sliding one over the other. Before a general sliding occurs and the whole body starts moving, local sliding (micro-slip) can occur while most of the contact area remains static (in stick condition). Stick-slip transitions, as well as the regions where they occur, are of fundamental interest for practical applications. In tangential contact, differences arise between sliding and rolling. During sliding, the same material particles remain in contact for the overall motion. On the other hand, during rolling, "fresh material" enters in contact all the time.

The difference between sliding and rolling makes it possible to introduce the term "creep", which stands for an apparent sliding velocity between the two surfaces. Creepage, i.e., the relative sliding between two surfaces, is resisted by tangential forces, the creep forces. In addition to the creep forces due to lateral and longitudinal creepages, spin moments can also develop due to spin creepage (relative movement around the common normal direction). In Figure 2.9, the classic curve relating traction and creep is presented. Such kind of curve can be drawn from Kalker's theory, for example. Moreover, one can observe that in steady rolling at low creepage, creep and tractive forces are proportional and Kalker's linear theory applies [46].

Figure 2.9: Relationship between traction and creep.



Source: [45]

The concepts of creepage and creep forces can be seen as a way to establish a relationship between the mechanics of rigid bodies and the mechanics of deformable bodies when both involve contact interactions. For example, for a rigid wheel rolling on a planar surface $V_{cp} = 0$, with V_{cp} being the velocity at the contacting point. The velocity at the centre of the wheel is $V = \omega R$. When deformable bodies are considered in the same scenario a contact area appears due to the deformation of the bodies, and the infinite points within this contact area present velocities different than 0, so that an apparent sliding velocity (the so called creep) is observed.

During his career, Professor J.J. Kalker made notable contributions to the field of contact mechanics. These contributions and its corresponding algorithms are widely used for detailed investigation of wheel-rail contact through computational simulation.

Polach et al. [47] present a great variety of numerical analyses performed in railway engineering. The versatility of today's computer programs allows engineers to test different wheel-rail combinations, making it possible to understand and to optimize the design process, all of this in a virtual environment. Outputs from detailed models of the wheel-rail interface are fundamental to maintenance planning and failure prediction. Moreover, being able to estimate correctly the forces developed at this interface is a key factor in safely designing structural components of railway vehicles and tracks.

An overview of the leading computer programs in this field can be seen in the famous "Manchester Benchmarks" [48]. Nonetheless, it is worth mentioning here the importance of the program CONTACT® [49], which implements the original Kalker's theory [46] [50], with several improvements made by the current owner of the software. Other two important tools are the FASTSIM® algorithm, based on the simplified theory of Kalker, also described in details in [46], and USETAB®, a table-based program consisting of tables pre-calculated by CONTACT®, which are ready to be read and interpolated in a simple routine. Both FASTSIM® and USETAB® are fast methods for solving contact problems (faster than the full Kalker's theory) that are available in the most popular commercial software, such as those compared in the Manchester Benchmarks.

3. COMPUTATIONAL CONTACT MECHANICS

3.1. Introduction and historical background

Contact is a multi-scale phenomenon which is rich in complexity. In a macro-scale it can be interpreted as the mechanism of load transferring between two bodies when they touch each other. However, in smaller scales (e.g.: micro or nanoscale), the topography of the surfaces involved in a contact interaction plays an important role, with remarkable impacts over the understanding of phenomena such as adhesion, friction and wear. Moreover, due to its “non-smooth” response, contact modelling imposes serious conceptual, mathematical and computational difficulties to the solution of mechanical problems.

Three main areas can be identified in the study of contact mechanics: (i) The science embracing the study of friction, wear and lubrication, the so-called tribology [51] [52]. (ii) The science comprising analytical models intended to predict contact stresses and strains, which has formally started in 1882 with the famous paper “On the contact of elastic solids”, by Hertz [53] [54]. (iii) The science focused on the development of computational contact methods to be employed together with other numerical procedures, such as the finite element method. Examples of texts covering computational contact mechanics in depth are those by Wriggers [19], Laursen [55], Yastrebov [56] and Konyukhov and Schweizerhof [57]. Although the present work handles the subject of computational contact mechanics employed together with nonlinear finite elements, the finite element method itself is not reviewed here. For this purpose, we refer to [58] and [59].

Among the pioneering publications employing the finite element method in the solution of contact problems, Wilson and Parson [60] presented a technique of differential displacements whereby problems involving elastic contact were solved by the finite element method when statically indeterminate conditions occur due to interference fits or similar interfacial conditions. Chan and Tuba [61] described a modified finite element method for solving problems of elastic bodies in contact, the

authors enforced the condition of non-penetration of elected points in each body and solved the problem in an iterative process. Francavilla and Zienkiewicz [62] presented a simple procedure of obtaining flexibility matrices in terms of contact pressures at possible contact points of two bodies, allowing the frictionless contact pressures to be solved as a quasi-linear problem. Stadter and Weiss [63] introduced the concept of establishing contact through gap elements, a kind of intermediate layer, placed between the contacting bodies, intended to account for contact occurrence. In terms of computer programs, DYNA2D/3D and NIKE2D/3D are said to be the first programs capable of simulating contact in large deformation scenarios in large scale and efficiently [19].

In computational contact mechanics, three main fields can be distinguished:

- Contact in finite element methods (FEM): usually handling small or large displacements, elastic or inelastic behaviour.
- Contact in discrete methods (DEM): usually handling a huge number of particles.
- Contact in multibody dynamics (MBD): usually handling the dynamics of rigid bodies.

Despite this distinction, common techniques are shared between the methods. Furthermore, three basic steps should be present in any contact formulation: contact detection, contact discretization and contact solution.

Contact detection is a step that precedes all the others. Indeed, it is during this step that contact occurrence is determined. The objective of this phase is to find the closest points between surfaces candidate to contact and to monitor these points in order to detect the contact event. Once contacting points are found, a contact constraint has to be imposed avoiding interpenetration of the bodies. Contact discretization is related to the structure of the elements used to compute contact interactions. In practice, the conventional types of discretization used in finite element methods are node-to-node, node-to-surface and surface-to-surface discretization.

Finally, the solution step involves adding the contact contributions to the global solution of the problem. In the solution of boundary value problems, weak form of equilibrium equations is needed and the weak form contributions due to contact presence results in variational inequalities, creating a nonlinear problem, even when dealing with linear elasticity. However, essential equations that describe the behaviour of the bodies do not change due to contact inclusion.

Node-to-node is the simplest method used for establishing contact. In this method, contact is defined between pre-selected nodes. In a very simplified description, one can understand node-to-node contact as if a fictitious spring were placed between the two nodes. If the nodes tend to move away (contact opening), this spring offers no stiffness, but if the distance between the nodes becomes smaller and smaller, tending to zero, a very large stiffness is activated for the spring, constraining the movement. This method is not appropriate if large sliding is expected.

Node-to-surface discretization is classic and represents the most widely used contact discretization scheme for finite element analyses. It consists of selecting a bunch of nodes, the “slave nodes”, which will interact with their normal projection in a parameterized (master) surface. Slave nodes are not allowed to penetrate master segments. In this approach, the concept of master-slave is very clear since one has slave points interacting with master segments. The method is quite general and allows finite relative sliding between the surfaces. However, if compared with the node-to-node method, the computational cost is increased.

Surface-to-surface is similar to the node-to-surface discretization. However, instead of selecting slave nodes, in this approach both the master and the slave sides are made of surface segments. The contact interaction happens in a weak sense, and the contact constraint is imposed over regions centred at the nodes lying on the slave surface. Although surface-to-surface discretization presents smoother behaviour, the computational cost is higher than that of the traditional node-to-surface approach.

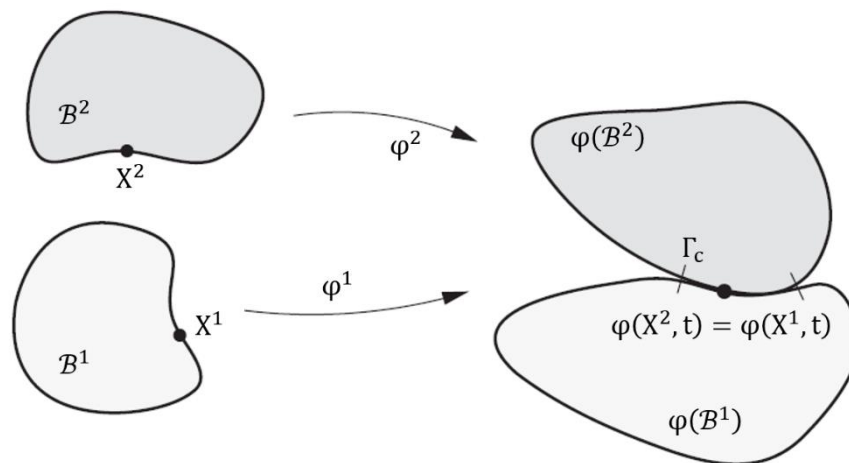
It is important to notice that there exist different approaches for contact, especially in case of establishing contact between beam elements or other special elements such as rigid bodies. In section 3.5, one of these formulations is detailed, it

is called master-surface to master-surface contact formulation and although it uses concepts of surface-to-surface discretization, it is not based on the traditional master-slave approach.

3.2. Contact kinematics

Contact kinematics involves the derivation of normal and tangential functions, the so-called gap functions. Figure 3.1 illustrates the general case of finite deformation, where three-dimensional bodies touch each other over a region Γ_c . In this picture, φ represents the deformation process, i.e., φ is the evolution operator. Normal and tangential kinematic relations have to be developed for Γ_c , as follows.

Figure 3.1: Contact in finite deformation context.

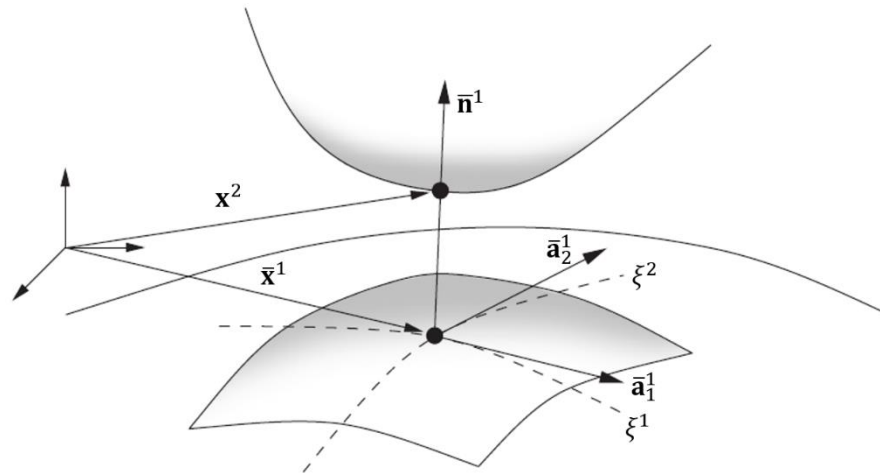


Source: [19]

3.2.1. Normal contact in three-dimensional bodies

In Figure 3.2, node-to-surface contact is illustrated. The current position of an arbitrary slave point is given by \mathbf{x}^2 (result of the deformation process $\varphi(X^2, t)$). In the finite element context, this point represents one of the pre-selected slave nodes. The master surface is parameterized using convective coordinates ξ^1 and ξ^2 and the position of the orthogonal projection of the slave point onto the master surface is indicated by $\bar{\mathbf{x}}^1$.

Figure 3.2: Bodies getting in touch.



Source: [19]

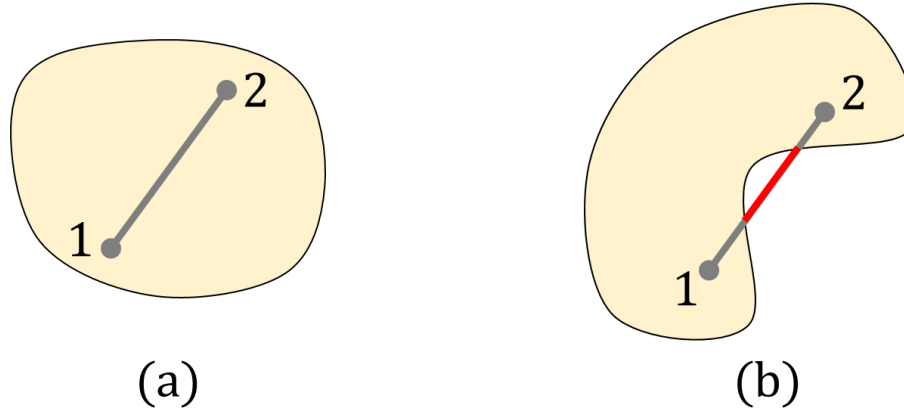
It is important to understand that $\bar{\mathbf{x}}^1$ receives an overbar in the present nomenclature to indicate that $\|\mathbf{x}^2 - \bar{\mathbf{x}}^1\|$ represents the minimum distance between \mathbf{x}^2 and the master surface. Point $\bar{\mathbf{x}}^1$ has convective coordinates $(\bar{\xi}^1, \bar{\xi}^2)$ and the normal direction at this point is $\bar{\mathbf{n}}^1$. If convex surfaces are assumed (at least locally), the solution of the minimum distance problem is unique, leading to a single point on master surface.

The non-penetration condition is given by:

$$(\mathbf{x}^2 - \bar{\mathbf{x}}^1) \cdot \bar{\mathbf{n}}^1 \geq 0. \quad (3.1)$$

In a Euclidian space, a convex region is a region where a straight line segment can be defined between two arbitrary points within the region and every point on this line segment is also within the region, see Figure 3.3.

Figure 3.3: Convex definition: (a) Convex region. (b) Non-convex region.



Source: Author

Since the angle between $(\mathbf{x}^2 - \bar{\mathbf{x}}^1)$ and $\bar{\mathbf{n}}^1$ is 0° for open contacts or 180° if \mathbf{x}^2 penetrates the master surface, by using the definition of the dot product¹, it is possible to define the normal gap function as:

$$g_n = \begin{cases} (\mathbf{x}^2 - \bar{\mathbf{x}}^1) \cdot \bar{\mathbf{n}}^1 & \text{if } (\mathbf{x}^2 - \bar{\mathbf{x}}^1) \cdot \bar{\mathbf{n}}^1 < 0 \\ 0 & \text{otherwise} \end{cases} \quad (3.2)$$

Notice that the gap function, as presented in equation (3.2), accounts for the case when the surfaces are not touching each other, i.e, opened gap with $g_n = 0$. But, the same function is used to evaluate the case when there are interpenetration between surfaces, i.e. a negative gap value. Defining the gap function in this way follows reference [19] and other authors may call it with different names or even considering opposite signs (see e.g. [55]).

In order to obtain the weak form of (3.2), we compute the variation of g_n , expressed as:

¹ $\mathbf{a} \cdot \mathbf{b} = \|\mathbf{a}\| \|\mathbf{b}\| \cos\theta$, where θ is the angle between vectors \mathbf{a} and \mathbf{b} .

$$\delta g_n = \delta((\mathbf{x}^2 - \bar{\mathbf{x}}^1) \cdot \bar{\mathbf{n}}^1). \quad (3.3)$$

Note that the position of any arbitrary point in the deformed (current) configuration is given by:

$$\mathbf{x}^k = \mathbf{X}^k + \mathbf{u}^k, \quad (3.4)$$

where \mathbf{X}^k is the initial position and \mathbf{u}^k represents the displacement experienced by the point. A convenient technique to compute the variations in expression (3.3) is to perform time-derivatives of those quantities, taking into account the chain rule. For example, \mathbf{x}^2 is a function of \mathbf{u}^2 , so that:

$$\frac{d\mathbf{x}^2}{dt} = \frac{\partial \mathbf{x}^2}{\partial \mathbf{u}^2} \frac{d\mathbf{u}^2}{dt}. \quad (3.5)$$

Since \mathbf{X}^2 is constant with respect to \mathbf{u}^2 , equation (3.5) simplifies to:

$$\frac{d\mathbf{x}^2}{dt} = \frac{d\mathbf{u}^2}{dt} \therefore d\mathbf{x}^2 = d\mathbf{u}^2. \quad (3.6)$$

Then, it is possible to write:

$$\delta \mathbf{x}^2 = \delta \mathbf{u}^2. \quad (3.7)$$

Employing the same technique for $\bar{\mathbf{x}}^1$, which is a function of $\bar{\mathbf{u}}^1$, ξ^1 and ξ^2 :

$$\frac{d\bar{\mathbf{x}}^1}{dt} = \frac{\partial \bar{\mathbf{x}}^1}{\partial \bar{\mathbf{u}}^1} \frac{d\bar{\mathbf{u}}^1}{dt} + \frac{\partial \bar{\mathbf{x}}^1}{\partial \xi^\alpha} \frac{d\xi^\alpha}{dt} \therefore d\bar{\mathbf{x}}^1 = d\bar{\mathbf{u}}^1 + \bar{\mathbf{x}}^1_{,\xi^\alpha} d\xi^\alpha. \quad (3.8)$$

In expression (3.8), summation is implied for repeated indexes and $\alpha = 1, 2$. Moreover, $\bar{\mathbf{x}}^1_{,\xi^\alpha}$ was used to improve readability of $\frac{\partial \bar{\mathbf{x}}^1}{\partial \xi^\alpha}$. Then, it is possible to write:

$$\delta \bar{\mathbf{x}}^1 = \delta \bar{\mathbf{u}}^1 + \bar{\mathbf{x}}_{,\xi\alpha}^1 \delta \xi^\alpha. \quad (3.9)$$

Using (3.7), (3.9) and the product rule in (3.3) we obtain:

$$\delta g_n = (\delta \mathbf{u}^2 - \delta \bar{\mathbf{u}}^1 - \bar{\mathbf{x}}_{,\xi\alpha}^1 \delta \xi^\alpha) \cdot \bar{\mathbf{n}}^1 + (\mathbf{x}^2 - \bar{\mathbf{x}}^1) \cdot \delta \bar{\mathbf{n}}^1. \quad (3.10)$$

From Figure 3.2, one can notice that:

$$\bar{\mathbf{n}}^1 = \frac{(\mathbf{x}^2 - \bar{\mathbf{x}}^1)}{\|\mathbf{x}^2 - \bar{\mathbf{x}}^1\|}. \quad (3.11)$$

Moreover, using the same figure, $\bar{\mathbf{n}}^1$ can also be defined in terms of tangent vectors $\bar{\mathbf{a}}_\alpha^1 = \bar{\mathbf{x}}_{,\xi\alpha}^1$:

$$\bar{\mathbf{n}}^1 = \frac{(\bar{\mathbf{a}}_1^1 \times \bar{\mathbf{a}}_2^1)}{\|\bar{\mathbf{a}}_1^1 \times \bar{\mathbf{a}}_2^1\|}. \quad (3.12)$$

Vector $\bar{\mathbf{n}}^1$ represents the exterior master-surface normal (always pointing outwards). It is clear that $\bar{\mathbf{n}}^1 \cdot \bar{\mathbf{n}}^1 = 1$ and $\bar{\mathbf{a}}_\alpha^1 \cdot \bar{\mathbf{n}}^1 = 0$. When using convective coordinates, the following condition can be applied (see Appendix B of Ref. [19]):

$$\mathbf{n} \cdot \dot{\mathbf{n}} = 0, \quad (3.13)$$

noticing that a dot over a variable indicates its time-derivative.

Multiplying the second parcel of (3.10) by $\frac{\|\mathbf{x}^2 - \bar{\mathbf{x}}^1\|}{\|\mathbf{x}^2 - \bar{\mathbf{x}}^1\|} = 1$ does not alter the expression. However, if one interpret $\bar{\mathbf{n}}^1$ as being equivalent to $\delta \bar{\mathbf{n}}^1$, by doing this, (3.13) and $\bar{\mathbf{a}}_\alpha^1 \cdot \bar{\mathbf{n}}^1 = 0$ can be used so that (3.10) simplifies to:

$$\delta g_n = (\delta \mathbf{u}^2 - \delta \bar{\mathbf{u}}^1) \cdot \bar{\mathbf{n}}^1. \quad (3.14)$$

As pointed out in [19], for linearization purposes necessary for the Newton-Raphson method, expression (3.10) should be used instead of (3.14). By author's knowledge, the expressions derived in this section were first presented in [64].

3.2.2. Tangential contact in three-dimensional bodies

Two general cases hold for tangential direction: (i) stick condition, where no relative sliding occurs between contacting surfaces and (ii) sliding, where the contact points move in tangential direction.

In stick condition, once the contact is established, the solution $(\bar{\xi}^1, \bar{\xi}^2)$ does not change during the movement. This condition allows us to write a special tangential gap function to represent sticking:

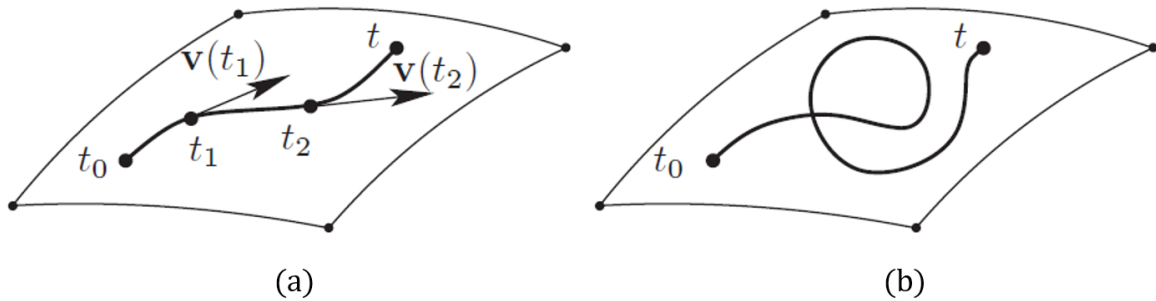
$$\mathbf{g}_T = ((\mathbf{x}^2 - \bar{\mathbf{x}}^1) \cdot \bar{\mathbf{a}}_\alpha^1) \bar{\mathbf{a}}^\alpha = \mathbf{0}. \quad (3.15)$$

It is important to observe that, for closed normal gaps, in stick condition, there is no need to make distinction between normal and tangential directions. Therefore, it is possible to combine $g_n = 0$ with $\mathbf{g}_T = \mathbf{0}$ to write:

$$(\mathbf{x}^2 - \bar{\mathbf{x}}^1) = \mathbf{0}. \quad (3.16)$$

On the other hand, sliding condition implies in relative movement between \mathbf{x}^2 and its normal projection $\bar{\mathbf{x}}^1$, which means that the solution $(\bar{\xi}^1, \bar{\xi}^2)$ will change according to the movement of \mathbf{x}^2 over the master surface.

Figure 3.4: Contact path over the master-surface.



Source: [19]

In Figure 3.4(a), the trajectory of \mathbf{x}^2 is illustrated for the time interval $t_0 - t$. Moreover, in the same picture, the relative velocities are shown at times t_1 and t_2 . The trajectory is unknown and arbitrary, as shown in Figure 3.4(b). In order to be able to draw this trajectory, it is necessary to integrate the relative velocities.

3.3. Constitutive equations for contact

With respect to the normal contact direction, one can develop constitutive laws to account for the micromechanics of the contact area or choose a purely geometric approach. On the tangential direction, on the other hand, a constitutive law accounting for friction is always necessary for the sliding condition.

The classic approach for normal contact is that in which there is no need of special constitutive equations. In this case, contact pressure is obtained as a reaction on the contact area, being deduced directly from the constraint equations. The non-penetration condition was introduced in expression (3.1) and can be rewritten as $g_n \geq 0$, recalling that $g_n = 0$ only when contact occurs. If adhesion is disregarded, when $g_n = 0$, the normal component of contact forces, F_n , has to be negative. So that, for contact condition (closed gap) $g_n = 0$ and $F_n \leq 0$ and for open gap $g_n \geq 0$ and $F_n = 0$. These are the so-called Hertz-Signorini-Moreau conditions, which can be written in the Karush-Kuhn-Tucker (KKT) form:

$$g_n \geq 0,$$

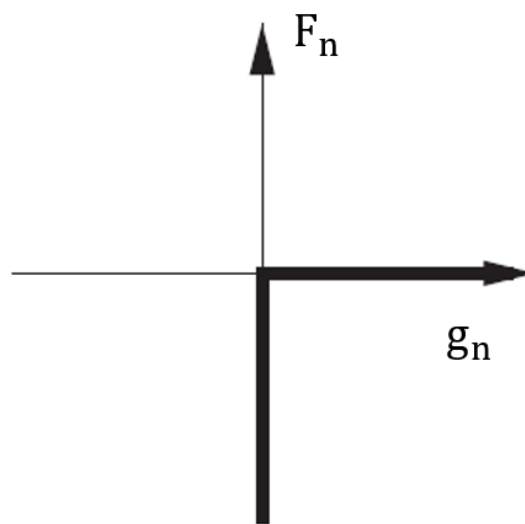
$$F_n \leq 0,$$

(3.17)

$$g_n F_n = 0.$$

Conditions from expression (3.17) are illustrated in Figure 3.5.

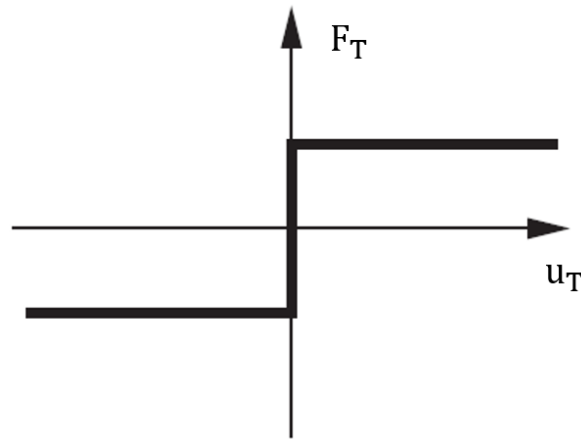
Figure 3.5: Contact normal force x normal gap.



Source: [19]

Constitutive equations for tangential direction can be very complex since it differs between stick and slip conditions. In the classic Coulomb's friction law, which is the most frequently used tangential constitutive equation, no relative movement occurs between two surfaces subjected to a tangential force until this force reaches a certain limit, which is illustrated in Figure 3.6.

Figure 3.6: Coulomb's friction law.



Source: [19]

The relative tangential movement is called sliding. The Coulomb's friction law states that the absolute value of the maximum tangential force F_{Tmax} supported before any sliding occurs is given by:

$$F_{Tmax} = \mu |F_n|, \quad (3.18)$$

where μ is the sliding friction coefficient, constant in the Coulomb's law.

In order to decide between stick and slip, a trying force F_{Ttry} has to be computed and compared with F_{Tmax} . Notice that the friction force is always opposite to the relative sliding tendency.

To compute F_{Ttry} distinct techniques can be used in conjunction with the definition of the tangential gap function. Later in this work, the implications of using a penalty based method will be addressed.

3.4. Contact constraint enforcement

Different techniques are available to incorporate contact constraints in the weak form of boundary value problems. These techniques are developed aiming at overcoming the difficulties associated with the non-smoothness of contact interactions. Most of the finite element codes employ Lagrange multipliers or Penalty methods to enforce contact constraints [19]. Here we introduce the Penalty method, which will be employed in this work.

Penalty methods are widely used for enforcing contact conditions. In this method, a penalty term due to contact constraint is added to the energy of the system:

$$\Pi_c^P = \frac{1}{2} \int_{\Gamma_c} (\epsilon_N (g_n)^2 + \epsilon_T \mathbf{g}_T \cdot \mathbf{g}_T) dA \quad \text{for } \epsilon_N, \epsilon_T > 0, \quad (3.19)$$

where ϵ_N and ϵ_T are normal and tangential penalty factors, respectively.

Penalty parameters can be interpreted as fictitious springs placed between contacting surfaces. Their values affect the contact solution in different ways. Low values of normal penalty factors result in large (unrealistic) interpenetration between bodies. Large values, on the other hand, minimize interpenetration between bodies. However, too large values can lead to an ill-conditioned numerical problem, causing non-convergence of the nonlinear solution. Tangential penalty factors are related to the elastic-slip between surfaces, i.e., a large tangential penalty factor tends to represent Coulomb's friction law more precisely (no slip until tangential forces are greater than a certain limit), a lower penalty factor relaxes this condition, allowing slippage before the limit is reached. One can observe that penalty parameters can also have a physical meaning if associated with the mechanical properties of the materials in contact. This will be better understood in Chapter 6.

3.5. Master-surface to master-surface contact formulation

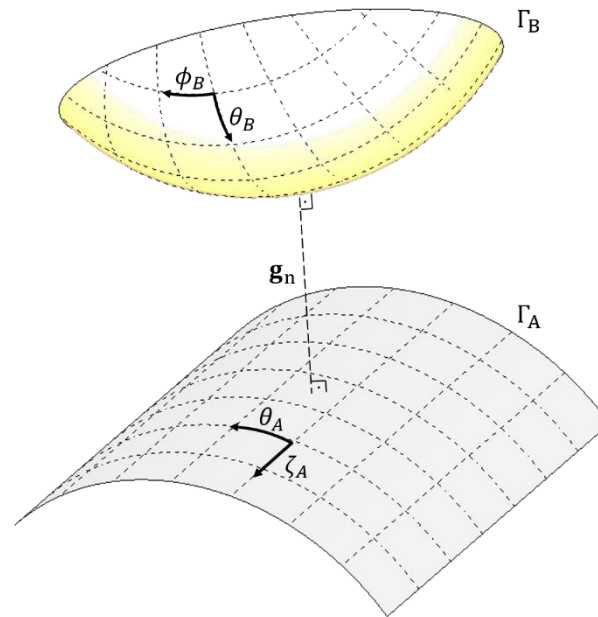
By author's knowledge, the seminal idea of the master-surface to master-surface contact formulation (from now on called simply "master-master") was first introduced in 1997 [65], in the context of beam-to-beam contact. In that work, it was

presented a contact formulation where the distinction between master and slave surfaces is avoided. That can be seen as a “master-curve to master-curve” contact formulation. One can see the inclusion of friction in [66], by the same authors. Recently, the technique was generalized into a master-surface to master-surface general pointwise contact formulation, by using super-elliptical extruded parameterized surfaces [29] [30], which may represent the surface of a beam-like structure. This generalization has expanded the range of applicability of the formulation, which is now employed in present work.

As shown previously in this chapter, in the traditional master-slave approach, to establish contact between bodies, one has to elect slave points in a surface to interact with their normal projections in another (parameterized) surface. In the master-master approach, on the other hand, there is no need to elect slave points. Both surfaces candidate to contact are parameterized using convective coordinates, i.e., both surfaces are described as functions of material coordinates that are attached to the body, and then, that deform with the body. Moreover, since these surfaces may be related to moving bodies, they also have to be written as functions of the generalized coordinates of the problem.

In Figure 3.7, two parameterized surfaces, Γ_A and Γ_B are shown. These surfaces are functions of a set of convective coordinates, \mathbf{c}_A and \mathbf{c}_B , and a set of generalized coordinates, \mathbf{d}_A and \mathbf{d}_B .

Figure 3.7: Parameterized surfaces candidate to contact.



Source: [67]

This dependence can be expressed as:

$$\Gamma_\beta = \Gamma_\beta(\mathbf{c}_\beta, \mathbf{d}_\beta) \quad \text{for } \beta = A, B. \quad (3.20)$$

Noticing from Figure 3.7 that:

$$\begin{aligned} \mathbf{c}_A &= [\zeta_A \quad \theta_A]^T \text{ and} \\ \mathbf{c}_B &= [\phi_B \quad \theta_B]^T. \end{aligned} \quad (3.21)$$

Vectors \mathbf{d}_A and \mathbf{d}_B represent the generalized coordinates of the problem, e.g. the vector of displacements and rotations in a finite element formulation.

Once both surfaces candidate to contact are parameterized, a normal (vector) gap function can be defined as:

$$\mathbf{g}_n = \mathbf{g}_n(\mathbf{c}, \mathbf{d}) = \Gamma_A - \Gamma_B, \quad (3.22)$$

where \mathbf{c} and \mathbf{d} are vectors collecting all the convective coordinates and all degrees of freedom of the problem, respectively. We call attention to the fact that the normal gap function in the master-master formulation (expressed in equation (3.22)) differs from the traditional gap function presented in section 3.2.1. Here, we have a vector gap function, which can be visualized in Figure 3.7. Therefore, it is possible to write a scalar quantity to measure the distance between the surfaces by:

$$g_n = \|\mathbf{g}_n\|. \quad (3.23)$$

The most important simplification present in the master-master contact formulation is the assumption of a pointwise interaction, i.e., the contact action is represented by an equivalent point load. In order to spread the contact action over a region, it is necessary to define several sub-surfaces, which will have their own contact points. Another hypothesis assumed in the formulation, as presented here, is the fact that surfaces candidate to contact must be convex. This ensures the existence of a unique pair of points representing the minimum distance between the surfaces. By assuming these two hypotheses, i.e., a pointwise interaction and convex surfaces, it is possible to impose orthogonality conditions and to establish a local contact problem, expressed as:

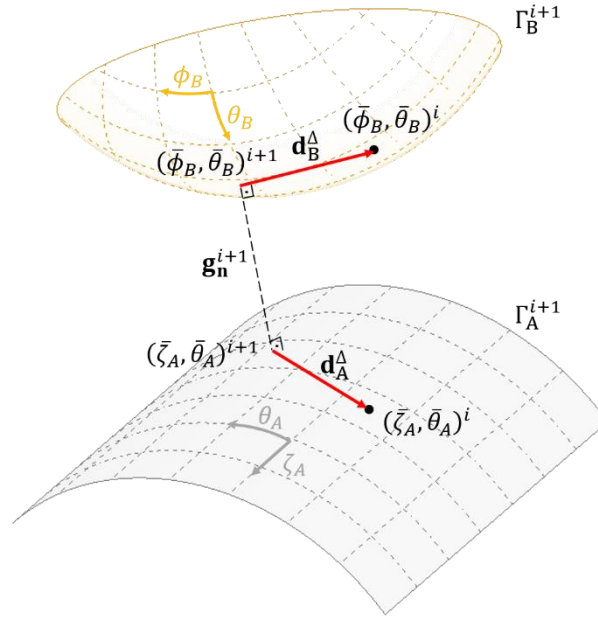
$$\mathbf{r} = \begin{bmatrix} \Gamma_{A, \zeta_A} \cdot \mathbf{g}_n \\ \Gamma_{A, \theta_A} \cdot \mathbf{g}_n \\ -\Gamma_{B, \phi_B} \cdot \mathbf{g}_n \\ -\Gamma_{B, \theta_B} \cdot \mathbf{g}_n \end{bmatrix} = \mathbf{0}_4. \quad (3.24)$$

In equation (3.24), the dot products between the normal vector gap function and the tangential vectors at the contact point are null, this means that we are imposing that the normal gap function is orthogonal to both surfaces at the contact point. For the case when there is no penetration between bodies, the points that satisfy this condition represent the closest points between the two surfaces. Ensuring that a good initial guess is provided, equation (3.24) can be solved for ζ_A , θ_A , ϕ_B and θ_B very efficiently

by using the Newton-Raphson method. At the end, one obtains a set of convective coordinates that define a gap vector \mathbf{g}_n orthogonal to both master surfaces. By doing that, we may evaluate if there is penetration or not of master surfaces and quantify it. In [29] and [30], the authors highlight the need of more elaborate methods, based on optimization techniques, to handle non-convex cases.

The main advantage of the master-master contact formulation is that once the minimum distance problem is solved, only one gap value has to be evaluated. This differs from the traditional master-slave approach, where multiple slave points interact with a master surface resulting in multiple gap values being monitored all the time.

For tangential direction, the tangential gap function is completely redefined in this formulation. In Figure 3.8 two surfaces candidate to contact are shown. Assuming an updated Lagrangian description, the right-superscript “ $i + 1$ ” in this figure refers to the current configuration. A right-superscript “ i ”, on the other hand, represents quantities from the last known configuration.

Figure 3.8: Parameterized surfaces candidate to contact in the configuration “ $i + 1$ ”.

Source: [67]

In this configuration, one may obtain position vectors associated with material points in both surfaces of the current solution of (3.24). Additionally, it is possible to obtain the material point positions in both surfaces associated with the previous solution of the local contact problem (mapped using convective coordinates from configuration “ i ”) in the new, current configuration “ $i + 1$ ”. Thus, it is possible to define vectors in both surfaces, at current configuration, that point from the current solution of the local contact problem to the previous one. These vectors can be written as:

$$\mathbf{d}_A^\Delta = \Gamma_A(\mathbf{c}^i, \mathbf{d}^{i+1}) - \Gamma_A(\mathbf{c}^{i+1}, \mathbf{d}^{i+1}) \text{ and}$$

$$\mathbf{d}_B^\Delta = \Gamma_B(\mathbf{c}^i, \mathbf{d}^{i+1}) - \Gamma_B(\mathbf{c}^{i+1}, \mathbf{d}^{i+1}).$$

(3.25)

By using the definition of exterior normal of one of the parameterized surfaces, for example of surface Γ_B , given by:

$$\mathbf{n}_B^{i+1} = \frac{\Gamma_{B,\theta_B}^{i+1} \times \Gamma_{B,\phi_B}^{i+1}}{\|\Gamma_{B,\theta_B}^{i+1} \times \Gamma_{B,\phi_B}^{i+1}\|},$$

(3.26)

it is possible to define an incremental tangential gap \mathbf{g}_T^Δ , which captures the relative sliding tendency between surfaces:

$$\mathbf{g}_T^\Delta = (\mathbf{d}_A^\Delta - \mathbf{d}_B^\Delta) - [(\mathbf{d}_A^\Delta - \mathbf{d}_B^\Delta) \cdot \mathbf{n}_B^{i+1}] \mathbf{n}_B^{i+1}. \quad (3.27)$$

Then, the tangential gap function can be defined as:

$$\mathbf{g}_T^{i+1} = \mathbf{g}_T^\Delta + \mathbf{Q}^\Delta \mathbf{g}_T^i. \quad (3.28)$$

In expression (3.28), \mathbf{Q}^Δ is a rotation tensor used to update the previous tangential gap to the next configuration, i.e. from configuration “ i ” to configuration “ $i + 1$ ”. By defining the tangential gap function in this way, the effect of rigid body rotation is eliminated from the contact pair, ensuring the objectivity of the measure used to quantify friction (or its tendency). Details of this operator can be found in remark 2 of Ref. [30].

Normal and tangential gap functions are the basis of the master-master gap measurement, which are later employed to establish contact potential contributions to the model, such as their associated weak forms and consistent linearization. To compute the contact forces, one can use, for example, a penalty approach. It is also necessary to employ a constitutive law to decide between sticking/slipping conditions and the Coulomb’s friction law is the most popular choice.

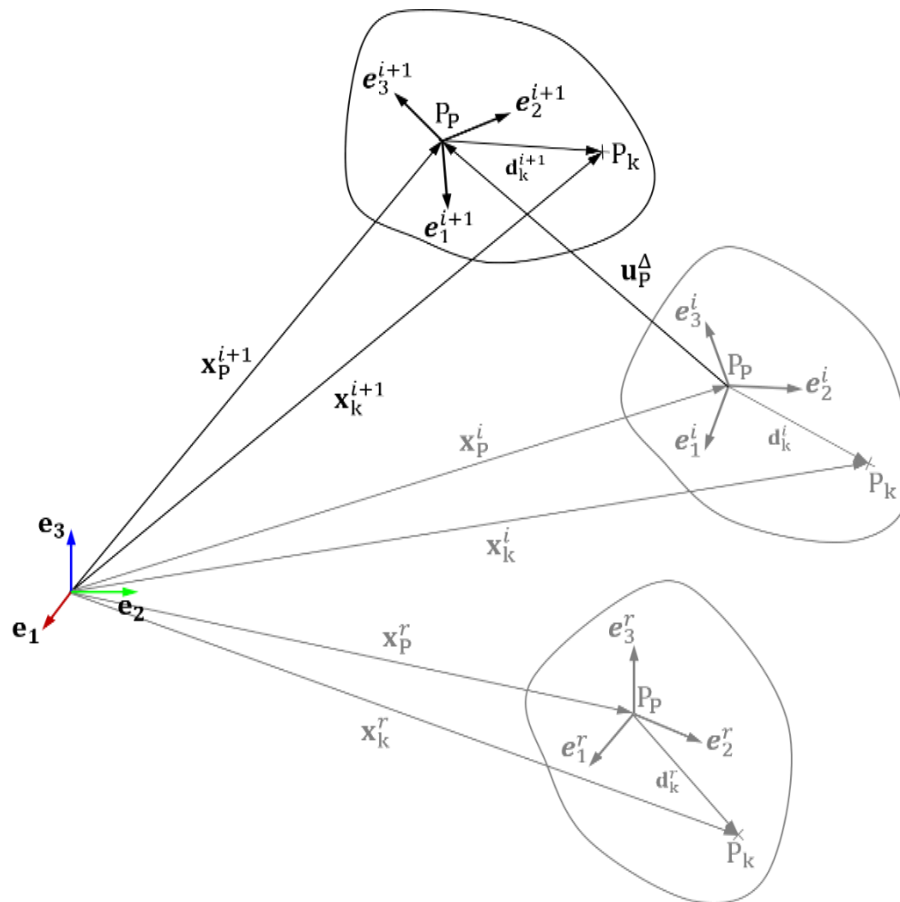
4. RIGID BODY ELEMENT FORMULATION

4.1. Inertial contribution

Rigid body elements are well known in the context of multibody dynamics (MBD). However, they are also very useful in finite element analyses. In engineering systems, it is common to have components which are significantly more rigid than the others. Moreover, there are components, or some regions of a component, which have to be included in a model only because of its inertial contribution, i.e., there are some parts which are important to the overall dynamic behaviour of the system, but stresses, strains and wave propagation can be disregarded for these parts. In such situation, the use of rigid body elements usually represents the best compromise between computational cost and accuracy. Instead of using traditional finite element meshes for the whole model, one can replace the meshes of those “rigid” components by a single node rigid body element, which accounts for inertia and mass properties and can be connected to the rest of the model.

Let us now develop the inertial contributions for such kind of rigid body element. Reinforcing that it is a one-node element, with six degrees of freedom, accounting for mass and inertia properties. Furthermore, this single node can be positioned anywhere in a finite element model. This means that, differently from traditional approaches, in the present formulation the rigid body pole (origin) does not need to be coincident with the centre of mass of the body.

Figure 4.1: Rigid body movement in a three-dimensional space.



Source: [67]

We want to describe a general rigid body movement. For that, we first define a reference configuration. Quantities associated with it will be here referenced by a right-superscript “ r ”. It is assumed an updated Lagrangian description. Last known configuration is denoted by a right-superscript “ i ”, while the next configuration (still unknown) is denoted by right-superscript “ $i + 1$ ”. In Figure 4.1, the rigid body configurations are illustrated.

Any generic material point of the rigid body can be mapped to the current configuration “ $i + 1$ ” using the rotation tensor \mathbf{Q}_k^{i+1} . Therefore, one can write the position vector for any material point P_k as:

$$\mathbf{x}_k^{i+1} = \mathbf{x}_P^{i+1} + \mathbf{Q}_k^{i+1} \mathbf{d}_k^r. \quad (4.1)$$

For the present work the rotation description by Rodrigues rotation vector was used (see Appendix B). Moreover, in order to overcome singularities for rotations $\theta_k = \pm\pi$, we have made a choice of an updated Lagrangian scheme. Then, one can define consecutive mappings between intermediate configurations, referred as “ i ” and “ $i + 1$ ”, represented in Figure 4.1. In this context, one may define updating quantities with an upper-right index “ Δ ”. Then, it is possible to write the mapping:

$$\mathbf{d}_k^{i+1} = \mathbf{Q}_k^\Delta \mathbf{d}_k^i, \quad (4.2)$$

which may be used together with

$$\mathbf{d}_k^i = \mathbf{Q}_k^i \mathbf{d}_k^r, \quad (4.3)$$

so that the rotation tensor \mathbf{Q}_k^{i+1} that appears in expression (4.1) is a compound tensor, given by:

$$\mathbf{Q}_k^{i+1} = \mathbf{Q}_k^\Delta \mathbf{Q}_k^i. \quad (4.4)$$

Using always small, but finite, rotation magnitudes to evaluate \mathbf{Q}_k^Δ avoids the mentioned possible singularities in rotation tensor. Then, we may define the Rodrigues rotation vector $\boldsymbol{\alpha}_k^\Delta = \alpha_k^\Delta \mathbf{e}_k^\Delta$, to be used to evaluate \mathbf{Q}_k^Δ , simply using it in Rodrigues’ expression (see Appendix B).

In Figure 4.1, P_P is called “pilot point”. The connection between P_P and general material points P_k in a model will be discussed later, in the next section. This point will be taken as the origin of a local frame, attached to the rigid body. The choice of this point is absolutely arbitrary, leading to a general formulation, as will be discussed here. The point can be chosen even out of the rigid body physical domain.

Using the incremental displacement \mathbf{u}_P^Δ , shown in Figure 4.1, it is possible to write:

$$\mathbf{x}_P^{i+1} = \mathbf{x}_P^i + \mathbf{u}_P^\Delta. \quad (4.5)$$

From equation (4.1), the velocity of a generic point in the rigid body can be written as:

$$\dot{\mathbf{x}}_k^{i+1} = \dot{\mathbf{x}}_P^{i+1} + \mathbf{d}_k^{i+1}, \quad (4.6)$$

where a dot over a variable indicates its time-derivative. Expression (4.6) can be rewritten using the instantaneous angular velocity of the body:

$$\dot{\mathbf{x}}_k^{i+1} = \dot{\mathbf{x}}_P^{i+1} + (\boldsymbol{\omega} \times \mathbf{d}_k^{i+1}). \quad (4.7)$$

Equation (4.7) is valid because:

$$\mathbf{d}_k^{i+1} = \mathbf{Q}_k^\Delta \mathbf{d}_k^i \therefore \mathbf{d}_k^i = \mathbf{Q}_k^{\Delta T} \mathbf{d}_k^{i+1} \text{ and} \quad (4.8)$$

$$\dot{\mathbf{d}}_k^{i+1} = \dot{\mathbf{Q}}_k^\Delta \mathbf{d}_k^i = \dot{\mathbf{Q}}_k^\Delta \mathbf{Q}_k^{\Delta T} \mathbf{d}_k^{i+1} = \boldsymbol{\Omega} \mathbf{d}_k^{i+1} = \boldsymbol{\omega} \times \mathbf{d}_k^{i+1}, \quad (4.9)$$

where $\boldsymbol{\omega}$ is the axial of $\boldsymbol{\Omega}$ (see Appendix A), which is, by definition, the spin vector (angular velocity).

From classical mechanics, one can write the kinetic energy for the rigid body as:

$$T = \frac{1}{2} \int_V \rho \dot{\mathbf{x}}_k^{i+1} \cdot \dot{\mathbf{x}}_k^{i+1} dV. \quad (4.10)$$

Using (4.7) in (4.10), we have:

$$T = \frac{1}{2} \int_V \rho \left(\dot{\mathbf{x}}_P^{i+1} + (\boldsymbol{\omega} \times \mathbf{d}_k^{i+1}) \right) \cdot \left(\dot{\mathbf{x}}_P^{i+1} + (\boldsymbol{\omega} \times \mathbf{d}_k^{i+1}) \right) dV, \quad (4.11)$$

with ρ being the volumetric mass density function of the material considered for the body.

The kinetic energy T can be decomposed into three parcels, they are the well-known translational, rotational and coupling terms of the kinetic energy: $T = T_1 + T_2 + T_3$, with:

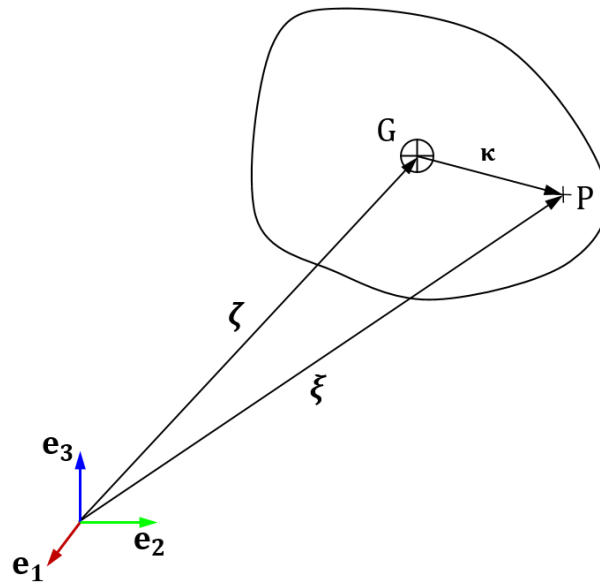
$$T_1 = \frac{1}{2} \int_V \rho \dot{\mathbf{x}}_P^{i+1} \cdot \dot{\mathbf{x}}_P^{i+1} dV,$$

$$T_2 = \frac{1}{2} \int_V \rho (\boldsymbol{\omega} \times \mathbf{d}_k^{i+1}) \cdot (\boldsymbol{\omega} \times \mathbf{d}_k^{i+1}) dV \text{ and} \quad (4.12)$$

$$T_3 = \int_V \rho \dot{\mathbf{x}}_P^{i+1} \cdot (\boldsymbol{\omega} \times \mathbf{d}_k^{i+1}) dV.$$

In this work, since there are no restrictions regarding the choice of the “pilot node”, the coupling term T_3 may be non-null. Naturally, if one chooses the “pilot node” coincident with the centre of mass of the body, then, T_3 becomes null and translational and rotational terms are decoupled. At this stage, it is convenient to introduce Figure 4.2.

Figure 4.2: Centre of mass of a rigid body.



Source: Author

By definition, the weighted average of vectors $\boldsymbol{\kappa}$ around the centre of mass is null. This can be shown as follows: in Figure 4.2, the position of an arbitrary point P, in terms of the centre of mass, is given by:

$$\boldsymbol{\xi} = \boldsymbol{\zeta} + \boldsymbol{\kappa}. \quad (4.13)$$

Using the definition of centre of mass, $\boldsymbol{\zeta}$ can be expressed as:

$$\boldsymbol{\zeta} = \frac{1}{m} \int_V \rho \boldsymbol{\xi} dV, \quad (4.14)$$

with m being the total mass of the body.

Using (4.13) in (4.14), we have:

$$\boldsymbol{\zeta} = \frac{1}{m} \int_V \rho (\boldsymbol{\zeta} + \boldsymbol{\kappa}) dV = \boldsymbol{\zeta} + \frac{1}{m} \int_V \rho \boldsymbol{\kappa} dV. \quad (4.15)$$

From equation (4.15), it is clear that $\int_V \rho \mathbf{k} dV$ has to be null. Therefore, it is possible to say that when the pole (pilot node) coincides with the centre of mass of the body, the coupling term of the kinetic energy is also null. This hypothesis is not assumed in the present work, so that any possible position can be chosen as a pilot point.

To obtain the weak form contribution due to rigid body inertial loads, one can use the artifice of evaluating \dot{T} , i.e., the time-derivative of the kinetic energy. For example, from equation (4.5) one can notice that $\dot{\mathbf{x}}_p^{i+1} = \dot{\mathbf{u}}_p^\Delta$ (= $\dot{\mathbf{u}}$ to simplify the notation), and then, T_1 can be rewritten as:

$$T_1 = \frac{1}{2} \int_V \rho \dot{\mathbf{x}}_p^{i+1} \cdot \dot{\mathbf{x}}_p^{i+1} dV = \frac{1}{2} m \dot{\mathbf{x}}_p^{i+1} \cdot \dot{\mathbf{x}}_p^{i+1} = \frac{1}{2} m \dot{\mathbf{u}} \cdot \dot{\mathbf{u}}, \quad (4.16)$$

such that,

$$\dot{T}_1 = \frac{dT_1}{dt} = m \dot{\mathbf{u}} \cdot \dot{\mathbf{u}} = m \dot{\mathbf{u}} \cdot \frac{d\mathbf{u}_p^\Delta}{dt} \therefore dT_1 = m \dot{\mathbf{u}} \cdot d\mathbf{u}_p^\Delta. \quad (4.17)$$

Then, one can replace d by δ , obtaining:

$$\delta T_1 = m \dot{\mathbf{u}} \cdot \delta \mathbf{u}_p^\Delta. \quad (4.18)$$

Employing the same approach, it is possible to obtain δT_2 and δT_3 , as follows.

$$\begin{aligned} \dot{T}_2 &= \frac{dT_2}{dt} = \int_V \rho (\boldsymbol{\omega} \times \mathbf{d}_k^{i+1}) \cdot (\boldsymbol{\omega} \times \mathbf{d}_k^{i+1}) dV \\ &+ \int_V \rho (\dot{\boldsymbol{\omega}} \times \mathbf{d}_k^{i+1}) \cdot (\boldsymbol{\omega} \times \mathbf{d}_k^{i+1}) dV. \end{aligned} \quad (4.19)$$

Naming the first integral in (4.19) as \dot{T}_{2a} , it can be rewritten replacing \mathbf{d}_k^{i+1} by $(\boldsymbol{\omega} \times \mathbf{d}_k^{i+1})$, as we already did in (4.7).

$$\begin{aligned}
\dot{T}_{2a} &= \int_V \rho (\boldsymbol{\omega} \times \mathbf{d}_k^{i+1}) \cdot (\boldsymbol{\omega} \times \mathbf{d}_k^{i+1}) dV \\
&= \int_V \rho \left(\boldsymbol{\omega} \times (\boldsymbol{\omega} \times \mathbf{d}_k^{i+1}) \right) \cdot (\boldsymbol{\omega} \times \mathbf{d}_k^{i+1}) dV.
\end{aligned} \tag{4.20}$$

In addition, this cross product can be represented in a different form by using $\mathbf{D}_k^{i+1} = \text{skew}(\mathbf{d}_k^{i+1})$ (see Appendix A):

$$\begin{aligned}
\dot{T}_{2a} &= \int_V \rho \left(\boldsymbol{\omega} \times (\mathbf{D}_k^{i+1} \boldsymbol{\omega}) \right) \cdot (\mathbf{D}_k^{i+1} \boldsymbol{\omega}) dV \\
&= \int_V -\rho \left((\mathbf{D}_k^{i+1} \boldsymbol{\omega}) \times \boldsymbol{\omega} \right) \cdot (\mathbf{D}_k^{i+1} \boldsymbol{\omega}) dV \\
&= \int_V -\rho \boldsymbol{\omega}^T \mathbf{D}_k^{i+1 T} \left((\mathbf{D}_k^{i+1} \boldsymbol{\omega}) \times \boldsymbol{\omega} \right) dV = \int_V \rho (\mathbf{D}_k^{i+1} \mathbf{D}_k^{i+1} \boldsymbol{\omega}) \times \boldsymbol{\omega} \cdot \boldsymbol{\omega} dV.
\end{aligned} \tag{4.21}$$

After performing such algebraic work, \dot{T}_{2a} can be written as:

$$\dot{T}_{2a} = \int_V -\rho \boldsymbol{\omega} \times \left((\mathbf{D}_k^{i+1})^2 \boldsymbol{\omega} \right) \cdot \boldsymbol{\omega} dV = \boldsymbol{\omega} \times \int_V -\rho (\mathbf{D}_k^{i+1})^2 dV \boldsymbol{\omega} \cdot \boldsymbol{\omega}, \tag{4.22}$$

where we can identify $-\int_V \rho (\mathbf{D}_k^{i+1})^2 dV$ as being the inertia tensor of the rigid body (see e.g.: [68]), named \mathbf{J} , thus:

$$\dot{T}_{2a} = \boldsymbol{\omega} \times \mathbf{J}^{i+1} \boldsymbol{\omega} \cdot \boldsymbol{\omega}. \tag{4.23}$$

Employing the same steps for the second integral in (4.19), \dot{T}_{2b} , we have:

$$\begin{aligned}
\dot{T}_{2b} &= \int_V \rho (\dot{\boldsymbol{\omega}} \times \mathbf{d}_k^{i+1}) \cdot (\boldsymbol{\omega} \times \mathbf{d}_k^{i+1}) dV = \int_V \rho (\mathbf{D}_k^{i+1} \dot{\boldsymbol{\omega}}) \cdot (\mathbf{D}_k^{i+1} \boldsymbol{\omega}) dV \\
&= \int_V \rho \boldsymbol{\omega}^T \mathbf{D}_k^{i+1 T} \mathbf{D}_k^{i+1} \dot{\boldsymbol{\omega}} dV \\
&= \int_V -\rho \boldsymbol{\omega}^T \mathbf{D}_k^{i+1} \mathbf{D}_k^{i+1} \dot{\boldsymbol{\omega}} dV = \boldsymbol{\omega} \cdot \int_V -\rho (\mathbf{D}_k^{i+1})^2 dV \dot{\boldsymbol{\omega}}.
\end{aligned} \tag{4.24}$$

The inertia tensor appears once more in expression (4.24), therefore:

$$\dot{T}_{2b} = \mathbf{J}^{i+1} \dot{\boldsymbol{\omega}} \cdot \boldsymbol{\omega}. \quad (4.25)$$

With (4.23) and (4.25), the time-derivative of the rotational term of kinetic energy is given by:

$$\dot{T}_2 = \dot{T}_{2a} + \dot{T}_{2b} = \boldsymbol{\omega} \times \mathbf{J}^{i+1} \boldsymbol{\omega} \cdot \boldsymbol{\omega} + \mathbf{J}^{i+1} \dot{\boldsymbol{\omega}} \cdot \boldsymbol{\omega}. \quad (4.26)$$

Notice that \mathbf{J}^{i+1} can be written in terms of the reference configuration as:

$$\mathbf{J}^{i+1} = \mathbf{Q}_k^{i+1} \mathbf{J}^r \mathbf{Q}_k^{i+1 T}. \quad (4.27)$$

Using the relation $\boldsymbol{\omega} = \boldsymbol{\Xi}_P \dot{\boldsymbol{\alpha}}$, where $\dot{\boldsymbol{\alpha}} = \dot{\boldsymbol{\alpha}}_P^\Delta$, and $\boldsymbol{\Xi}_P$ (see e.g.: [69]):

$$\boldsymbol{\Xi}_P = \frac{4}{4 + \alpha_P^\Delta \cdot \alpha_P^\Delta} \left(\mathbf{I} + \frac{1}{2} \mathbf{A}_P \right). \quad (4.28)$$

The weak form of T_2 is finally written as:

$$\begin{aligned} \dot{T}_2 &= \frac{dT_2}{dt} = \boldsymbol{\omega} \times \mathbf{J}^{i+1} \boldsymbol{\omega} \cdot \boldsymbol{\Xi}_P \dot{\boldsymbol{\alpha}} + \mathbf{J}^{i+1} \dot{\boldsymbol{\omega}} \cdot \boldsymbol{\Xi}_P \dot{\boldsymbol{\alpha}} \\ &= \dot{\boldsymbol{\alpha}}^T \boldsymbol{\Xi}_P^T (\boldsymbol{\omega} \times \mathbf{J}^{i+1} \boldsymbol{\omega}) + \dot{\boldsymbol{\alpha}}^T \boldsymbol{\Xi}_P^T \mathbf{J}^{i+1} \dot{\boldsymbol{\omega}} = (\boldsymbol{\Xi}_P^T (\boldsymbol{\omega} \times \mathbf{J}^{i+1} \boldsymbol{\omega}) + \boldsymbol{\Xi}_P^T \mathbf{J}^{i+1} \dot{\boldsymbol{\omega}}) \cdot \dot{\boldsymbol{\alpha}} \\ &= (\boldsymbol{\Xi}_P^T (\boldsymbol{\omega} \times \mathbf{J}^{i+1} \boldsymbol{\omega}) + \boldsymbol{\Xi}_P^T \mathbf{J}^{i+1} \dot{\boldsymbol{\omega}}) \cdot \frac{d\boldsymbol{\alpha}_P^\Delta}{dt} \\ \therefore dT_2 &= (\boldsymbol{\Xi}_P^T (\boldsymbol{\omega} \times \mathbf{J}^{i+1} \boldsymbol{\omega}) + \boldsymbol{\Xi}_P^T \mathbf{J}^{i+1} \dot{\boldsymbol{\omega}}) \cdot d\boldsymbol{\alpha}_P^\Delta. \end{aligned} \quad (4.29)$$

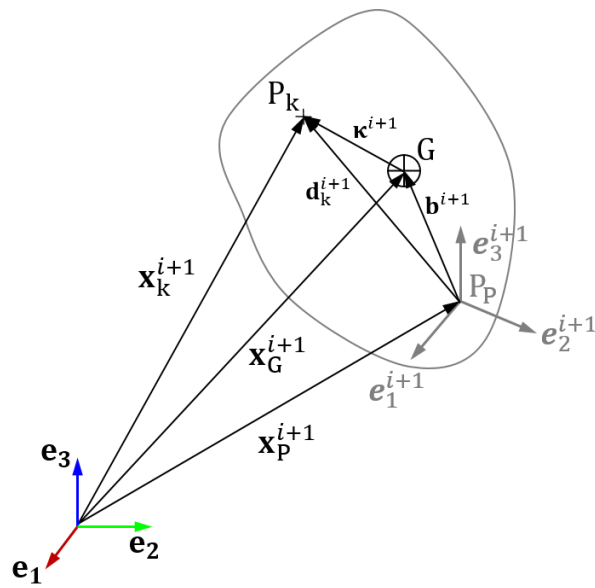
Then, one can write:

$$\delta T_2 = (\boldsymbol{\Xi}_P^T (\boldsymbol{\omega} \times \mathbf{J}^{i+1} \boldsymbol{\omega}) + \boldsymbol{\Xi}_P^T \mathbf{J}^{i+1} \dot{\boldsymbol{\omega}}) \cdot \delta \boldsymbol{\alpha}_P^\Delta. \quad (4.30)$$

By introducing Figure 4.3 and noticing that $\dot{\mathbf{x}}_P^{i+1} = \dot{\mathbf{u}}_P^\Delta$ ($= \dot{\mathbf{u}}$ to simplify the notation), it is possible to rewrite T_3 as:

$$\begin{aligned}
T_3 &= \int_V \rho \dot{\mathbf{u}} \cdot (\boldsymbol{\omega} \times \mathbf{d}_k^{i+1}) dV = \int_V \rho (\boldsymbol{\omega} \times \mathbf{d}_k^{i+1}) \cdot \dot{\mathbf{u}} dV \\
&= \boldsymbol{\omega} \times \int_V \rho \mathbf{d}_k^{i+1} dV \cdot \dot{\mathbf{u}}
\end{aligned} \tag{4.31}$$

Figure 4.3: Arbitrary "pilot point".



Source: [67]

As mentioned previously, the weighted average of vectors $\boldsymbol{\kappa}$ around the centre of mass results null. Using additional information provided in Figure 4.3, the term $\int_V \rho \mathbf{d}_k^{i+1} dV$ in (4.31) can be rewritten as:

$$\int_V \rho \mathbf{d}_k^{i+1} dV = \int_V \rho \mathbf{b}^{i+1} dV + \int_V \rho \boldsymbol{\kappa}^{i+1} dV = m \mathbf{b}^{i+1}. \tag{4.32}$$

Therefore, T_3 simplifies to:

$$T_3 = \boldsymbol{\omega} \times m \mathbf{b}^{i+1} \cdot \dot{\mathbf{u}}. \tag{4.33}$$

Then, it is possible to compute \dot{T}_3 :

$$\begin{aligned}\dot{T}_3 &= \frac{dT_3}{dt} = m(\dot{\boldsymbol{\omega}} \times \mathbf{b}^{i+1} \cdot \dot{\mathbf{u}} + \boldsymbol{\omega} \times \dot{\mathbf{b}}^{i+1} \cdot \dot{\mathbf{u}} + \boldsymbol{\omega} \times \mathbf{b}^{i+1} \cdot \ddot{\mathbf{u}}) \\ &= m(\dot{\boldsymbol{\omega}} \times \mathbf{b}^{i+1} \cdot \dot{\mathbf{u}} + \boldsymbol{\omega} \times (\boldsymbol{\omega} \times \mathbf{b}^{i+1}) \cdot \dot{\mathbf{u}} + \boldsymbol{\omega} \times \mathbf{b}^{i+1} \cdot \ddot{\mathbf{u}}).\end{aligned}\quad (4.34)$$

Therefore,

$$\begin{aligned}\dot{T}_3 &= \frac{dT_3}{dt} \\ &= m(\dot{\mathbf{u}} \cdot (\dot{\boldsymbol{\omega}} \times \mathbf{b}^{i+1}) + \dot{\mathbf{u}} \cdot (\boldsymbol{\omega} \times (\boldsymbol{\omega} \times \mathbf{b}^{i+1})) + (\mathbf{b}^{i+1} \times \ddot{\mathbf{u}}) \cdot \boldsymbol{\omega}) \\ &= m(\dot{\mathbf{u}} \cdot (\dot{\boldsymbol{\omega}} \times \mathbf{b}^{i+1}) + \dot{\mathbf{u}} \cdot (\boldsymbol{\omega} \times (\boldsymbol{\omega} \times \mathbf{b}^{i+1})) + \dot{\boldsymbol{\alpha}}^T \boldsymbol{\Xi}_P^T (\mathbf{b}^{i+1} \times \ddot{\mathbf{u}})) \\ &= m(\dot{\mathbf{u}} \cdot (\dot{\boldsymbol{\omega}} \times \mathbf{b}^{i+1}) + \dot{\mathbf{u}} \cdot (\boldsymbol{\omega} \times (\boldsymbol{\omega} \times \mathbf{b}^{i+1})) + \boldsymbol{\Xi}_P^T (\mathbf{b}^{i+1} \times \ddot{\mathbf{u}}) \cdot \dot{\boldsymbol{\alpha}}),\end{aligned}\quad (4.35)$$

which makes it possible to write:

$$\begin{aligned}\dot{T}_3 &= \frac{dT_3}{dt} \\ &= m\left(\frac{d\mathbf{u}_P^\Delta}{dt} \cdot (\dot{\boldsymbol{\omega}} \times \mathbf{b}^{i+1}) + \frac{d\mathbf{u}_P^\Delta}{dt} \cdot (\boldsymbol{\omega} \times (\boldsymbol{\omega} \times \mathbf{b}^{i+1})) + \boldsymbol{\Xi}_P^T (\mathbf{b}^{i+1} \times \ddot{\mathbf{u}}) \cdot \frac{d\boldsymbol{\alpha}_P^\Delta}{dt}\right) \\ \therefore dT_3 &= m\left(d\mathbf{u}_P^\Delta \cdot (\dot{\boldsymbol{\omega}} \times \mathbf{b}^{i+1}) + d\mathbf{u}_P^\Delta \cdot (\boldsymbol{\omega} \times (\boldsymbol{\omega} \times \mathbf{b}^{i+1})) + \boldsymbol{\Xi}_P^T (\mathbf{b}^{i+1} \times \ddot{\mathbf{u}}) \cdot d\boldsymbol{\alpha}_P^\Delta\right).\end{aligned}\quad (4.36)$$

Finally, one can write:

$$\begin{aligned}\delta T_3 &= m\left(\left((\dot{\boldsymbol{\omega}} \times \mathbf{b}^{i+1}) + (\boldsymbol{\omega} \times (\boldsymbol{\omega} \times \mathbf{b}^{i+1}))\right) \cdot \delta \mathbf{u}_P^\Delta + \left(\boldsymbol{\Xi}_P^T (\mathbf{b}^{i+1} \times \ddot{\mathbf{u}})\right) \cdot \delta \boldsymbol{\alpha}_P^\Delta\right).\end{aligned}\quad (4.37)$$

Putting it all together, the weak form contribution due to the kinetic energy is given by:

$$\begin{aligned}
\delta T &= \delta T_1 + \delta T_2 + \delta T_3 \\
&= m\ddot{\mathbf{u}} \cdot \delta \mathbf{u}_P^\Delta + \left(\boldsymbol{\Xi}_P^T (\boldsymbol{\omega} \times \mathbf{J}^{i+1} \boldsymbol{\omega}) + \boldsymbol{\Xi}_P^T \mathbf{J}^{i+1} \dot{\boldsymbol{\omega}} \right) \cdot \delta \boldsymbol{\alpha}_P^\Delta + m \left(\left((\dot{\boldsymbol{\omega}} \times \mathbf{b}^{i+1}) + \right. \right. \\
&\quad \left. \left. (\boldsymbol{\omega} \times (\boldsymbol{\omega} \times \mathbf{b}^{i+1})) \right) \right) \cdot \delta \mathbf{u}_P^\Delta + \left(\boldsymbol{\Xi}_P^T (\mathbf{b}^{i+1} \times \ddot{\mathbf{u}}) \right) \cdot \delta \boldsymbol{\alpha}_P^\Delta.
\end{aligned} \tag{4.38}$$

Equation (4.38) can be re-organized as follows:

$$\begin{aligned}
\delta T &= m \left(\ddot{\mathbf{u}} + \left((\dot{\boldsymbol{\omega}} \times \mathbf{b}^{i+1}) + (\boldsymbol{\omega} \times (\boldsymbol{\omega} \times \mathbf{b}^{i+1})) \right) \right) \cdot \delta \mathbf{u}_P^\Delta + \left(\boldsymbol{\Xi}_P^T (\boldsymbol{\omega} \times \right. \\
&\quad \left. \mathbf{J}^{i+1} \boldsymbol{\omega}) + \boldsymbol{\Xi}_P^T \mathbf{J}^{i+1} \dot{\boldsymbol{\omega}} \right) + m \left(\boldsymbol{\Xi}_P^T (\mathbf{b}^{i+1} \times \ddot{\mathbf{u}}) \right) \cdot \delta \boldsymbol{\alpha}_P^\Delta.
\end{aligned} \tag{4.39}$$

In a much more compact notation:

$$\delta T = \mathbf{f}_u \cdot \delta \mathbf{u}_P^\Delta + \mathbf{f}_\alpha \cdot \delta \boldsymbol{\alpha}_P^\Delta = \begin{bmatrix} \mathbf{f}_u \\ \mathbf{f}_\alpha \end{bmatrix} \cdot \begin{bmatrix} \delta \mathbf{u}_P^\Delta \\ \delta \boldsymbol{\alpha}_P^\Delta \end{bmatrix}, \tag{4.40}$$

with,

$$\begin{aligned}
\mathbf{f}_u &= m \left(\ddot{\mathbf{u}} + \left((\dot{\boldsymbol{\omega}} \times \mathbf{b}^{i+1}) + (\boldsymbol{\omega} \times (\boldsymbol{\omega} \times \mathbf{b}^{i+1})) \right) \right) \text{ and} \\
\mathbf{f}_\alpha &= \left(\boldsymbol{\Xi}_P^T (\boldsymbol{\omega} \times \mathbf{J}^{i+1} \boldsymbol{\omega}) + \boldsymbol{\Xi}_P^T \mathbf{J}^{i+1} \dot{\boldsymbol{\omega}} \right) + m \left(\boldsymbol{\Xi}_P^T (\mathbf{b}^{i+1} \times \ddot{\mathbf{u}}) \right).
\end{aligned} \tag{4.41}$$

Linearization of the weak form is necessary in order to ensure quadratic convergence of the Newton-Raphson method in a nonlinear finite element framework, and then, we have:

$$\Delta(\delta T) = \begin{bmatrix} \Delta \mathbf{f}_u \\ \Delta \mathbf{f}_\alpha \end{bmatrix} \cdot \begin{bmatrix} \delta \mathbf{u}_P^\Delta \\ \delta \boldsymbol{\alpha}_P^\Delta \end{bmatrix} = \begin{bmatrix} \mathbf{f}_{u,u_P^\Delta} & \mathbf{f}_{u,\alpha_P^\Delta} \\ \mathbf{f}_{\alpha,u_P^\Delta} & \mathbf{f}_{\alpha,\alpha_P^\Delta} \end{bmatrix} \begin{bmatrix} \Delta \mathbf{u}_P^\Delta \\ \Delta \boldsymbol{\alpha}_P^\Delta \end{bmatrix} \cdot \begin{bmatrix} \delta \mathbf{u}_P^\Delta \\ \delta \boldsymbol{\alpha}_P^\Delta \end{bmatrix}. \tag{4.42}$$

In order to avoid cumbersome algebraic work, necessary to evaluate partial derivatives present in equation (4.42), one can employ automatic differentiation tools. In this work, a hybrid symbolic-numerical approach was used, where Mathematica®

was employed together with the automatic code generator AceGen®. The resulting codes were incorporated in GIRAFFE platform [36].

4.2. Rigid node set constraint

In the previous section a single-node rigid body element (also presented in [67]) was fully developed. There is a need of connecting it to the rest of the model. The proper connection point of a rigid body with others or with other flexible parts in a system may be done through many ways, including more than one connection material point in distinct positions of the rigid body. For such situations one should be able to define a rigid region constraint, including a set of nodes.

Possible uses of this kind of constraint may include connections between distinct rigid bodies, between rigid bodies and joints or between rigid bodies and a set of nodes in a deformable mesh². The constraint presented in this section was developed in [67] and it works like a multipoint constraint, i.e., it is a feature intended to provide a link between the degrees of freedom of one or more nodes to the degrees of freedom of a “pilot node”. A rigid connection, including translational and rotational degrees of freedom, is ensured. Therefore, this rigid constraint is also compatible with structural elements, e.g.: beams and shells. We called this a “rigid node set”.

Let us define a rigid region B in the Euclidean three-dimensional space, as depicted in Figure 4.4(a). A set of N material points $P_1, P_2, \dots, P_k, \dots, P_N$ are arbitrarily chosen. Another arbitrary choice is the material point named “pilot point” (node): P_p . We are interested in mapping the movement of all these points in space, for a general rigid body deformation. Each material point can be associated with a position vector, such that $\mathbf{x}_1, \mathbf{x}_2, \dots, \mathbf{x}_k, \dots, \mathbf{x}_N$ refers to points $P_1, P_2, \dots, P_k, \dots, P_N$ and \mathbf{x}_p to P_p . Such positions may change during the rigid region movement.

At reference configuration, the positions of the material points are, then, given by $\mathbf{x}_1^r, \mathbf{x}_2^r, \dots, \mathbf{x}_k^r, \dots, \mathbf{x}_N^r$ and \mathbf{x}_p^r . At the next configuration, they are described by $\mathbf{x}_1^i, \mathbf{x}_2^i, \dots, \mathbf{x}_k^i, \dots, \mathbf{x}_N^i$ and \mathbf{x}_p^i .

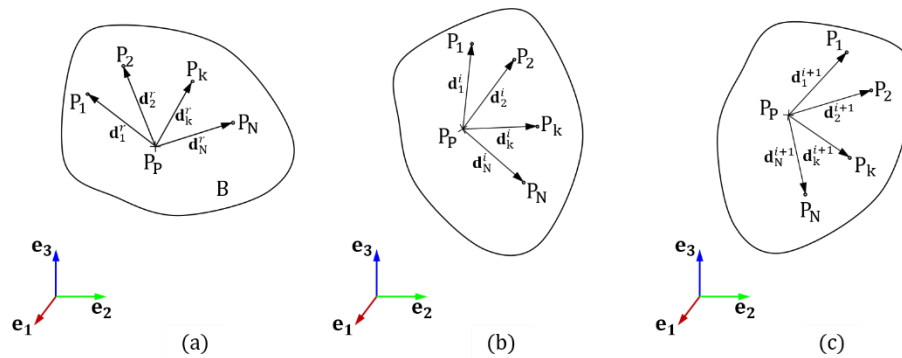
² Numerical examples of this work show some usages of this kind of constraint in practical modelling situations.

One can define a set of N distance vectors between P_k and P_p , such that:

$$\mathbf{d}_k^r = \mathbf{x}_k^r - \mathbf{x}_p^r \text{ and}$$

$$\mathbf{d}_k^i = \mathbf{x}_k^i - \mathbf{x}_p^i \quad \text{for } k = 1, \dots, N. \quad (4.43)$$

Figure 4.4: Rigid body (a) Reference configuration “ r ” (b) Deformed configuration “ i ” (c) Deformed configuration “ $i + 1$ ”.



Source: [67]

It is imposed that the magnitude of all distance vectors remains constant during the subsequent configurations. This is a necessary condition for a set of general pairs of distinct material points within a rigid body. Then, one can write the following relation:

$$\mathbf{d}_k^i = \mathbf{Q}_k^i \mathbf{d}_k^r, \quad (4.44)$$

where \mathbf{Q}_k^i is a rotation tensor that maps a vector from the reference configuration to the configuration “ i ”.

Following the same approach as in the previous section, one may define updating quantities with an upper-right index “ Δ ”. Then, it is possible to write the mapping:

$$\mathbf{d}_k^{i+1} = \mathbf{Q}_k^\Delta \mathbf{d}_k^i, \quad (4.45)$$

which may be used to write

$$\mathbf{d}_k^{i+1} = \mathbf{Q}_k^{i+1} \mathbf{d}_k^r, \quad (4.46)$$

Such that

$$\mathbf{Q}_k^{i+1} = \mathbf{Q}_k^\Delta \mathbf{Q}_k^i. \quad (4.47)$$

Regarding the displacements, it is possible to define, for each material point, the displacement vector \mathbf{u}_k^Δ between configurations “ i ” and “ $i + 1$ ”, such that:

$$\mathbf{x}_k^{i+1} = \mathbf{x}_k^i + \mathbf{u}_k^\Delta, \quad (4.48)$$

The mechanical constraint related to the mapping of vectors represented in equations (4.44), (4.45) and (4.46) can be written by:

$$\mathbf{r}_{1k} = \mathbf{d}_k^{i+1} - \mathbf{Q}_k^\Delta \mathbf{d}_k^i = \mathbf{0}_3 \quad \text{for } k = 1, \dots, N, \quad (4.49)$$

where $\mathbf{0}_3$ is a 3-dimension null vector. These constraint equations are not enough to ensure a rigid body correct kinematics for the chosen set of material points. We still have to impose that all of them must present the same rotation³. Taking the pilot point as a reference, one may state a second constraint equation, which must be obeyed:

³ This is essential, particularly when dealing with connections including rotations degrees of freedom. In this context, one should understand the rigid region constraint as a combination of two constraints: in displacement and rotation fields, as developed here. Particularly, for usage of rigid body element together with beam/shell nodes, this is very important.

$$\mathbf{r}_{2k} = \boldsymbol{\alpha}_k^\Delta - \boldsymbol{\alpha}_P^\Delta = \mathbf{0}_3 \quad \text{for } k = 1, \dots, N. \quad (4.50)$$

Then, one may rewrite (4.49) already imposing that $\mathbf{Q}_k^\Delta = \mathbf{Q}_P^\Delta$, for $k = 1, \dots, N$:

$$\mathbf{r}_{1k} = \mathbf{d}_k^{i+1} - \mathbf{Q}_P^\Delta \mathbf{d}_k^i = \mathbf{0}_3 \quad \text{for } k = 1, \dots, N. \quad (4.51)$$

In order to enforce both constraint equations (4.50) and (4.51) in a mechanical model (e.g.: a nonlinear finite element model), one may define an extra potential W_c contribution to the model, given by:

$$W_c = \sum_{k=1}^N (\boldsymbol{\lambda}_{1k} \cdot \mathbf{r}_{1k} + \boldsymbol{\lambda}_{2k} \cdot \mathbf{r}_{2k}), \quad (4.52)$$

where $\boldsymbol{\lambda}_{1k}$ and $\boldsymbol{\lambda}_{2k}$ represent 3-dimensional Lagrange multipliers vectors, unknown, and used to enforce the constraints. The weak form contribution corresponding to W_c leads from the first variation of such potential, represented by δW_c . One can write:

$$\delta W_c = \sum_{k=1}^N (\delta \boldsymbol{\lambda}_{1k} \cdot \mathbf{r}_{1k} + \delta \boldsymbol{\lambda}_{2k} \cdot \mathbf{r}_{2k} + \boldsymbol{\lambda}_{1k} \cdot \delta \mathbf{r}_{1k} + \boldsymbol{\lambda}_{2k} \cdot \delta \mathbf{r}_{2k}). \quad (4.53)$$

When handling nonlinear models, solved by numerical methods that need usage of the weak form linearization (e.g.: Newton-Raphson method), one also needs to evaluate an expression for the linearization of (4.53), represented by $\Delta(\delta W_c)$. It is given by:

$$\Delta(\delta W_c) = \sum_{k=1}^N [\delta \boldsymbol{\lambda}_{1k} \cdot \Delta \mathbf{r}_{1k} + \delta \boldsymbol{\lambda}_{2k} \cdot \Delta \mathbf{r}_{2k} + \Delta \boldsymbol{\lambda}_{1k} \cdot \delta \mathbf{r}_{1k} + \Delta \boldsymbol{\lambda}_{2k} \cdot \delta \mathbf{r}_{2k} + \boldsymbol{\lambda}_{1k} \cdot \Delta(\delta \mathbf{r}_{1k}) + \boldsymbol{\lambda}_{2k} \cdot \Delta(\delta \mathbf{r}_{2k})]. \quad (4.54)$$

The herein presented mathematical model for the rigid region constraint is intended to be applied together with a finite element nonlinear mechanical model, by usage of the updated Lagrangian description. This leads to the usage of a time-integration (in case of dynamics) or evolution integration (in case of statics). Both cases are intent to be used with solution-steps, here generally mentioned as time-steps. For

each converged time-step, one may define a known configuration “ i ”. For the next time-step, the objective is to find the solution leading to the configuration “ $i + 1$ ”. Incremental degrees of freedom (DOFs) quantities are to be solved. Then, the model DOFs are the incremental displacements \mathbf{u}_k^Δ and incremental rotations α_k^Δ . This strategy is interesting, since for each converged configuration, the previously obtained quantities related to configuration “ i ” are treated as constant for the next time-step. Then, the evaluation of each term from (4.53) and (4.54) obeys such premise: the variation and linearization operations are done only with respect to incremental quantities.

The term $\delta \mathbf{r}_{1k}$ is given by:

$$\delta \mathbf{r}_{1k} = \delta \mathbf{u}_k^\Delta - \delta \mathbf{u}_p^\Delta - \delta(\mathbf{Q}_p^\Delta \mathbf{d}_k^i). \quad (4.55)$$

The term $\delta(\mathbf{Q}_p^\Delta \mathbf{d}_k^i)$ depends on incremental rotations of the pilot point α_p^Δ . One can write:

$$\delta(\mathbf{Q}_p^\Delta \mathbf{d}_k^i) = \Xi_p \delta \alpha_p^\Delta \times (\mathbf{Q}_p^\Delta \mathbf{d}_k^i) = -\text{skew}(\mathbf{Q}_p^\Delta \mathbf{d}_k^i) \Xi_p \delta \alpha_p^\Delta, \quad (4.56)$$

where Ξ_p is given in equation (4.28). Then, using (4.56) in (4.55) leads to

$$\delta \mathbf{r}_{1k} = \delta \mathbf{u}_k^\Delta - \delta \mathbf{u}_p^\Delta + \text{skew}(\mathbf{Q}_p^\Delta \mathbf{d}_k^i) \Xi_p \delta \alpha_p^\Delta. \quad (4.57)$$

The term $\delta \mathbf{r}_{2k}$ is given by:

$$\delta \mathbf{r}_{2k} = \delta \alpha_k^\Delta - \delta \alpha_p^\Delta. \quad (4.58)$$

Using (4.57) and (4.58), one may rewrite the weak form contribution (4.53):

$$\delta W_c = \sum_{k=1}^N \left\{ \begin{bmatrix} \delta \mathbf{u}_P^{\Delta T} & \delta \boldsymbol{\alpha}_P^{\Delta T} & \delta \mathbf{u}_k^{\Delta T} & \delta \boldsymbol{\lambda}_{1k}^T \end{bmatrix} \begin{bmatrix} -\boldsymbol{\lambda}_{1k} \\ (\boldsymbol{\lambda}_{1k}^T \text{skew}(\mathbf{Q}_P^{\Delta} \mathbf{d}_k^i) \boldsymbol{\Xi}_P)^T \\ \boldsymbol{\lambda}_{1k} \\ \mathbf{r}_{1k} \end{bmatrix} + \right. \\ \left. \begin{bmatrix} \delta \boldsymbol{\alpha}_P^{\Delta T} & \delta \boldsymbol{\alpha}_k^{\Delta T} & \delta \boldsymbol{\lambda}_{2k}^T \end{bmatrix} \begin{bmatrix} -\boldsymbol{\lambda}_{2k} \\ \boldsymbol{\lambda}_{2k} \\ \mathbf{r}_{2k} \end{bmatrix} \right\}. \quad (4.59)$$

The linearization of (4.53) may be split in two terms, such that:

$$\Delta(\delta W_c) = \Delta(\delta W_c)_1 + \Delta(\delta W_c)_2. \quad (4.60)$$

with

$$\Delta(\delta W_c)_1 = \sum_{k=1}^N \begin{bmatrix} \delta \mathbf{u}_P^{\Delta T} & \delta \boldsymbol{\alpha}_P^{\Delta T} & \delta \mathbf{u}_k^{\Delta T} & \delta \boldsymbol{\lambda}_{1k}^T \end{bmatrix} \begin{bmatrix} \mathbf{O}_3 & \mathbf{O}_3 & \mathbf{O}_3 & -\mathbf{I}_3 \\ \mathbf{O}_3 & \mathbf{B}_k & \mathbf{O}_3 & \mathbf{C}_k^T \\ \mathbf{O}_3 & \mathbf{O}_3 & \mathbf{O}_3 & +\mathbf{I}_3 \\ -\mathbf{I}_3 & \mathbf{C}_k & +\mathbf{I}_3 & \mathbf{O}_3 \end{bmatrix} \begin{bmatrix} \Delta \mathbf{u}_P^{\Delta} \\ \Delta \boldsymbol{\alpha}_P^{\Delta} \\ \Delta \mathbf{u}_k^{\Delta} \\ \Delta \boldsymbol{\lambda}_{1k} \end{bmatrix} \text{ and} \quad (4.61)$$

$$\Delta(\delta W_c)_2 = \sum_{k=1}^N \begin{bmatrix} \delta \boldsymbol{\alpha}_P^{\Delta T} & \delta \boldsymbol{\alpha}_k^{\Delta T} & \delta \boldsymbol{\lambda}_{2k}^T \end{bmatrix} \begin{bmatrix} \mathbf{O}_3 & \mathbf{O}_3 & -\mathbf{I}_3 \\ \mathbf{O}_3 & \mathbf{O}_3 & +\mathbf{I}_3 \\ -\mathbf{I}_3 & +\mathbf{I}_3 & \mathbf{O}_3 \end{bmatrix} \begin{bmatrix} \Delta \boldsymbol{\alpha}_P^{\Delta} \\ \Delta \boldsymbol{\alpha}_k^{\Delta} \\ \Delta \boldsymbol{\lambda}_{2k} \end{bmatrix}, \quad (4.62)$$

where \mathbf{O}_3 is a 3x3 null square matrix and \mathbf{I}_3 is the identity matrix of order three. The operators \mathbf{B}_k and \mathbf{C}_k are given by:

$$\mathbf{B}_k = \left[(\text{skew}(\mathbf{Q}_P^{\Delta} \mathbf{d}_k^i) \boldsymbol{\Xi}_P)^T \boldsymbol{\lambda}_{1k} \right]_{,\alpha_P^{\Delta}} = -\mathbf{Y}(\mathbf{Q}_P^{\Delta} \mathbf{d}_k^i, \boldsymbol{\alpha}_P^{\Delta}, \boldsymbol{\alpha}_P^{\Delta}; \boldsymbol{\lambda}_{1k}) \text{ and} \quad (4.63)$$

$$\mathbf{C}_k = \text{skew}(\mathbf{Q}_P^{\Delta} \mathbf{d}_k^i) \boldsymbol{\Xi}_P. \quad (4.64)$$

In the definition of \mathbf{B}_k , one has to make use of the operator $\mathbf{Y}(\mathbf{Q}_P^{\Delta} \mathbf{a}, \boldsymbol{\alpha}_P^{\Delta}, \boldsymbol{\alpha}_P^{\Delta}; \mathbf{v})$ defined for general vectors \mathbf{a} and \mathbf{v} by (see e.g.: [29] and [30], where such operators

were defined in the context of the master-surface to master-surface contact formulation, where the same kind of derivation is necessary):

$$\mathbf{Y}(\mathbf{Q}_P^\Delta \mathbf{a}, \alpha_P^\Delta, \alpha_P^\Delta; \mathbf{v}) := [\hat{\mathbf{F}}(\mathbf{A}_P \mathbf{v}) + \mathbf{\Xi}_P^T \mathbf{V} \mathbf{A}_P \mathbf{\Xi}_P]. \quad (4.65)$$

with $\mathbf{V} = \text{skew}(\mathbf{v})$ and $\mathbf{A}_P = \text{skew}(\mathbf{Q}_P^\Delta \mathbf{a})$.

$\hat{\mathbf{F}}$ is an operator that can be applied to a generic vector $\mathbf{v}_P(\alpha_P^\Delta)$. It is given by:

$$\hat{\mathbf{F}}(\mathbf{v}_P) = -\frac{1}{2} \left(\frac{4}{4 + \alpha_P^\Delta \cdot \alpha_P^\Delta} \right) [(\mathbf{\Xi}_P^T \mathbf{v}_P) \otimes \alpha_P^\Delta - \text{skew}(\mathbf{v}_P)]. \quad (4.66)$$

Note that the expressions (4.59)-(4.62) are ready and directly implementable in a nonlinear finite element code. If one takes the column-vectors from (4.59), they will play the role of the residual contribution to the Newton-Raphson Method and, the square matrices from (4.61) and (4.62) will play the role of the tangent stiffness contributions, due to the rigid body constraint. Such usage ensures a quadratic convergence in the solution vicinity of the nonlinear model.

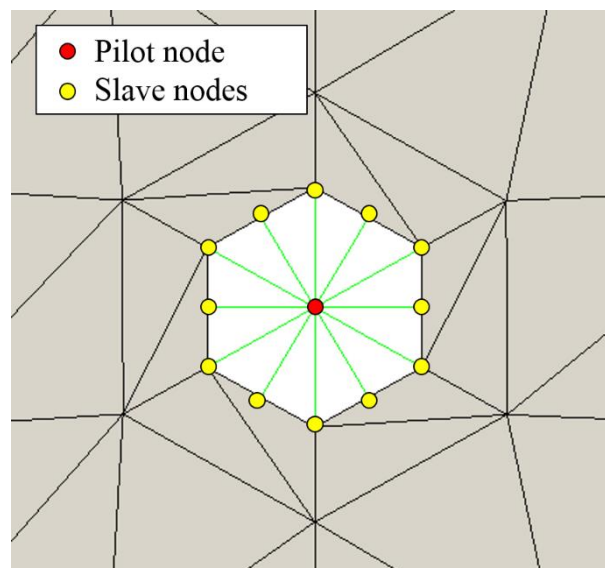
Remark 1

The rigid node set constraint here presented represents an enforcement in displacements and rotations DOFs. Naturally, such imposition will lead to a constraint also in velocities/accelerations fields, when time-integrating the system of differential-algebraic equations (DAE). One should care, however, when imposing an initial condition to the pilot node. This leads to establishing a velocity field for all nodes attached to it by the rigid node set, both for situations of initial linear/angular velocities. Then, one needs to establish a pre-processing phase of initial conditions, in order to ensure a linear/angular velocity field compatible to the rigid node set constraint, to be imposed as initial condition.

Remark 2

It is important to emphasize that attaching a rigid body element to the pilot node of a rigid node set is optional, i.e., the rigid node set can consider inertial effects of a rigid body, or not. Therefore, rigid node set constraints can be used as simple connecting features or points for applying loads. In Figure 4.5, a typical usage for a rigid node set constraint, without inertial contributions, is depicted. In such configuration, a central pilot node is rigidly connected to the border nodes of a hole, in a shell mesh. This type of constraint is popularly called “spider”, and it can be used, for example, as a loading point (by applying a concentrated load in the pilot node) or, as an idealization for a bolted connection (connecting the pilot node to a beam element and then, this beam element to another mesh).

Figure 4.5: Rigid node set constraint typical usage (“spider”).



Source: [67]

4.3. External field loading on the rigid body element

To develop the contribution of external field loads to the rigid body we refer to Figure 4.3 once more. Although it is quite simple to include the effects of external loading in finite element formulations, if a point other than the centre of mass is chosen as a pilot point in a rigid body, the equivalent force-couple system has to be considered.

Vector \mathbf{b}^{i+1} in Figure 4.3 gives the position of the centre of mass, relative to the pilot point, in the current configuration. This vector can be directly obtained from reference configuration by:

$$\mathbf{b}^{i+1} = \mathbf{Q}_k^{i+1} \mathbf{b}^r \quad (4.67)$$

Assuming the body has a total mass m and is subjected to a gravitational field \mathbf{g} , the equivalent couple is given by:

$$\mathbf{m}^{i+1} = \mathbf{b}^{i+1} \times m\mathbf{g} = \mathbf{B}^{i+1}m\mathbf{g} \quad (4.68)$$

where $\mathbf{B}^{i+1} = \text{skew}(\mathbf{b}^{i+1})$ (see Appendix A).

If we write the power of external forces and moments as:

$$\dot{W}_{\text{field}} = m\mathbf{g} \cdot \dot{\mathbf{u}} + \mathbf{m}^{i+1} \cdot \boldsymbol{\Xi}_P \dot{\boldsymbol{\alpha}} = m\mathbf{g} \cdot \dot{\mathbf{u}} + \boldsymbol{\Xi}_P^T \mathbf{m}^{i+1} \cdot \dot{\boldsymbol{\alpha}}, \quad (4.69)$$

we can immediately obtain the weak form contribution due to of external field loads applied to the rigid body element:

$$\delta W_{\text{field}} = m\mathbf{g} \cdot \delta \mathbf{u}_P^\Delta + \boldsymbol{\Xi}_P^T \mathbf{m}^{i+1} \cdot \delta \boldsymbol{\alpha}_P^\Delta = m\mathbf{g} \cdot \delta \mathbf{u}_P^\Delta + \boldsymbol{\Xi}_P^T (\mathbf{B}^{i+1} m\mathbf{g}) \cdot \delta \boldsymbol{\alpha}_P^\Delta \quad (4.70)$$

In a more compact notation:

$$\delta W_{\text{field}} = \mathbf{f}_{fu} \cdot \delta \mathbf{u}_P^\Delta + \mathbf{f}_{f\alpha} \cdot \delta \boldsymbol{\alpha}_P^\Delta = \begin{bmatrix} \mathbf{f}_{fu} \\ \mathbf{f}_{f\alpha} \end{bmatrix} \cdot \begin{bmatrix} \delta \mathbf{u}_P^\Delta \\ \delta \boldsymbol{\alpha}_P^\Delta \end{bmatrix}, \quad (4.71)$$

With

$$\mathbf{f}_{fu} = m\mathbf{g} \text{ and}$$

$$\mathbf{f}_{f\alpha} = \mathbf{\Xi}_p^T(\mathbf{B}^{i+1}m\mathbf{g}). \quad (4.72)$$

Consistent linearization of the weak form is performed, as before:

$$\Delta(\delta W_{\text{field}}) = \begin{bmatrix} \Delta \mathbf{f}_{fu} \\ \Delta \mathbf{f}_{f\alpha} \end{bmatrix} \cdot \begin{bmatrix} \delta \mathbf{u}_p^\Delta \\ \delta \boldsymbol{\alpha}_p^\Delta \end{bmatrix} = \begin{bmatrix} \mathbf{f}_{fu, \mathbf{u}_p^\Delta} & \mathbf{f}_{fu, \boldsymbol{\alpha}_p^\Delta} \\ \mathbf{f}_{f\alpha, \mathbf{u}_p^\Delta} & \mathbf{f}_{f\alpha, \boldsymbol{\alpha}_p^\Delta} \end{bmatrix} \begin{bmatrix} \Delta \mathbf{u}_p^\Delta \\ \Delta \boldsymbol{\alpha}_p^\Delta \end{bmatrix} \cdot \begin{bmatrix} \delta \mathbf{u}_p^\Delta \\ \delta \boldsymbol{\alpha}_p^\Delta \end{bmatrix}. \quad (4.73)$$

The terms $\mathbf{f}_{fu, \mathbf{u}_p^\Delta}$, $\mathbf{f}_{fu, \boldsymbol{\alpha}_p^\Delta}$ and $\mathbf{f}_{f\alpha, \mathbf{u}_p^\Delta}$ are null. However, a non-null contribution appears in $\mathbf{f}_{f\alpha, \boldsymbol{\alpha}_p^\Delta}$ due to its dependency on rotations. This term is non-null in our formulation due to generality of the pole choice. If the centre of mass is the pole choice, \mathbf{b}^{i+1} will be null and the consistent linearization contribution due to this loading term will be null.

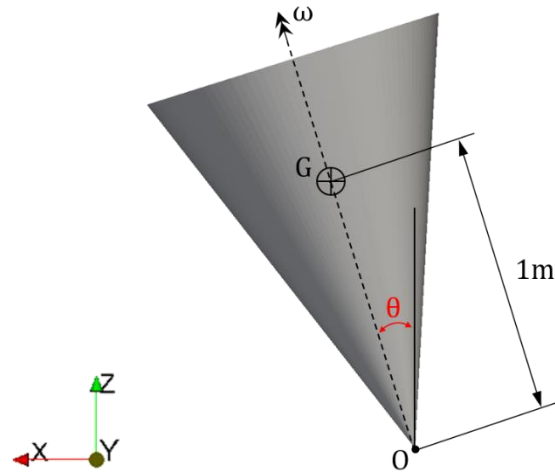
4.4. Numerical Examples

All examples in this work were performed using fully nonlinear transient dynamic analyses in GIRAFFE platform [36]. Newmark method is employed for time integration, with parameters $\beta = 0.3$ and $\gamma = 0.5$ for all the cases. Specific details of each simulation are provided as long as they are presented.

Example 4.1: Spinning top

In this example, we present a classical case from rigid-body mechanics, taken from [70]. A spinning top is modelled using the rigid body formulation developed in this work. With this model we intend to demonstrate physical coherence of our results. Moreover, we explore the possibility of choosing a node not located at the centre of mass as the rigid body (pilot node).

Figure 4.6: Example 4.1 - Spinning top.



Source: [67]

Figure 4.6 illustrates the model. The following data was considered:

Unit system: N, m, kg, s,

Gravitational field, $\mathbf{g} = [0 \ 0 \ -10]^T \text{ m/s}^2$,

Initial angle, $\theta = 17.45^\circ$,

Total mass, $m = 2 \text{ kg}$,

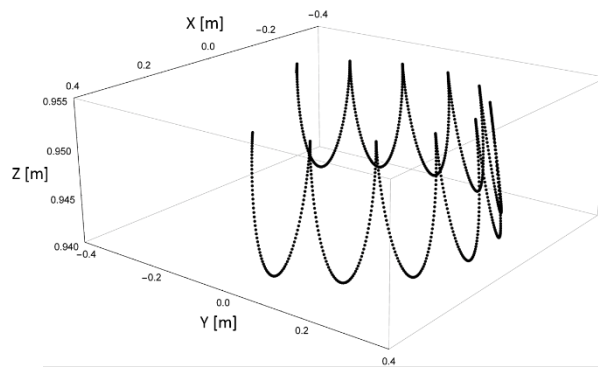
Initial angular velocity, $\boldsymbol{\omega} = [50 \sin \theta \ 0 \ 50 \cos \theta]^T \text{ rad/s}$ and

Inertia tensor, $\mathbf{J} = \begin{bmatrix} 5 & 0 & 0 \\ 0 & 5 & 0 \\ 0 & 0 & 1 \end{bmatrix} \text{ kg.m}^2$.

Note: \mathbf{J} is provided with respect to local barycentric axes, with local z axis aligned with $(G - O)$ direction and local y axis aligned with global Y axis.

A total time of 10 s was simulated and a fixed time step $\Delta_t = 0.001$ s was adopted. The rigid body element associated node is located at the lower vertex of the spinning top, i.e., at material point 0. This node has its translational degrees of freedom constrained, which means that the body is free to rotate in any direction around 0, however, translation of this point is not allowed. In Figure 4.7, the trajectory of the centre of mass is plotted, presenting results similar to ones shown in [70].

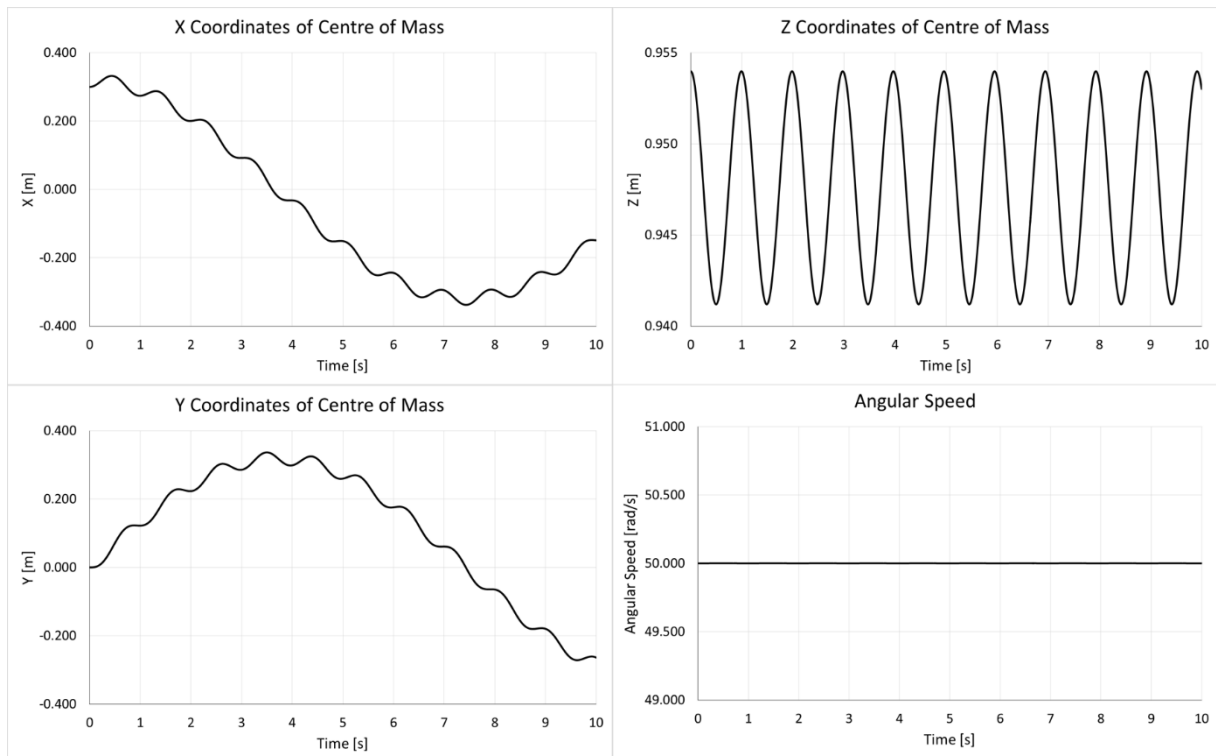
Figure 4.7: Example 4.1 - Trajectory of the centre of mass.



Source: [67]

For better visualization, time evolution of centre of mass position is shown in components in Figure 4.8. In addition, the magnitude of angular speed is also shown. In Figure 4.9, mechanical energy and the magnitude of the angular momentum are shown (measured at the centre of mass).

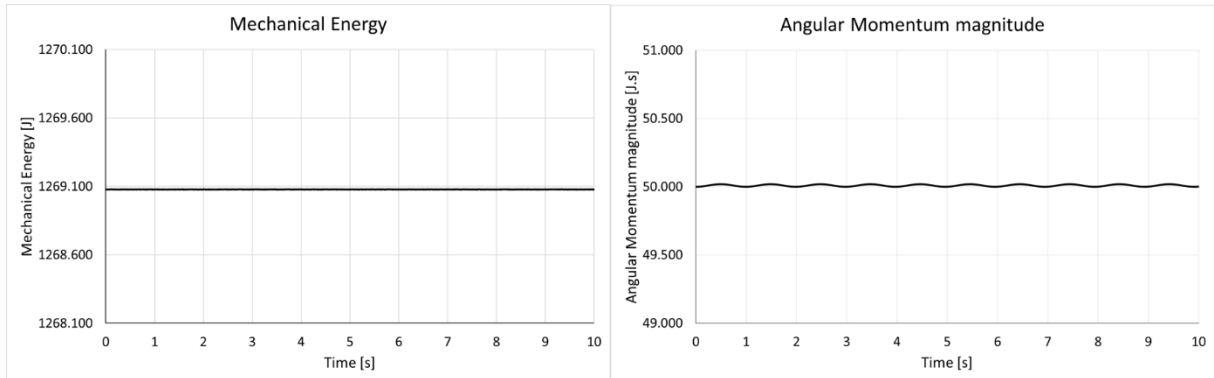
Figure 4.8: Example 4.1 - Kinematic information.



Source: [67]

As can be observed in Figure 4.8, angular speed remains constant during the whole analysis. In Figure 4.9, one may observe the mechanical energy time-evolution, presenting the same result reported in reference [70]. We show also in Figure 4.9 the magnitude of the angular momentum, evaluated taking the point G as the pole. One may note an oscillating behaviour in such quantity, along time, such as occurring in Z coordinate of the barycentre.

Figure 4.9: Example 4.1 - Mechanical energy and angular momentum magnitude.



Source: [67]

Example 4.2: Double pendulum

In this simple example, we combine two identical rigid bodies to form a double pendulum. The connection between the two elements is done by a hinge joint element (see [18]). Initial position, as well as additional details of the model are illustrated in Figure 4.10. The following data was considered:

Unit system: N, m, kg, s,

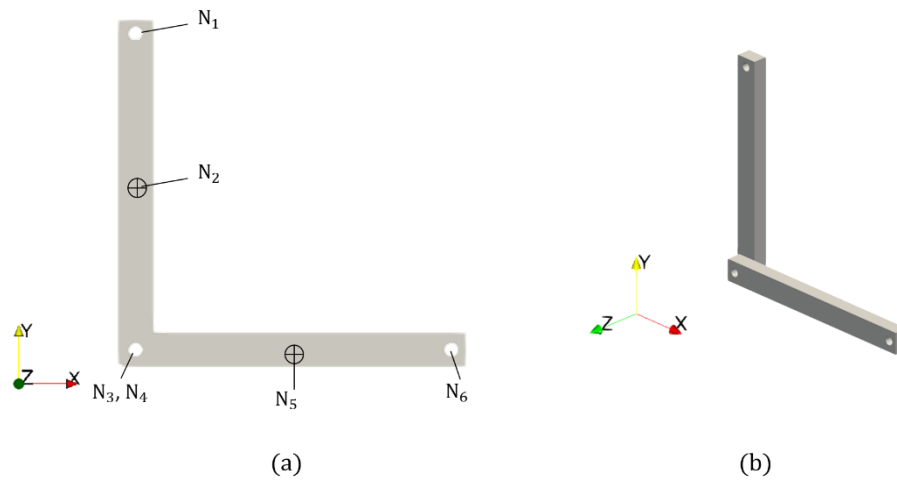
Gravitational field, $\mathbf{g} = [0 \quad -9.81 \quad 0]^T \text{ m/s}^2$,

Mass (of each body), $m = 1.377 \text{ kg}$,

Inertia tensor (of each body), $\mathbf{J} = \begin{bmatrix} 0.0100 & 0 & 0 \\ 0 & 0.0002 & 0 \\ 0 & 0 & 0.0100 \end{bmatrix} \text{ kg.m}^2$.

Note: \mathbf{J} is provided with respect to local barycentric axes aligned with the global axes. For body 2 (horizontal body), \mathbf{J} has to be properly rotated.

Figure 4.10: Example 4.2 - (a) Front view of the double pendulum. (b) Isometric view of the double pendulum.



Source: [67]

In Table 4.1, the global coordinates of the double pendulum points are provided. Point N_1 is fixed in all degrees of freedom, except from rotation about global Z axis. This point is rigidly connected to points N_2 and N_3 . The first rigid body (body 1) is defined at N_2 , which coincides with its centre of mass. A hinge joint element, free to rotate about global Z axis is defined between N_3 and N_4 . Point N_4 is rigidly connected to points N_5 and N_6 and the second rigid body (body 2) is defined at N_5 , which coincides with its centre of mass. A total time of 5 s was simulated and a fixed time step, $\Delta_t = 0.001$ s was adopted. Since here the context is of a finite element model, all mentioned points are defined as nodes in our solver.

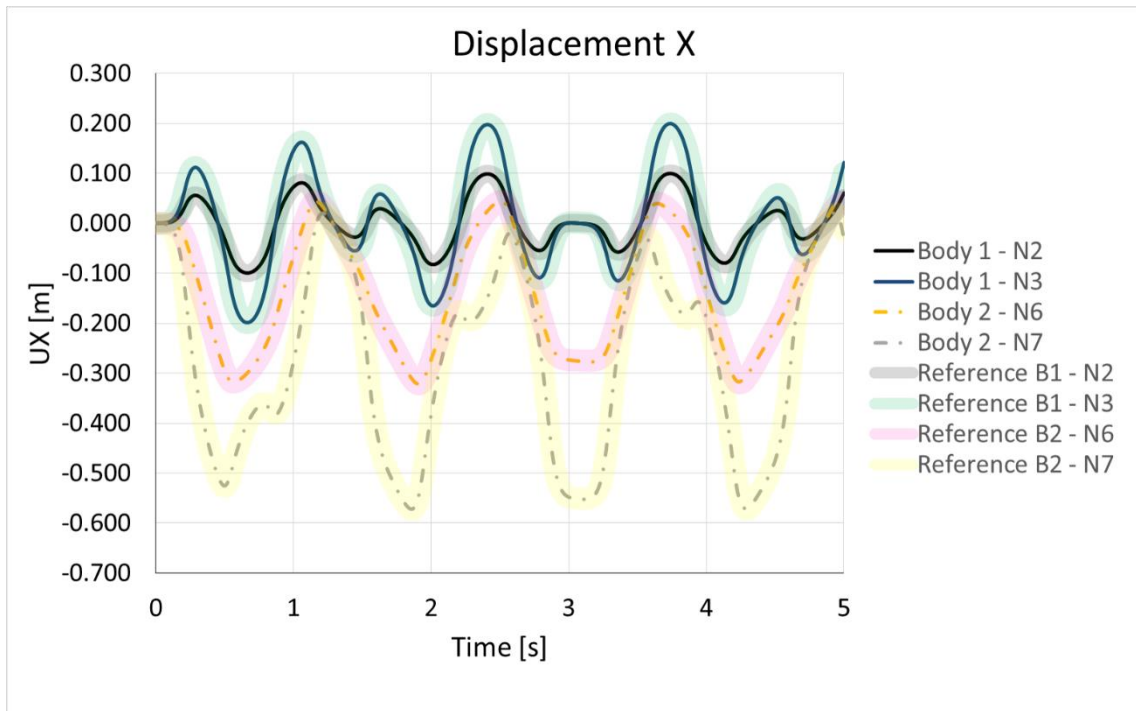
Table 4.1: Example 4.2 - Global coordinates of points.

Point	X [m]	Y [m]	Z [m]
N_1	0.000	0.000	0.000
N_2	0.000	-0.138	0.000
N_3	0.000	-0.276	0.000
N_4	0.000	-0.276	0.000
N_5	0.138	-0.276	0.020
N_6	0.276	-0.276	0.020

Source: [67]

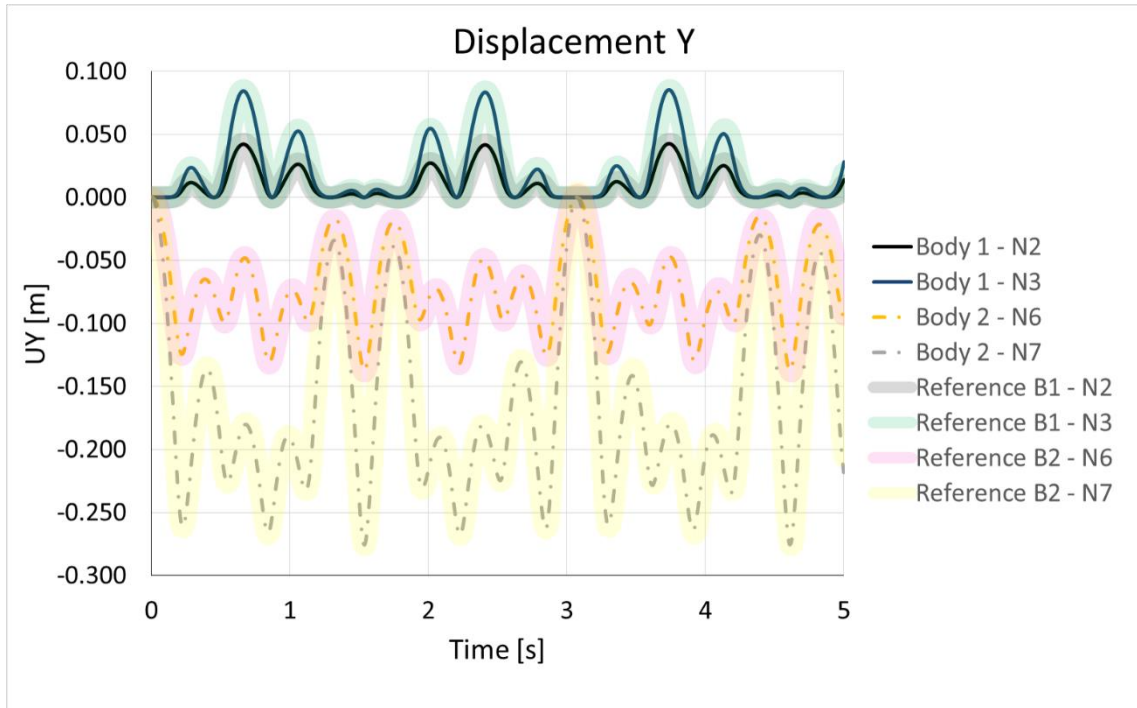
Figure 4.11 and Figure 4.12 presents the global displacements in X and Y directions. Results are shown for body 1 and body 2 at points N_2 , N_3 and N_5 , N_6 , respectively. In Figure 4.13, angular speed about global Z axis is plotted for each body.

Figure 4.11: Example 4.2 - Global X displacements.



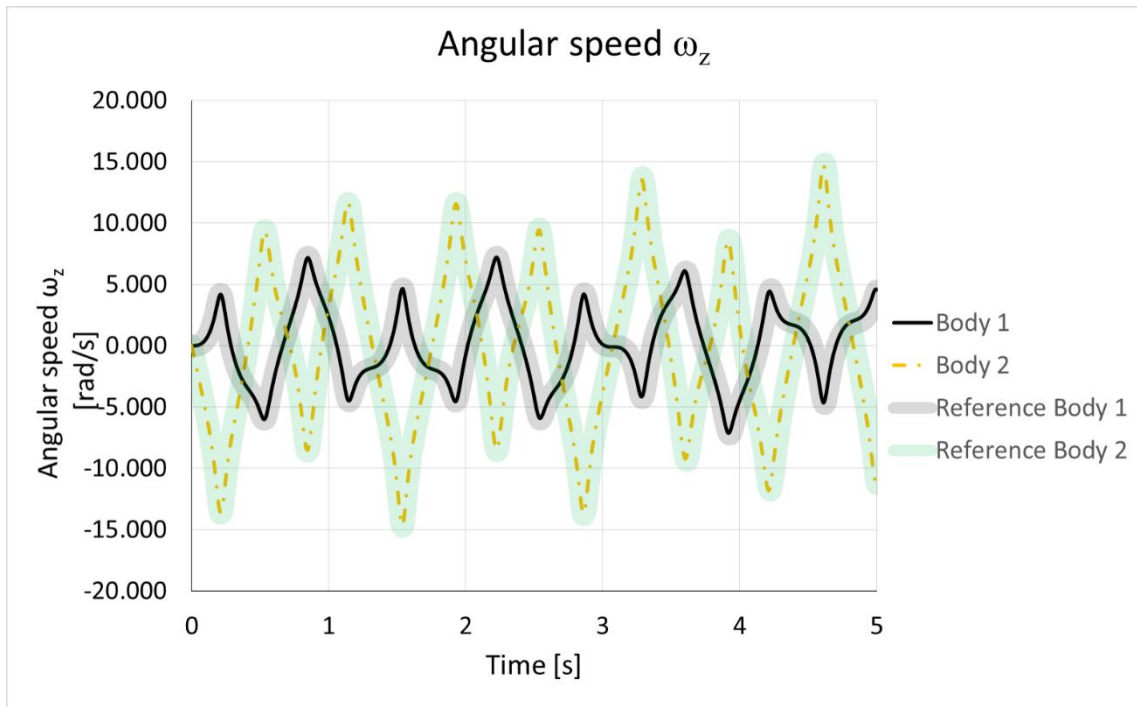
Source: Author

Figure 4.12: Example 4.2 - Global Y displacements.



Source: Author

Figure 4.13: Example 4.2 - Angular speed around global Z axis.



Source: Author

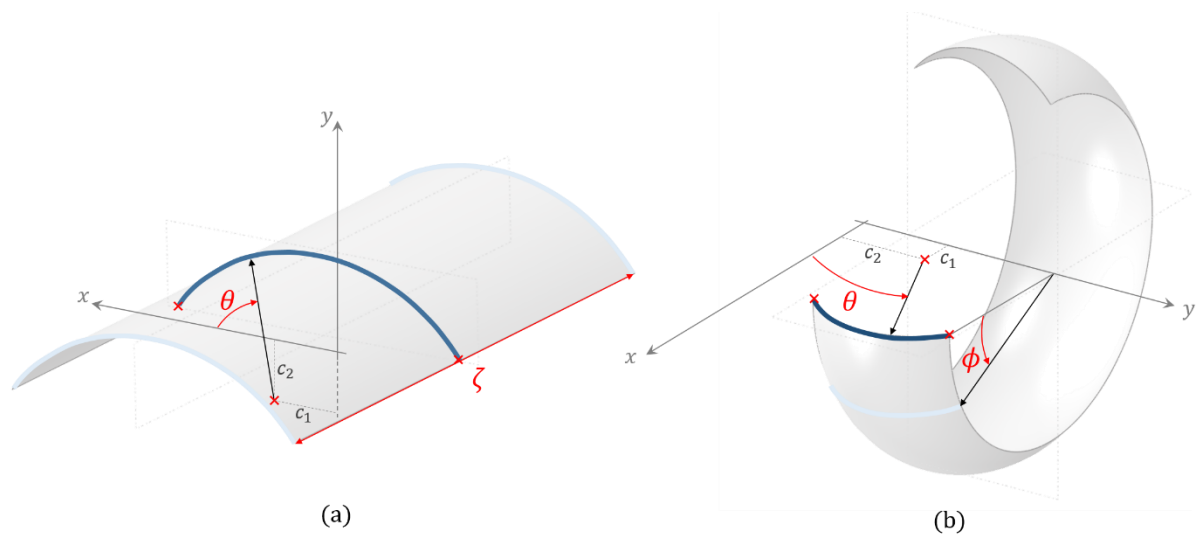
The results shown in Figure 4.11, Figure 4.12 and Figure 4.13 are in perfect agreement with the reference model solved using the commercial package MotionSolve®, available within the Altair HyperWorks suite (results of the reference model also shown in the same figures).

5. PARAMETERIZATION OF SURFACES

The master-master contact formulation, as presented in [29] and [30], was applied to the context of beam-to-beam contact only. In present work, new parameterized surfaces are presented and implemented in GIRAFFE platform [36], in order to increase the range of applicability of such formulation.

Extrusion and revolution rigid/flexible bodies are going to be addressed. Both are proposed, using for that, first, a planar parameterization of a curve composed of arcs, which are later extruded or revolved, generating the desired surfaces for establishing contact. The aim is to develop a new contact pair that allows the interaction between “extruded arcs” and “revolved arcs”. Such kind of surfaces are shown in Figure 5.1.

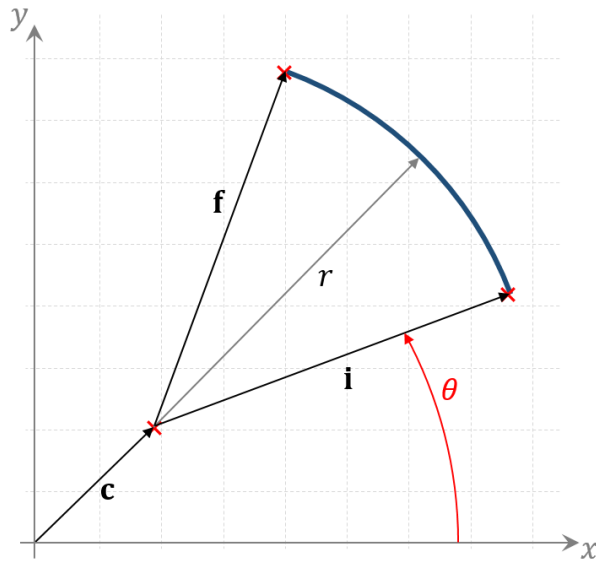
Figure 5.1: (a) An example of an extruded arc. (b) An example of a revolved arc.



Source: [67]

Both surfaces are based on the same main feature: an arc defined in a local coordinate system, as shown in Figure 5.2.

Figure 5.2: A 2D arc defined in a local coordinate system.

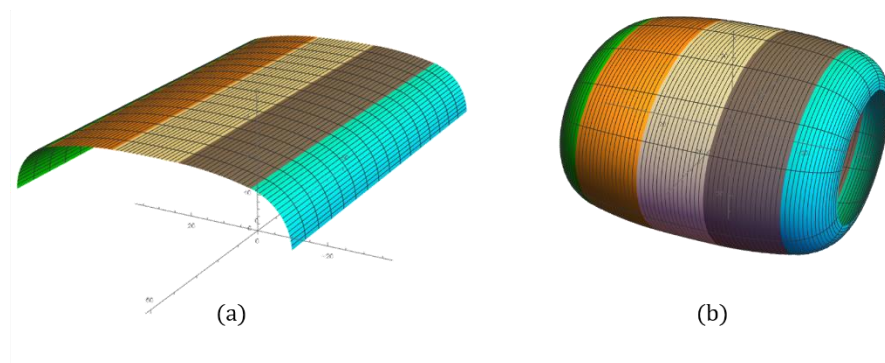


Source: [67]

In the local coordinate system, the centre of curvature, c , an initial and a final point, i and f , and the radius of the arc, r , are defined. With these quantities, the convective coordinate θ can be obtained.

The parameterizations here presented are ready to be used with the master-surface to master-surface contact formulation. In practical usage, several arcs can be combined to form a more elaborated surface. For example, in Figure 5.3(a), five extruded arcs were used to compound a profile similar to the top of a railway rail profile. It is possible, as well, to represent a more complex revolving surface, such as presented in Figure 5.3(b), including varying revolving radii, according to parameters x_{factor} and z_{factor} .

Figure 5.3: (a) A profile composed by a set of extruded arcs. (b) A revolved surface composed by a set of arcs.



Source: [67]

5.1. Extruded rigid or flexible contact surface

The extruded arc, shown in Figure 5.1(a), is designed to be attached to two nodes, located at extreme points of the surface. These nodes can be constrained to compose a rigid surface or they can be the end nodes of a beam finite element, for example, and in that case, a flexible surface is generated.

For the “extruded arc”, a very simple vector function \mathbf{f}_A , describing the arc in the 2D plane, can be established, then, this function can be interpolated between the two nodes to generate an extruded surface, as follows:

$$\mathbf{f}_A = \begin{bmatrix} r \cos \theta + c_1 \\ r \sin \theta + c_2 \\ 0 \end{bmatrix}. \quad (5.1)$$

Here, linear interpolation functions were assumed, following [29]:

$$h_1 = \frac{1}{2}(1 - \zeta) \text{ and}$$

$$h_2 = \frac{1}{2}(1 + \zeta), \quad (5.2)$$

with $-1 \leq \zeta \leq +1$ being the convective coordinate along the extrusion direction (see Figure 5.1(a)). Using Equations (5.1) and (5.2) the surface parameterization can be written:

$$\Gamma_A(\zeta, \theta) = h_1(\mathbf{Q}_1 \mathbf{f}_A + \mathbf{x}_1) + h_2(\mathbf{Q}_2 \mathbf{f}_A + \mathbf{x}_2). \quad (5.3)$$

In expression (5.3), \mathbf{Q}_1 and \mathbf{Q}_2 are rotation tensors that account for the transformation between local and global coordinate systems and also the rotation experienced by the attached nodes. In addition, \mathbf{x}_1 and \mathbf{x}_2 are the updated (current) node positions.

Note that Figure 5.1(a) shows that the positive direction of the convective coordinate ζ may be interpreted differently, according to the chosen nodes \mathbf{x}_1 and \mathbf{x}_2 and rotation tensors \mathbf{Q}_1 and \mathbf{Q}_2 .

5.2. Revolved rigid contact surface

The revolved arc, shown in Figure 5.1(b), is attached to a single node, in a way that a rigid surface is always generated. The node of a revolved arc can be a simple free node, or it can be a rigid body element (one-node element) with mass and inertia properties.

For the revolved arc, a procedure similar to that of extruded arc is employed. However, it is even simpler since it is attached to a single node.

A vector function \mathbf{f}_B can be defined:

$$\mathbf{f}_B = \begin{bmatrix} (r \cos \theta + c_1)(x_{\text{factor}} \cos \phi) \\ r \sin \theta + c_2 \\ -((r \cos \theta + c_1)(z_{\text{factor}} \sin \phi)) \end{bmatrix}, \quad (5.4)$$

where x_{factor} and z_{factor} are parameters that can be used to represent ovalized geometries (varying revolving radii) and ϕ is the convective coordinate for the revolution angle (see Figure 5.1(b)).

The local y axis was chosen to be the revolution axis. Expression (5.4) can be used to parameterize the surface in the following way:

$$\Gamma_B(\phi, \theta) = \mathbf{Q}\mathbf{f}_B + \mathbf{x}. \quad (5.5)$$

Here \mathbf{Q} represents a composed rotation tensor, accounting for the transformation between local and global coordinate systems and also the rotation experienced by the attached node. In addition, \mathbf{x} is the updated (current) node position.

5.3. Numerical Examples

All examples in this dissertation were performed using fully nonlinear transient dynamic analyses in GIRAFFE platform [36]. Newmark method is employed for time integration, with parameters $\beta = 0.3$ and $\gamma = 0.5$ for all the cases. Specific details of each simulation are provided as long as they are presented.

Example 5.1: Rigid ball in contact

In *Example 5.1*, the rigid body formulation is used together with the contact formulation presented in this work. We develop the case of a rigid body, shaped like an American Football ball, in contact with a rigid floor. Figure 5.4 provides an overview of this model. A rigid body element was defined at point N_1 . This point corresponds to the centre of mass of the ball. The following data was considered:

Unit system: N, m, kg, s,

Gravitational field, $\mathbf{g} = [0 \ 0 \ -9.81]^T m/s^2$,

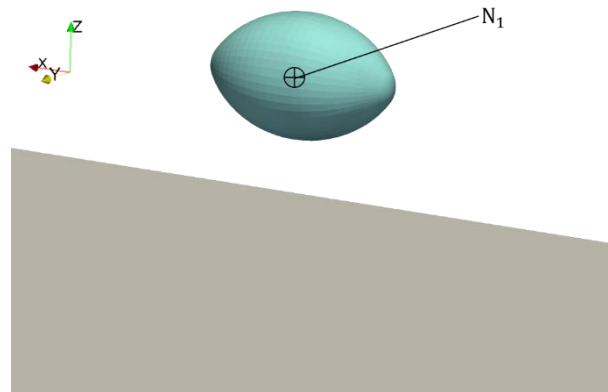
Initial angular velocity, $\boldsymbol{\omega} = [0 \ 0 \ 6.28]^T rad/s$

Mass, $m = 0.439 kg$,

Inertia tensor, $\mathbf{J} = \begin{bmatrix} 0.00224 & 0 & 0 \\ 0 & 0.00139 & 0 \\ 0 & 0 & 0.00224 \end{bmatrix} kg.m^2$.

Note: \mathbf{J} is provided with respect to local barycentric axes oriented such as those illustrated in Figure 5.5(b).

Figure 5.4: Example 5.1 - Global overview of the model.



Source: [67]

The rigid floor is represented by an arc extruded between two fixed nodes (N_{floor}^1 and N_{floor}^2). The coordinates of the nodes of this model are provided in Table 5.1.

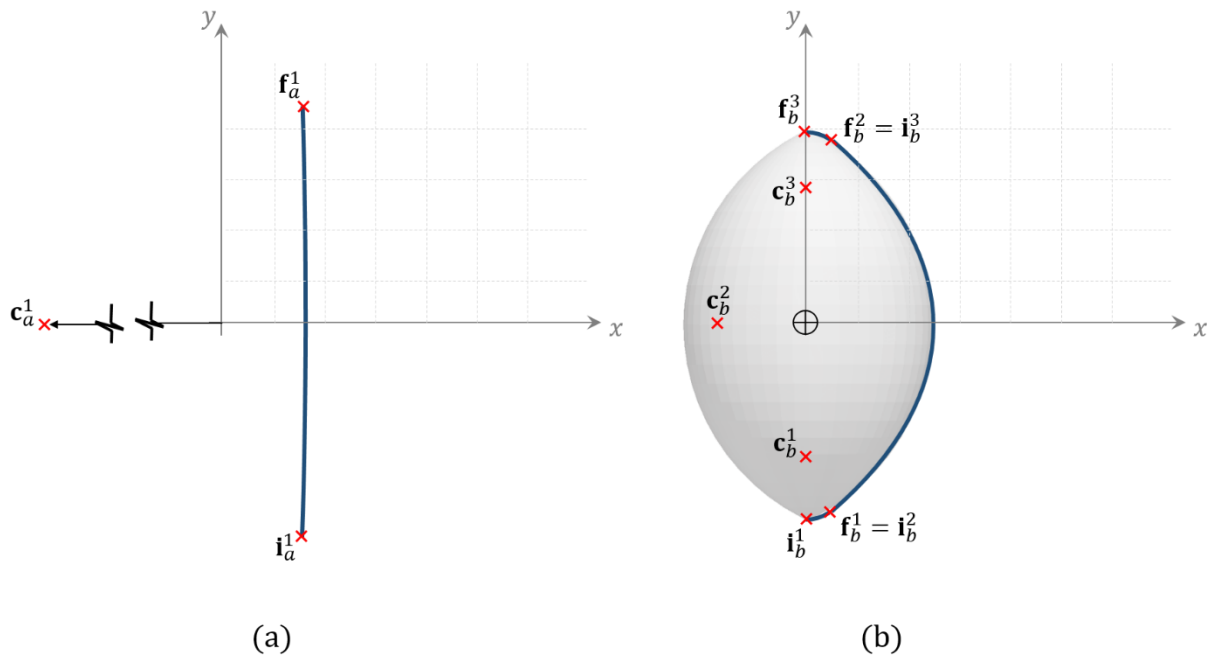
Table 5.1: Example 5.1 - Global coordinates of points.

Point	X [m]	Y [m]	Z [m]
N_1	0.0	0.0	0.4
N_{floor}^1	0.0	-1.0	0.0
N_{floor}^2	0.0	1.0	0.0

Source: [67]

In Figure 5.5, the arcs used to generate contact surfaces are presented. The same approach introduced in section 5 was used, i.e., arcs were defined in local coordinate systems and then positioned in the global model. The arcs used to represent the ball are revolved about local y axis. The single arc employed to represent the floor was chosen with a very large curvature radius, in order to represent a practical flat surface. Local coordinates of each arc illustrated in Figure 5.5 are provided in Table 5.2.

Figure 5.5: Example 5.1 - (a) Contact arc for rigid floor. (b) Contact arcs for ball.



Source: [67]

Table 5.2: Example 5.1 - Local coordinates of contact arcs.

Point	x [m]	y [m]
c_a^1	-1.000e+005	0.000
i_a^1	0.000	-1.000
f_a^1	0.000	1.000
c_b^1	0.000	-0.100
i_b^1	0.000	-0.140
f_b^1	0.024	-0.132
c_b^2	-0.075	0.000
i_b^2	0.024	-0.132
f_b^2	0.024	0.132
c_b^3	0.000	0.100
i_b^3	0.024	0.132
f_b^3	0.000	0.140

Source: [67]

After contact is established between ball and rigid floor, an impulse load is applied to the centre of mass of the ball. The force is applied in the global Y direction and its time history is presented in Table 5.3 (linear interpolation is assumed between time-values shown in the table):

Table 5.3: Example 5.1 - Force time history.

Time [s]	FY [N]
0.0	0.0
1.0	0.0
1.1	5.0
1.2	0.0
10.0	0.0

Source: [67]

Four different coefficients of friction were analysed: $\mu_1 = 0.01$, $\mu_2 = 0.1$, $\mu_3 = 0.25$ and $\mu_4 = 0.5$. Normal and tangential penalty factors were defined as $1.0e+004 \text{ N/m}$ and a normal damping, equal to 50 N.s/m , was employed at the contact interface⁴. All the analyses were performed using fixed time step, $\Delta_t = 0.0001 \text{ s}$.

In Figure 5.6, the trajectory of the centre of mass of the ball is illustrated in the XY plane, for each coefficient of friction. Figure 5.7 shows the kinetic energy and the magnitude of angular momentum for each model and Figure 5.8 illustrates the contact forces time-series. Since we are not interested in the impact event in this example, contact forces are shown starting at 1 s in Figure 5.8.

In Figure 5.6, one can notice that when $\mu = 0.01$, the ball simply slides, falling outside the contact surface (the rigid floor is a squared plate 1 m x 1 m). For higher friction coefficients, the ball remains within the floor surface, exhibiting very particular trajectories.

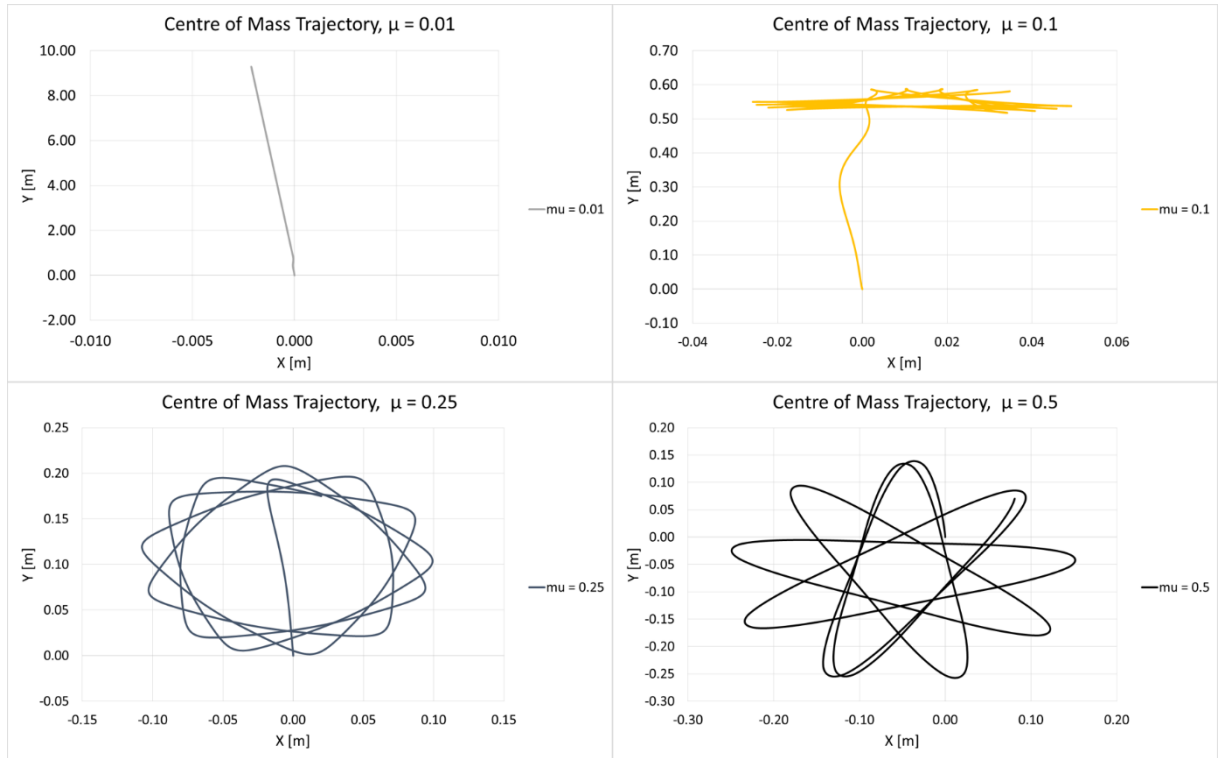
From Figure 5.7, it is possible to notice a peak in kinetic energy at the start of the analysis (due to the impact of the ball over the rigid floor). After that, due to impulsive load acting on the ball, all cases acquired kinetic energy. In cases of smaller friction coefficients, pure rolling takes longer to be achieved. For example, when $\mu = 0.1$ one may see that kinetic energy time-series achieves an oscillating long-term pattern after 2 s. For the case of $\mu = 0.25$, this was achieved prior to 2 s. The dissipation

⁴ The damping model employed is based on a standard linear dissipation with respect to relative speed of surface material points on contact interface. One may see details of application of similar models in the context of rigid balls with surfaces in [72].

of energy occurred during this initial sliding phase varies according to the choice of coefficient of friction and leads the system to distinct amplitudes and oscillation patterns, in the long term. The long-term behaviour is characterized by oscillations (see the patterns in Figure 5.6), while pure rolling is observed on contact interface.

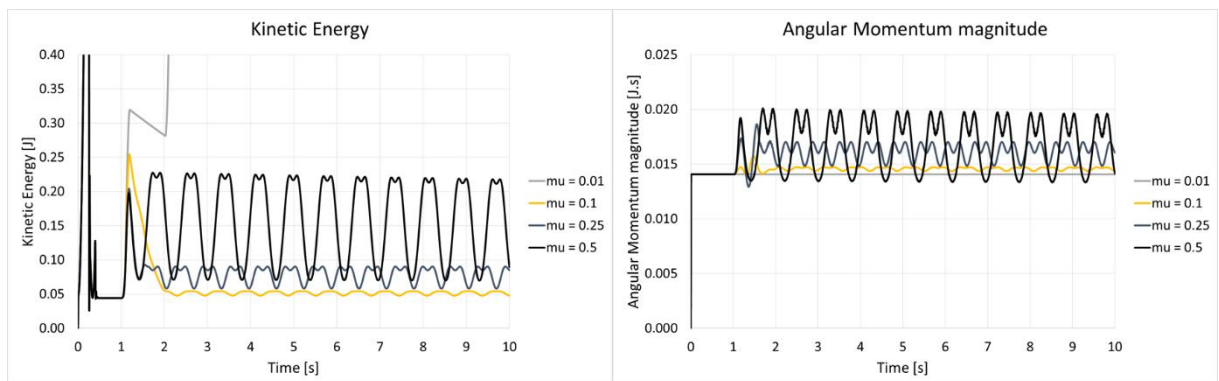
An interesting observed result was that for $\mu = 0.5$: mechanical energy was not fully conserved after the pure rolling regime was achieved (note the slight decrease in amplitudes of kinetic energy in Figure 5.7, which can be observed after each cycle along simulation). To better understand this phenomenon, it is important to mention that when $\mu = 0.5$, the ball rolls in a way that the smaller lateral arcs, which generated the ball revolving surface (see Figure 5.5(b)) get in contact with the floor. For the other models, it does not occur, such that contact takes place only in the range of the central arc that shapes the revolving surface of the ball. The singular change in curvature radius during the pure rolling of the ball on the floor surface introduces an effect similar to a local impact, which explains some dissipation of energy. This can also be seen when investigating the behaviour of friction forces, in Figure 5.8. These plots show the friction force along time, for each case, and also the maximum friction available, according to the Coulomb's law. Then, one may interpret such plots as envelopes for non-sliding conditions, if the friction experienced does not saturates the Coulomb's limit. When saturation occurs, dissipation of energy takes place. One may see that in the case when $\mu = 0.1$, the saturation limit is almost tested at each cycle, while when $\mu = 0.25$ the saturation limit is quite far from the friction actual occurrence. The case when $\mu = 0.5$ is particularly interesting since one may observe high-frequency oscillations in both saturation limit and friction occurrences, testing the Coulomb limits for very small periods of each cycle, leading to a slight energy dissipation. The high frequency oscillations occur exactly when pure rolling contact experiences the singular change in curvature radius on the surface of the ball. Numerically, when trying to enforce the contact condition, the forces start oscillating due to penalty parameters adopted for contact and should not be directly related to physical oscillations, but numerical ones.

Figure 5.6: Example 5.1 - Trajectory of the centre of mass.



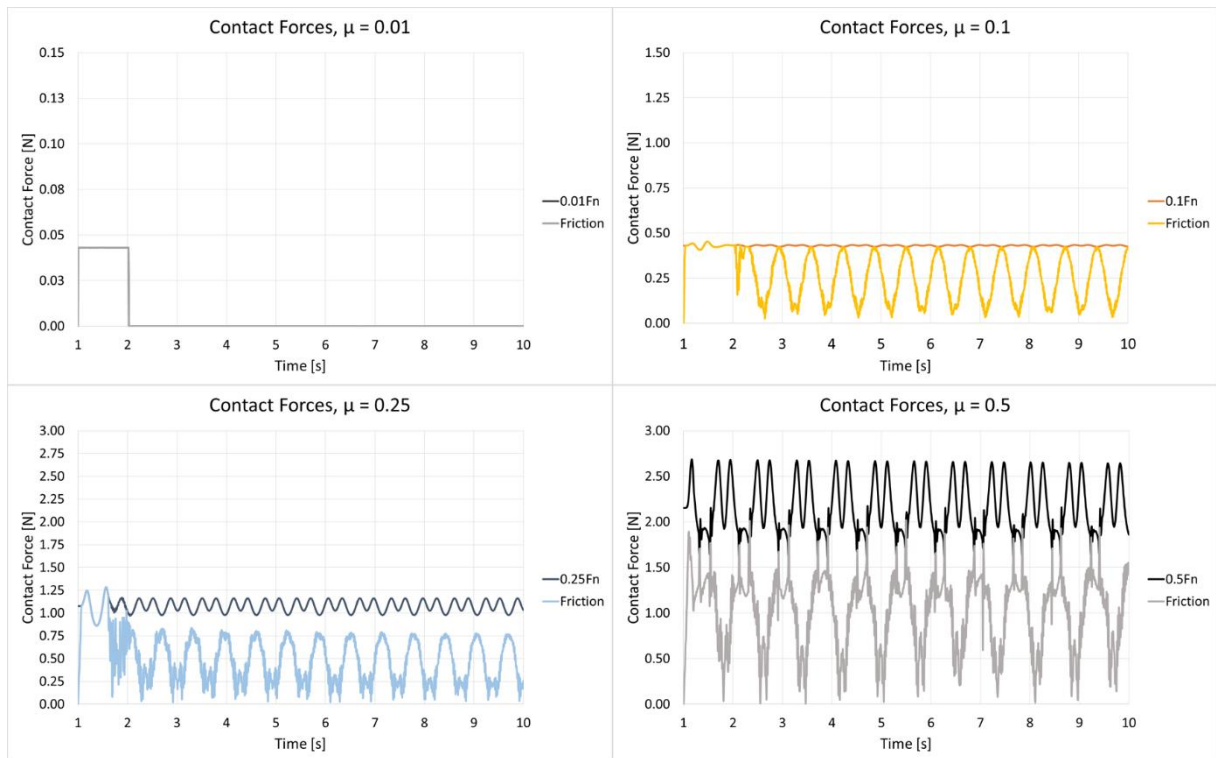
Source: [67]

Figure 5.7: Example 5.1 - Kinetic energy and angular momentum magnitude.



Source: [67]

Figure 5.8: Example 5.1 - Contact forces.



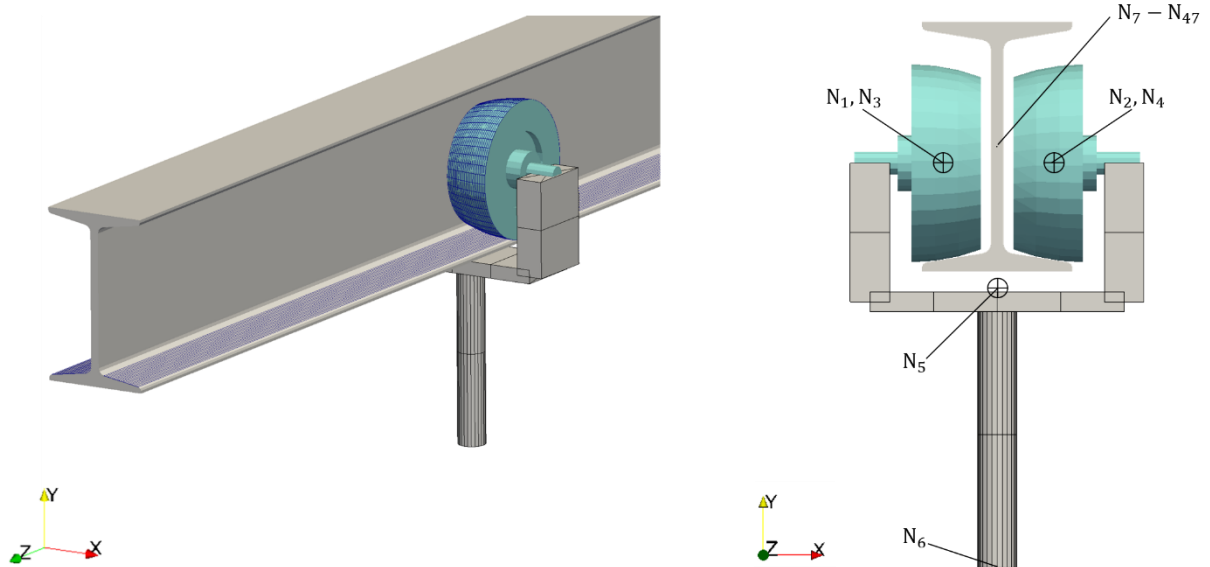
Source: [67]

Example 5.2: Overhead conveyor

In this example, beam elements, rigid bodies, joints as well as contact interactions between rigid and flexible bodies are present. We develop a simplified model of an overhead conveyor. The system consists of a main body and two wheels, all represented by rigid bodies. The guide rail is represented by second order beam elements, with I cross section (from [71]). The rolling movement of the wheels is allowed through the use of hinge joints (from [18]). We call attention for the contact interaction between the rigid wheels and the I-shaped cross section of beam elements, from author's knowledge, it represents a novel application involving frictional beam contact.

In Figure 5.9, the main features of this model are illustrated. Global coordinates of the points represented in this picture are provided in Table 5.4.

Figure 5.9: Example 5.2 - Overhead conveyor.



Source: [67]

Table 5.4: Example 5.2 - Global coordinates of points.

Point	X [mm]	Y [mm]	Z [mm]
N ₁	-26.7945	159.5163	0.0000
N ₂	26.7945	159.5163	0.0000
N ₃	-26.7945	159.5163	0.0000
N ₄	26.7945	159.5163	0.0000
N ₅	0.0000	102.609	0.0000
N ₆	0.0000	-49.4835	0.0000
N ₇	0.0000	167.9163	200.0000
N ₄₇	0.0000	167.9163	-3800.0000

Source: [67]

The main body is positioned at N₅. This corresponds to the centre of mass of the component. A rigid node set is created connecting N₅, as a pilot node, to N₃, N₄ and N₆. Hinge joints, free to rotate about the global X axis, were defined between N₃ and N₁ (left wheel) and N₄ and N₂ (right wheel).

Points N₁ and N₂ correspond to the centre of mass of the wheels. The following data was considered:

Unit system: N, mm, tonne, s,

Gravitation field was not included in this analysis.

For each wheel:

Mass, $m = 0.001968$ tonne,

$$\text{Inertia tensor, } \mathbf{J} = \begin{bmatrix} 1.354 & 0 & 0 \\ 0 & 2.263 & 0 \\ 0 & 0 & 1.354 \end{bmatrix} \text{ tonne} \cdot \text{mm}^2.$$

Note: \mathbf{J} is provided with respect to local barycentric axes oriented such as those illustrated in Figure 5.10(b).

For the main body:

Mass, $m = 0.00211$ tonne,

$$\text{Inertia tensor, } \mathbf{J} = \begin{bmatrix} 5.05 & 0 & 0 \\ 0 & 6.56 & 0 \\ 0 & 0 & 10.84 \end{bmatrix} \text{ tonne} \cdot \text{mm}^2.$$

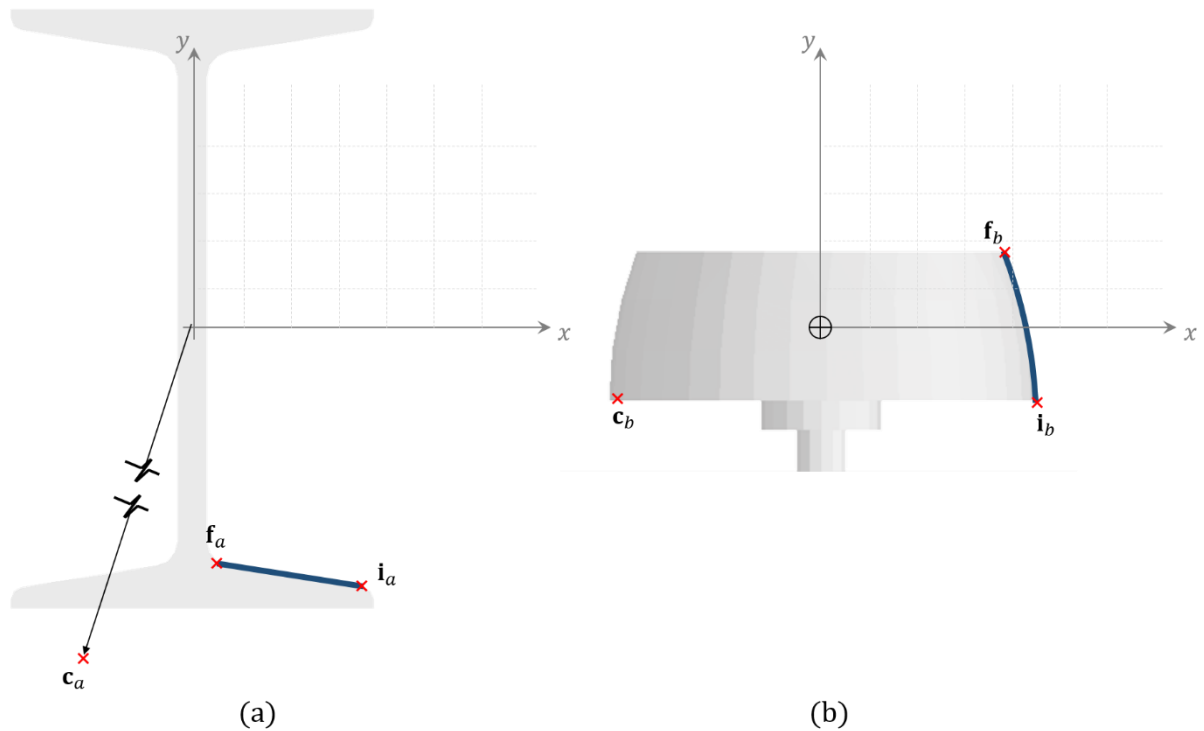
Note: \mathbf{J} is provided with respect to local barycentric axes aligned with the global axes.

In Figure 5.10, the arcs used to generate contact surfaces are presented. The same approach introduced in section 5 was used, i.e., arcs were defined in local coordinate systems and then positioned in the global model. In Figure 5.10, the arc used to represent the wheel is revolved about local y axis. The arc used to represent the I-beam webs, on the other hand, is extruded between the beam nodes. Both arcs have to be positioned in the model in such a way to represent the two wheels and the two sides of the beam. Local coordinates of each arc illustrated in Figure 5.10 are provided in Table 5.5.

Frictional contact is defined with $\mu = 0.1$. Normal and tangential penalty factors were defined as $1.0\text{e}+004$ N/mm and $1.0\text{e}+003$ N/mm, respectively. A normal

damping, equal to 50 N.s/mm , was employed in the contact interface (see [72] for details of damping model).

Figure 5.10: Example 5.2 - (a) Contact arc for I-beam. (b) Contact arc for wheel.



Source: [67]

Table 5.5: Example 5.2 - Local coordinates of contact arcs.

Point	x [mm]	y [mm]
c_a	-1641.332747439500	-10412.570484686000
i_a	35.996373000000	-58.531600000000
f_a	7.395194000000	-53.938800000000
c_b	-49.000528400995	-16.542095535700
i_b	49.9999999995448	-16.542000000000
f_b	43.6066955941508	18.458000000000

Source: [67]

Finally, the guide rail is represented by several second order beam elements defined between equally spaced nodes distributed between N_7 and N_{47} . Nodes N_7 and N_{47} have all its translational degrees of freedom and the rotation about global Z axis constrained (pinned-pinned condition). Linear elastic material ($E = 70000 \text{ MPa}$, $\nu =$

0.33, $\rho = 2.7e-009 \text{ tonne/mm}^3$) is assumed for this component and the following cross-sectional properties were adopted:

Cross sectional area, $A = 1780 \text{ mm}^2$,

Second moment of area about local x axis, $I_{xx} = 4503109.50000 \text{ mm}^4$,

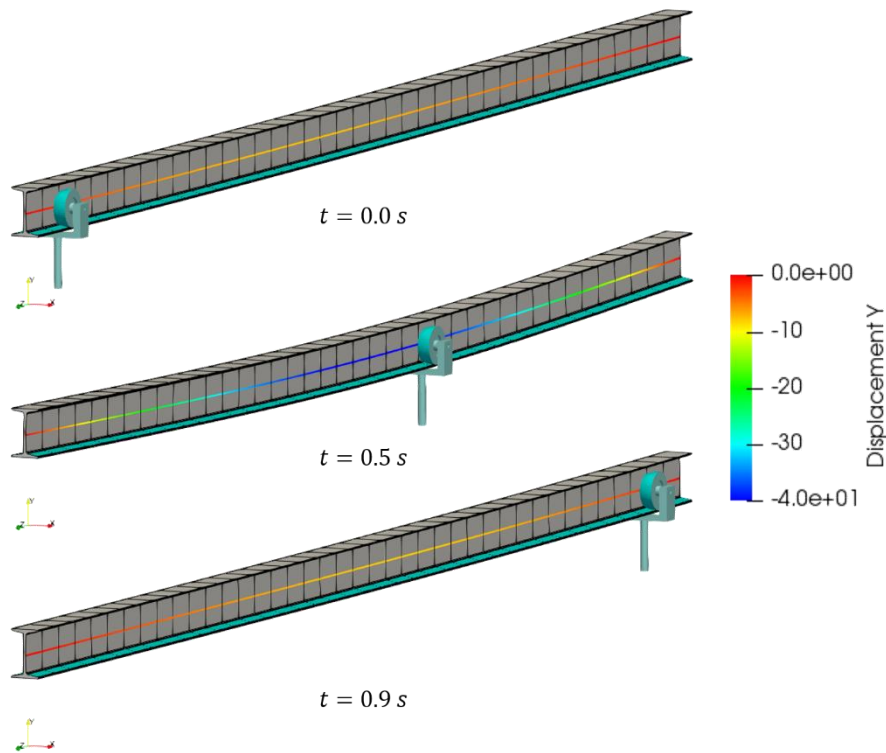
Second moment of area about local y axis, $I_{yy} = 414724.25831 \text{ mm}^4$,

Torsional constant, $T = 35024 \text{ mm}^4$.

In this analysis, self-weight is disregarded, however, a concentrated vertical load of 11772 N is applied at N_6 . This load is statically applied before the start of the dynamic analysis, for this, all degrees of freedom of the conveyor (wheels and main body), except from the translation in Y direction, are constrained. Once the contact is established and the full load is applied, the guide rail (I-beam) deforms, i.e., at the start of the dynamic analysis, the guide rail is already deformed due to the vertical load being applied through the contact interface. At the start of the dynamic analysis, degrees of freedom of conveyor are released and the vertical load is kept constant (11772 N in negative Y direction). In order to avoid any unexpected lateral vibration, N_5 has its translation in global X direction and rotation about global Y direction restricted during the dynamic analysis. The initial deformation experienced by the I-beam profile is sufficient to make the “free” conveyor to start moving (rolling) along the rail. The dynamic analysis was performed for a total time of 10 s, using fixed time step $\Delta_t = 0.0001 \text{ s}$.

In Figure 5.11 the whole system is illustrated at different instants of the analysis. For visualization purposes, the beam cross section is shown using rendering techniques. The beam axis is also shown coloured according to the Y displacement of each node. In the same picture it is possible to observe the contact surfaces highlighted.

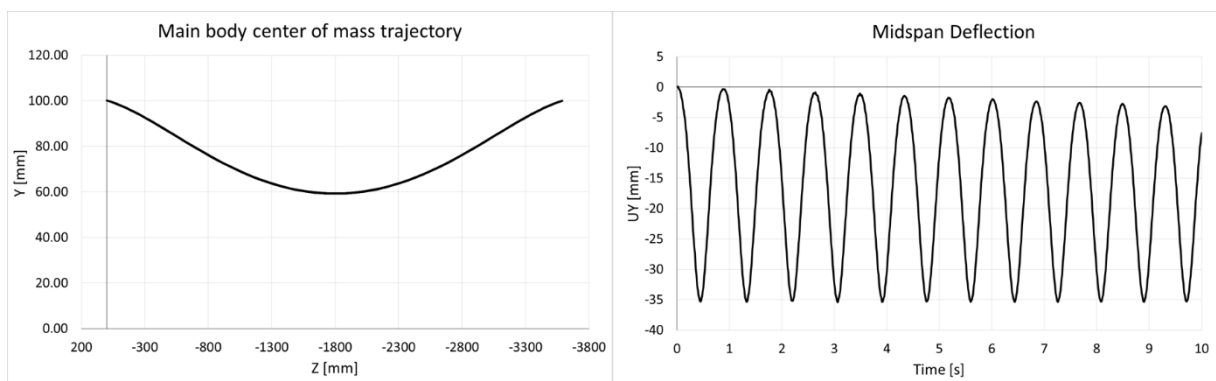
Figure 5.11: Example 5.2 - Global deformation of the guide rail.



Source: [67]

In Figure 5.12 the position of the centre of mass of the main body is plotted in the YZ plane. In the same picture, the midspan deflection (vertical displacement measured for a node located at the mid-length of the I-beam) is also shown.

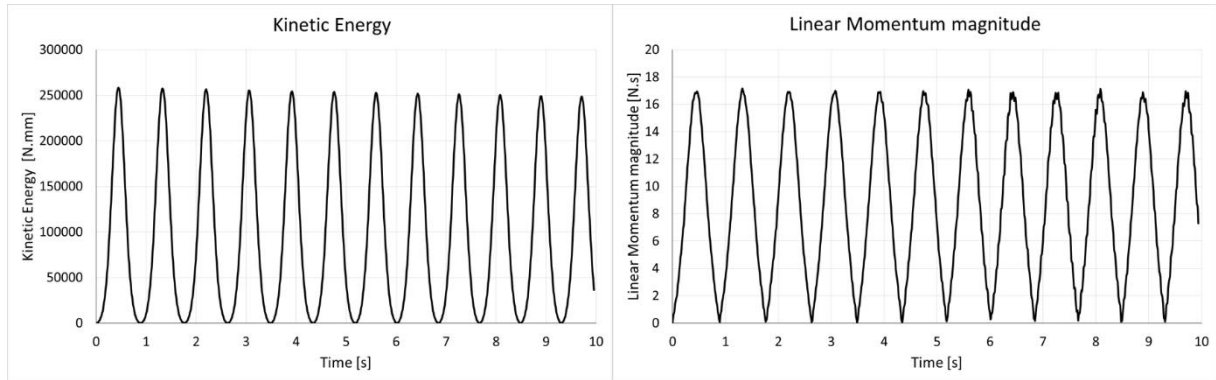
Figure 5.12: Example 5.2 - Conveyor kinematics.



Source: [67]

In Figure 5.13, kinetic energy and the magnitude of linear momentum are plotted accounting for the main body plus the two wheels.

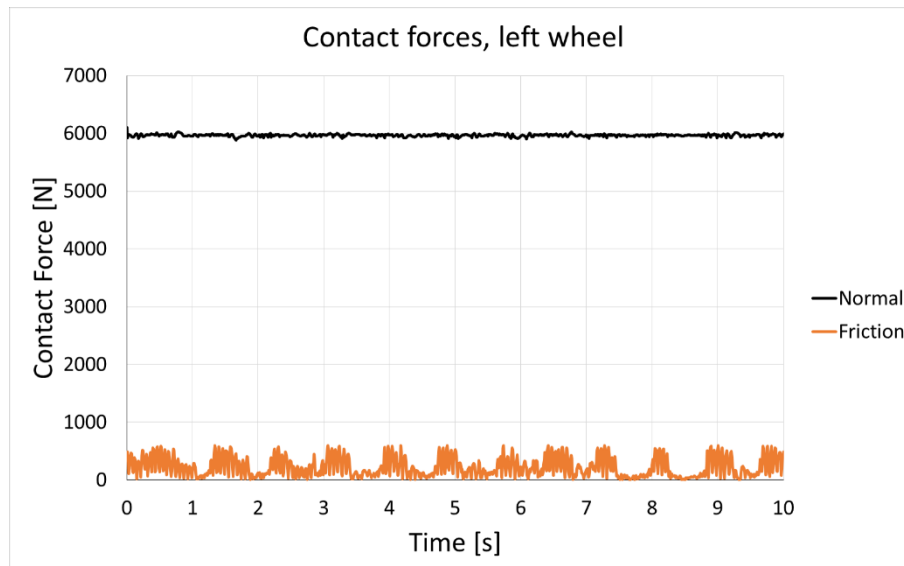
Figure 5.13: Example 5.2 - Conveyor energy and linear momentum magnitude (main body plus wheels).



Source: [67]

Finally, in Figure 5.14, contact forces are shown for the left wheel.

Figure 5.14: Example 5.2 - Contact forces magnitudes (left wheel).



Source: [67]

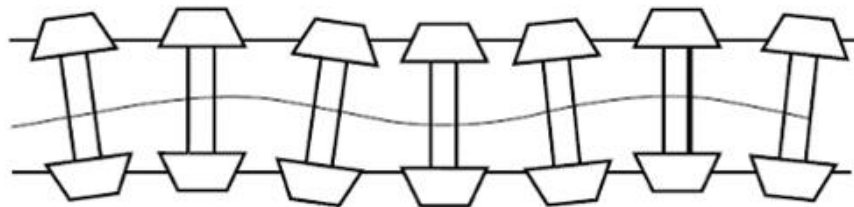
This example shows the possibility of applying our presented model to scenarios of complex kinematics involving flexible together with rigid bodies.

6. RAILWAY CASE

6.1. Hunting phenomenon

The wheelset geometry was already introduced in section 2.1. On the one hand, the conicity of the wheels makes the vehicle orientation in curves easier, since it allows the experience of a difference in rolling radii between both wheels. On the other hand, the conicity may introduce lateral vehicle oscillations, called “hunting” (see Figure 6.1). This oscillation introduces forces into the system, which may cause vehicle and rail damage, discomfort to passengers, and even increase the risk of derailment. The longitudinal speed at which the vehicle becomes unstable is called critical speed and its determination is essential in railway vehicles design.

Figure 6.1: Hunting phenomenon.



Source: [43]

Hunting is nonlinear in its essence. Moreover, this phenomenon is a result of the coupling between the creep forces developed at the wheel-rail contact interface and the lateral and yaw movements of the wheelset. Nevertheless, some classic linearized models are available and can be used to provide a first insight into the phenomenon. In [73], a linearized model based on the equations of movement proposed by Carter in 1916 was reviewed, and critical speeds were evaluated by the first method of Lyapunov [74].

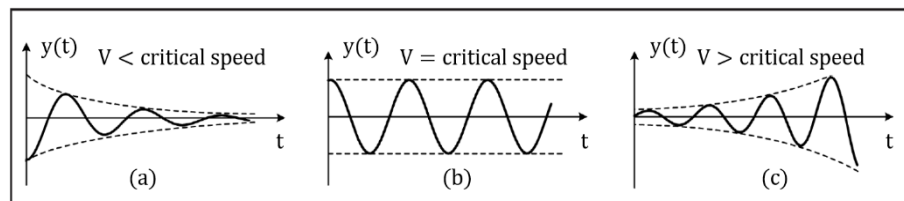
For a quick reference, Carter's equations are presented in expressions (6.1) and (6.2) and an illustration of possible scenarios predicted by this model is provided in Figure 6.2.

$$m\ddot{y} + 2f_{22}\left(\frac{\dot{y}}{V} - \psi\right) + k_y y = 0, \quad (6.1)$$

$$I_z\ddot{\psi} + \frac{2f_{11}l^2}{V}\dot{\psi} + \frac{2f_{11}\gamma l}{r_o}y + k_\psi\psi = 0. \quad (6.2)$$

In these expressions, m and I_z represent the wheelset mass and inertia, respectively; k_y and k_ψ represent lateral and yaw stiffness offered by suspension elements; f_{11} and f_{22} are the longitudinal and lateral linearized creep forces; r_o is the radius of the wheel, $2l$ is the distance between tapelines and γ is the wheel conicity.

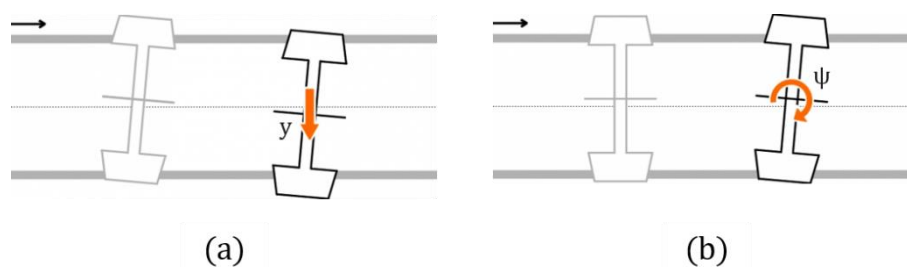
Figure 6.2: Hunting scenarios.



Source: [39]

In Figure 6.3 the degrees of freedom of this model, y and ψ , are illustrated.

Figure 6.3: Model degrees of freedom.



Source: Adapted from [75]

6.1.1. Analytical model for hunting

In [76], one can find data for a typical wheelset, which is reproduced in Table 6.1.

Table 6.1: Railway wheelset properties.

Typical measures for a railway vehicle		
$m = 1250 \text{ kg}$	$f_{11} = 7.44 \text{ MN}$	$k_y = 0.23 \text{ MN/m}$
$I_z = 700 \text{ kg. m}^2$	$f_{22} = 6.79 \text{ MN}$	$k_\psi = 2.5 \text{ MN. m/rad}$
$r_o = 0.45 \text{ m}$	$\gamma = 0.1174$	$l = 0.7452 \text{ m}$

Source: [76]

Using this, the critical speed can be found applying the first method of Lyapunov in equations (6.1) and (6.2). The first step of the method consists of reducing the system of equations into a first order system, by introducing state variables

$$x_1 = y, \quad x_2 = \psi, \quad x_3 = \dot{y}, \quad x_4 = \dot{\psi}. \quad (6.3)$$

So that,

$$\dot{x}_1 = x_3, \quad \dot{x}_2 = x_4, \quad \dot{x}_3 = \ddot{y}, \quad \dot{x}_4 = \ddot{\psi}. \quad (6.4)$$

Then, equations (6.1) and (6.2) can be rewritten as

$$\ddot{y} = -\frac{1}{m} \left(2f_{22} \left(\frac{\dot{y}}{v} - \psi \right) + k_y y \right), \quad (6.5)$$

and

$$\ddot{\psi} = -\frac{1}{I_z} \left(\frac{2f_{11} \gamma l y}{r_o} + \frac{2f_{11} l^2 \dot{\psi}}{v} + k_\psi \psi \right). \quad (6.6)$$

In matrix form:

$$\dot{\mathbf{x}} = \mathbf{A}\mathbf{x} \rightarrow \begin{Bmatrix} \dot{x}_1 \\ \dot{x}_2 \\ \dot{x}_3 \\ \dot{x}_4 \end{Bmatrix} = \begin{bmatrix} 0 & 0 & 1 & 0 \\ 0 & 0 & 0 & 1 \\ -\frac{k_y}{m} & \frac{2f_{z2}}{m} & -\frac{2f_{z2}}{mV} & 0 \\ -\frac{2f_{11}\gamma l}{I_z r_o} & -\frac{k_\psi}{I_z} & 0 & -\frac{2f_{11}l^2}{I_z V} \end{bmatrix} \begin{Bmatrix} x_1 \\ x_2 \\ x_3 \\ x_4 \end{Bmatrix}. \quad (6.7)$$

One can extract the eigenvalues of matrix \mathbf{A} , and the theorem says:

- If all eigenvalues of \mathbf{A} have negative real part, i.e., $Re_k < 0$, then the state is said to be Lyapunov-Stable.
- On the other hand, if at least one of the eigenvalues of \mathbf{A} has a positive real part, i.e., $Re_k > 0$, then the state is said to be Lyapunov-Unstable.
- Finally, if $Re_k = 0$, the state is said to be Lyapunov-Critical.

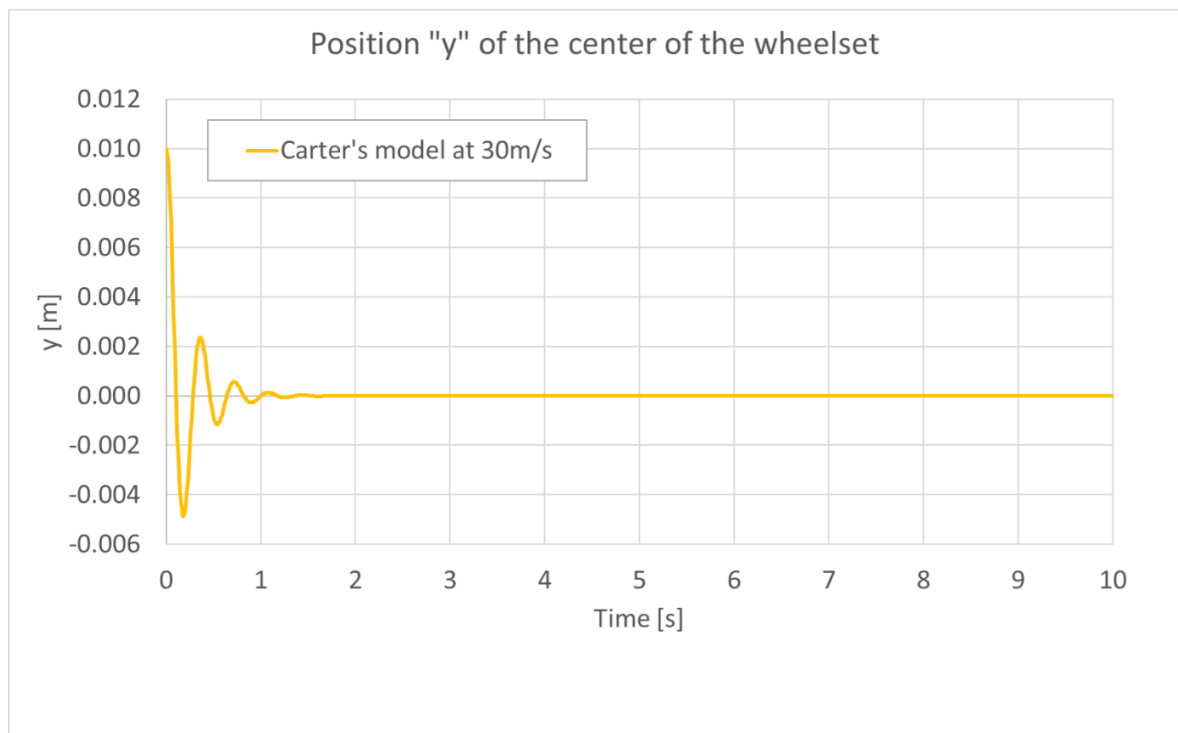
These steps can be applied in a straightforward manner to determine the critical speed of a railway vehicle. Using the characteristics provided in Table 6.1, one can calculate matrix \mathbf{A} and then, a very simple routine can be developed to find the critical speed, as follows:

1. Define a starting (null) value for velocity, $V = 0.0$ m/s
2. Define an increment for the calculations. For example, define $inc = 0.01$ for obtaining critical speeds with a precision of two decimal places.
3. Extract eigenvalues of \mathbf{A} for the current value of V .
4. Check if $Re_k \geq 0$, with $k = 1, 2, 3$ and 4 .
5. If all eigenvalues have negative real part, increase the current value of V by inc and repeat the process from step 3 to step 5. Otherwise, stop the calculation and evaluate the current value of V , it will represent the critical speed.

By performing these five steps for the model proposed in Table 6.1, the critical speed for this vehicle is found to be 74.26 m/s (267.3 km/h).

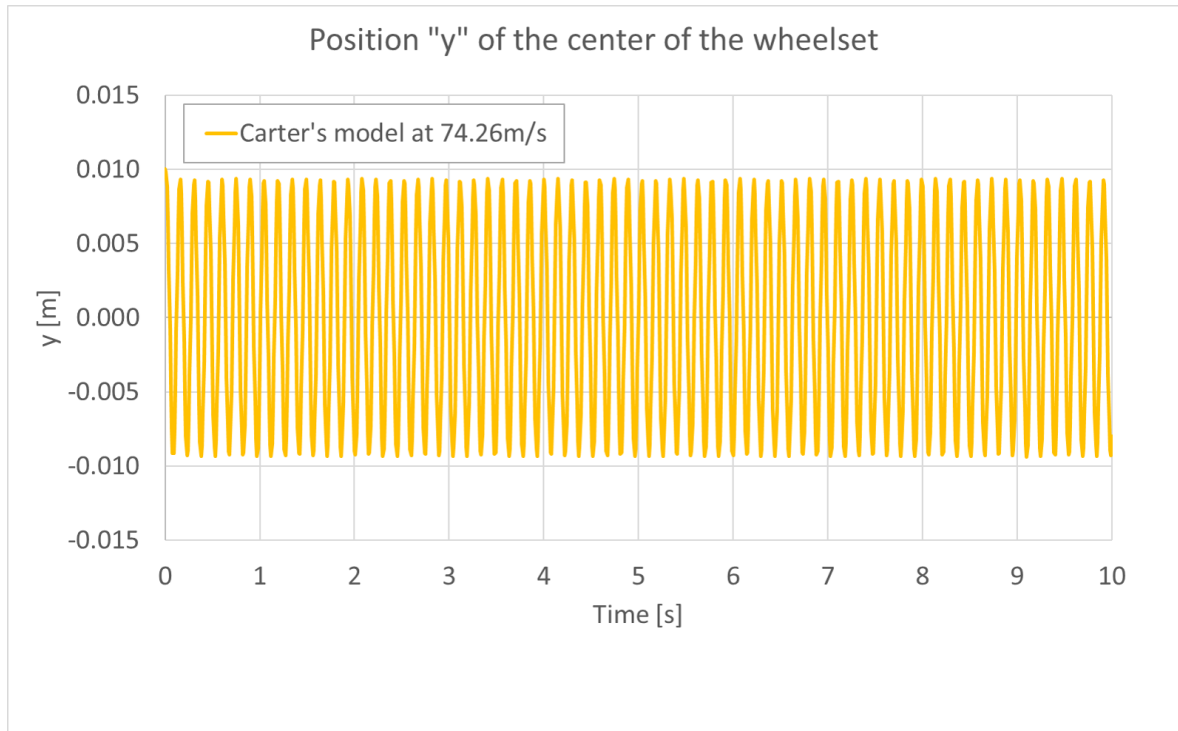
Once the critical speed is known, one can check if the conditions illustrated in Figure 6.2 are satisfied. To do that, we performed time integration of Carter's equations considering an initial lateral offset of 0.01 m. Results are shown for cases below critical speed, at critical speed and above critical speed (Figure 6.4, Figure 6.5 and Figure 6.6, respectively).

Figure 6.4: Time evolution of lateral displacements y for an initial lateral offset of 0.01m. Below critical speed: $V = 30.0$ m/s.



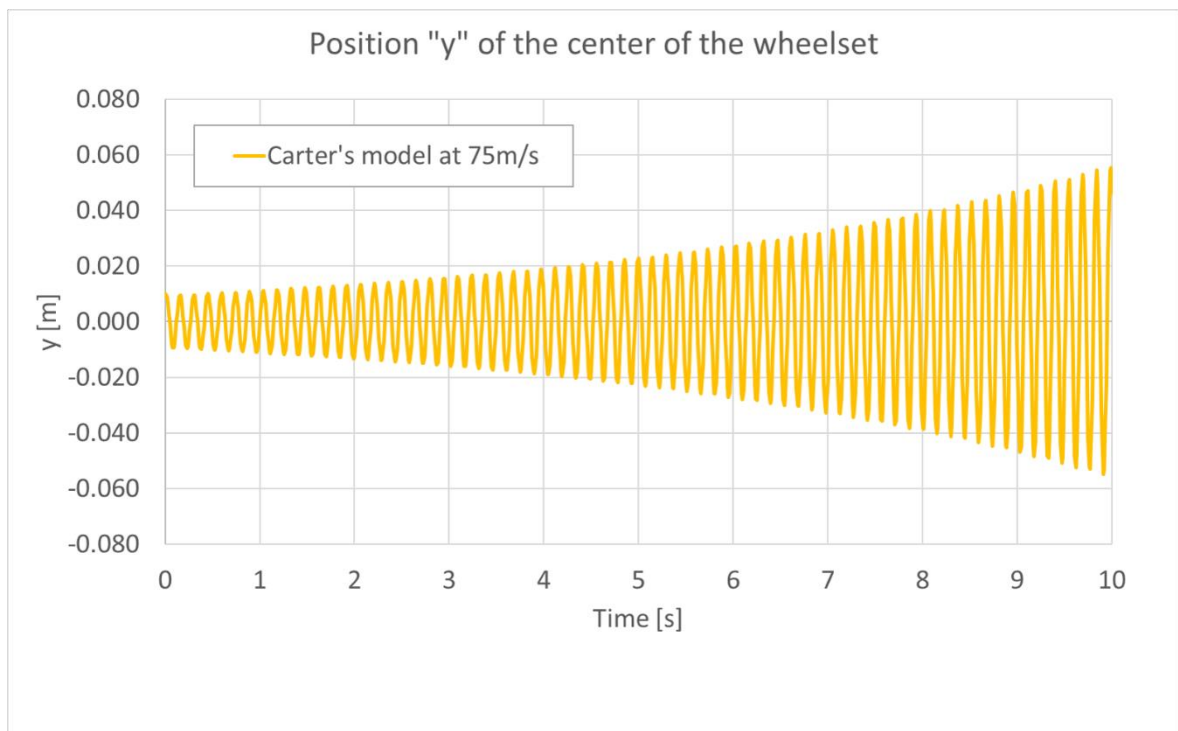
Source: [73]

Figure 6.5: Time evolution of lateral displacements y for an initial lateral offset of 0.01m. At critical speed: $V = 74.26$ m/s.



Source: [73]

Figure 6.6: Time evolution of lateral displacements y for an initial lateral offset of 0.01m. Above critical speed: $V = 75.0$ m/s.

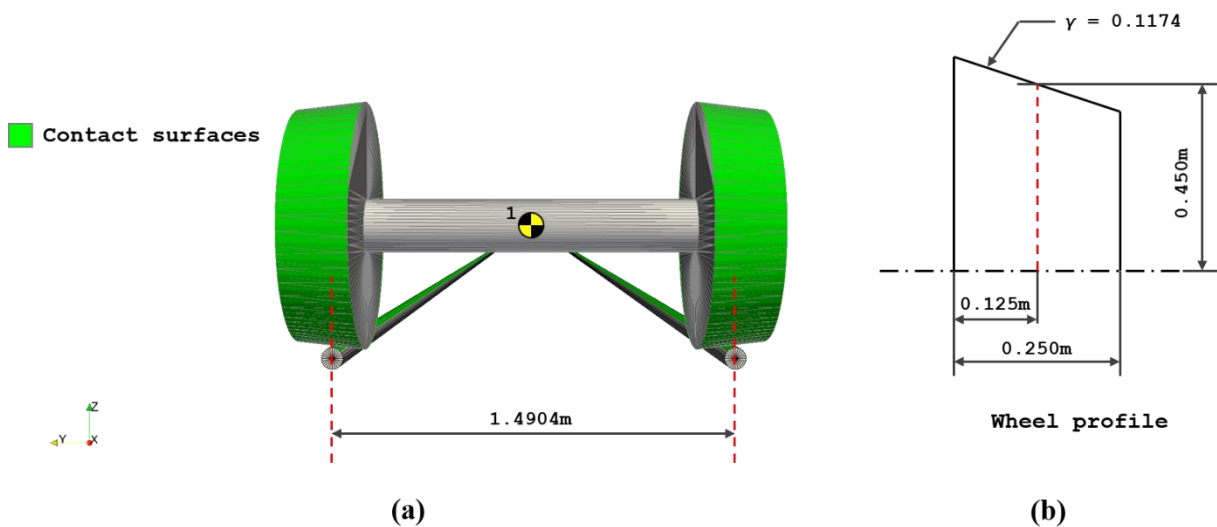


Source: [73]

6.1.2. Nonlinear simplified model for hunting

In this section, a first railway application is presented using the rigid body and the contact models developed in this work. For this purpose, the same case presented in the previous section is solved in a nonlinear approach. In Figure 6.7, the nonlinear model used in conjunction with the master-master contact formulation is shown. Figure 6.7 (a) presents an overview of the model. A rigid body is defined at point 1, this element is free to move in any direction, except from longitudinal direction (x), which has an imposed constant forward speed. Contact surfaces are shown in green: rails are idealized as rigid beams with circular cross section with radius of 0.04 m and the rigid wheel profile is depicted in Figure 6.7 (b). As can be observed, the conical surface representing the wheel tread is an arc with a very large radius, which is an approximation for a straight line.

Figure 6.7: Nonlinear model: (a) General overview of wheelset model. (b) Wheel profile dimensions.



Source: [73]

The rigid body shown in Figure 6.7 has the same properties of the model of Table 6.1. In addition, since it is a 3D model, it was necessary to define $I_x = 700 \text{ kg} \cdot \text{m}^2$ and $I_y = 115 \text{ kg} \cdot \text{m}^2$. A constant load of 78480 N (4 tonnes per wheel) was applied. Carter's model does not use a coefficient of friction explicitly. However, linear creep coefficients from Kalker's linear theory (f_{11} and f_{22}) are assumed. Only Coulomb's

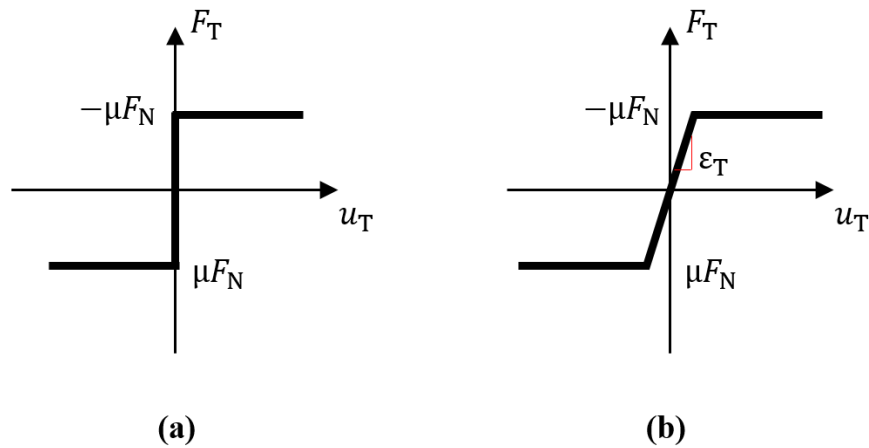
friction law is available in our formulation and therefore a coefficient of friction, $\mu = 0.3$ was adopted for the nonlinear model. Moreover, in the current release of Giraffe, it is not possible to represent lateral and yaw stiffness (k_y and k_ψ). Although the influence of k_y and k_ψ was not studied here, one can see that assuming null stiffness for both parameters drastically reduces the critical speed. Actually, the model becomes unstable for any velocity in such scenario.

To obtain some reasonable results, the simulation was performed for a constant speed of 15.0 m/s. Although this is much lower than the critical speed predicted in the previous section, since null values were assumed for k_y and k_ψ , unstable behaviour is expected.

At this point, it is worth mentioning that there exist important differences between the Coulomb's friction law (used in Giraffe) and the linear creepage theory (used together with the Carter's model). In Figure 6.8 (a), classical Coulomb's frictional behaviour is illustrated: once the tangential forces are above a certain limit (proportional to the compressive normal contact force $F_N \leq 0$, and to the friction coefficient μ) the contacting surfaces start (suddenly) sliding. On the other hand, as mentioned in Chapter 2, friction laws involving the concept of creepage allows micro slips within the contact area even before a saturation limit is achieved.

In fact, to avoid the non-differentiability of the Coulomb's law, in numerical procedures the tangential constraint is imposed by techniques such as the penalty method. The penalty factor ε_T used to impose the tangential constraint can notably influence the overall behaviour of the model. While very high penalty factors impose conditions such as that illustrated in Figure 6.8 (a), if penalty factors are relaxed, slippage between surfaces can be observed before the saturation limit is achieved (see Figure 6.8 (b)). The tangential penalty factor ε_T is a numerical parameter related to the implementation of the friction constitutive law in a penalty approach. Therefore, it doesn't need to have a physical meaning associated to it. However, one can identify some similarities between the effect of varying penalty factors and the concept of creepage, i.e., the ε_T chosen defines how much sliding occurs before the saturation limit is reached in a numerical model, and creepage is the amount of slipping observed within a contact area before complete slip occurs (see Chapter 2).

Figure 6.8: Frictional behaviour. (a) Coulomb's law. (b) Coulomb's law in a penalty approach.



Source: Adapted from [19]

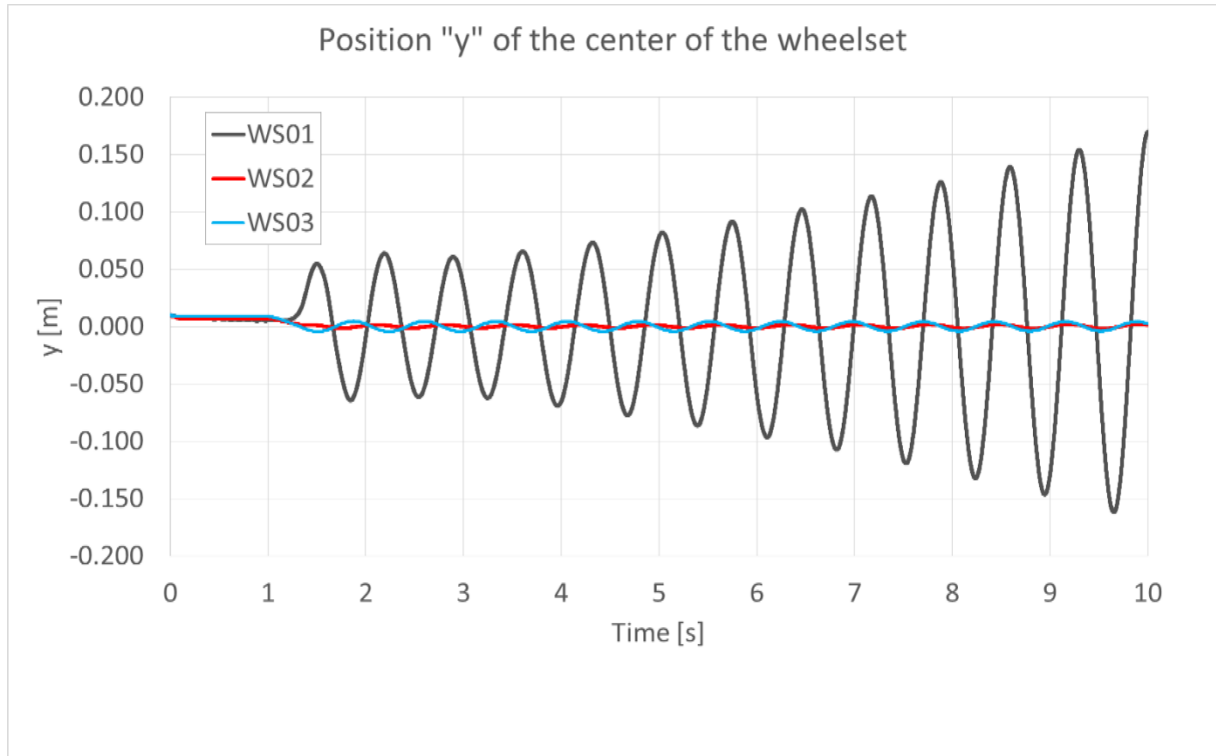
For the model described above, three analyses were performed varying the tangential penalty factor. The normal penalty factor was kept constant between different models ($\epsilon_N = 1.0e+008$ N/m). Table 6.2 summarizes the model properties and the results are shown in Figure 6.9.

Table 6.2: Nonlinear models.

Model	ϵ_N [N/m]	ϵ_T [N/m]	V [m/s]
WS01	1.0e+008	1.0e+007	15
WS02	1.0e+008	1.0e+008	15
WS03	1.0e+008	1.0e+009	15

Source: [73]

Figure 6.9: Nonlinear model response: time evolution of lateral displacements for different tangential penalty factors. Speed: 15.0 m/s.

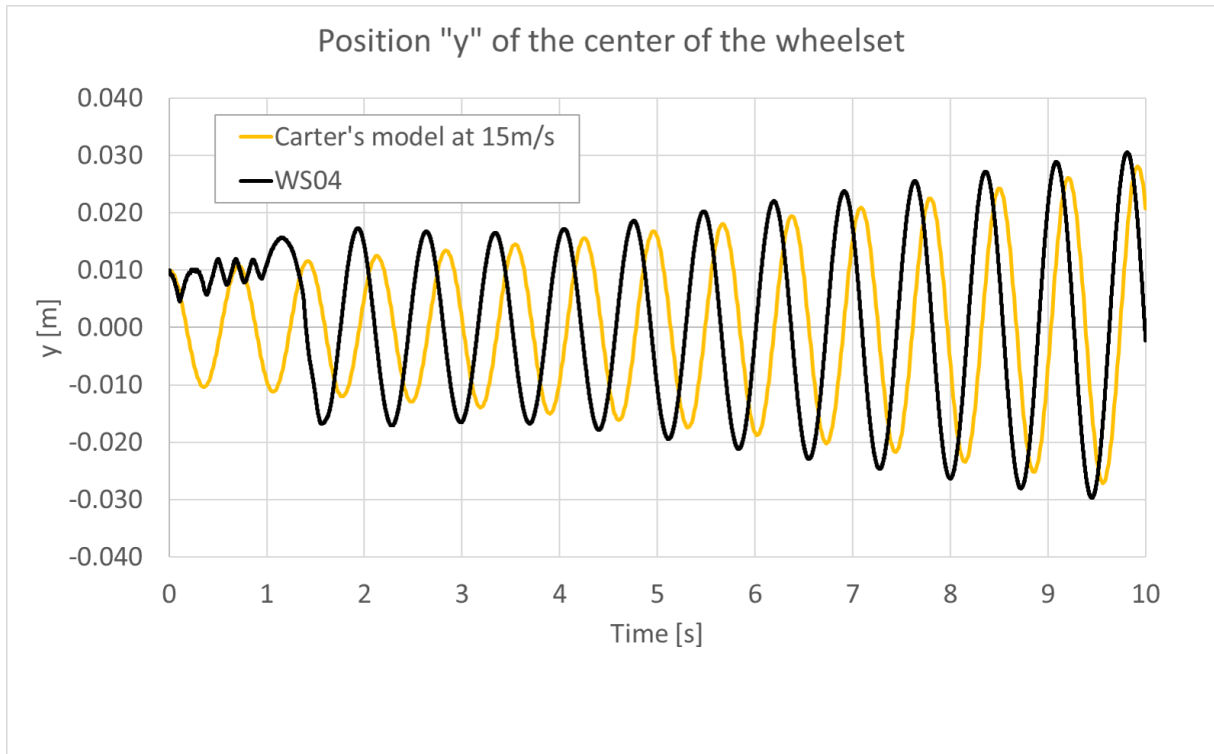


Source: [73]

As already pointed out, the dynamic behaviour of the system is severely influenced by the choice of ε_T . Using higher values in models WS02 and WS03 resulted in a better representation of Coulomb's friction law. For these cases, an important parcel of the energy of the system is dissipated through the contact interface, mitigating the hunting phenomenon. On the other hand, relaxing ε_T (model WS01) can be interpreted as if some kind of creep law was included in the model, making it possible to capture the hunting phenomenon.

Therefore, for the same model, the tangential penalty factor was adjusted in order to obtain results similar to those predicted by Carter's equation at a speed of 15.0 m/s and assuming $k_y = k_\psi = 0$. A model identified as WS04 was generated, and $\varepsilon_T = 3.6e+007$ N/m was employed. Comparative results are shown in Figure 6.10.

Figure 6.10: Nonlinear model response: time evolution of lateral displacements for $\varepsilon_T = 3.6e+007$ N/m. Speed: 15.0 m/s.



Source: [73]

The hunting phenomenon is indeed observed in practice. As shown in the previous example, the strict Coulomb's friction law may not be adequate to study such kind of phenomenon since the saturation of friction can mitigate its occurrence. However, if implemented using penalty techniques, the penalty parameter can be calibrated in order to have something similar to a linear creep law. The correct calibration of penalty factors for this purpose is a subject of future studies. It can be done based on Kalker's linear theory or experimental data, for example. Moreover, the implementation of friction laws other than the Coulomb's one together with the master-master formulation is promising and would allow deeper investigations of nonlinear lateral stability of railway vehicles.

6.2. Wheelset example

To conclude this work, a model with realistic wheel and rail profiles is developed. Interesting initial results are presented, the capability of representing complex contact surfaces is shown and the possibility of capturing multiple contact

points is demonstrated. The analysis is performed using a fully nonlinear transient dynamic procedure in GIRAFFE platform [36]. Newmark method is employed for time integration, with parameters $\beta = 0.3$ and $\gamma = 0.5$.

In this example, the rigid body formulation is used together with the contact formulation presented in this work to represent an isolated wheelset running over a tangent track. Figure 6.11 provides an overview of this model. A rigid body element was defined at point N_1 . This point corresponds to the centre of mass of the wheelset. The following data was considered:

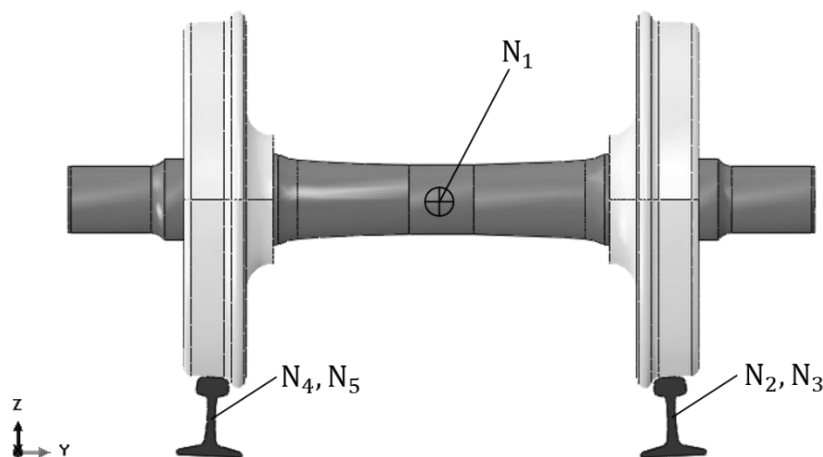
Unit system: N, mm, tonne, s,

Mass, $m = 1.05$ tonne,

$$\text{Inertia tensor, } \mathbf{J} = \begin{bmatrix} 78688.53 & 0 & 0 \\ 0 & 310377.97 & 0 \\ 0 & 0 & 310377.97 \end{bmatrix} \text{ tonne} \cdot \text{mm}^2.$$

Note: \mathbf{J} is provided with respect to local barycentric axes aligned with the global axes.

Figure 6.11: Wheelset example - Global overview of the model.



Source: Author

The right-side rail is represented by arcs extruded between two fixed nodes (N_2 and N_3), the left-side rail is represented in the same way, but between N_4 and N_5 . The coordinates of the nodes of this model are provided in Table 6.3.

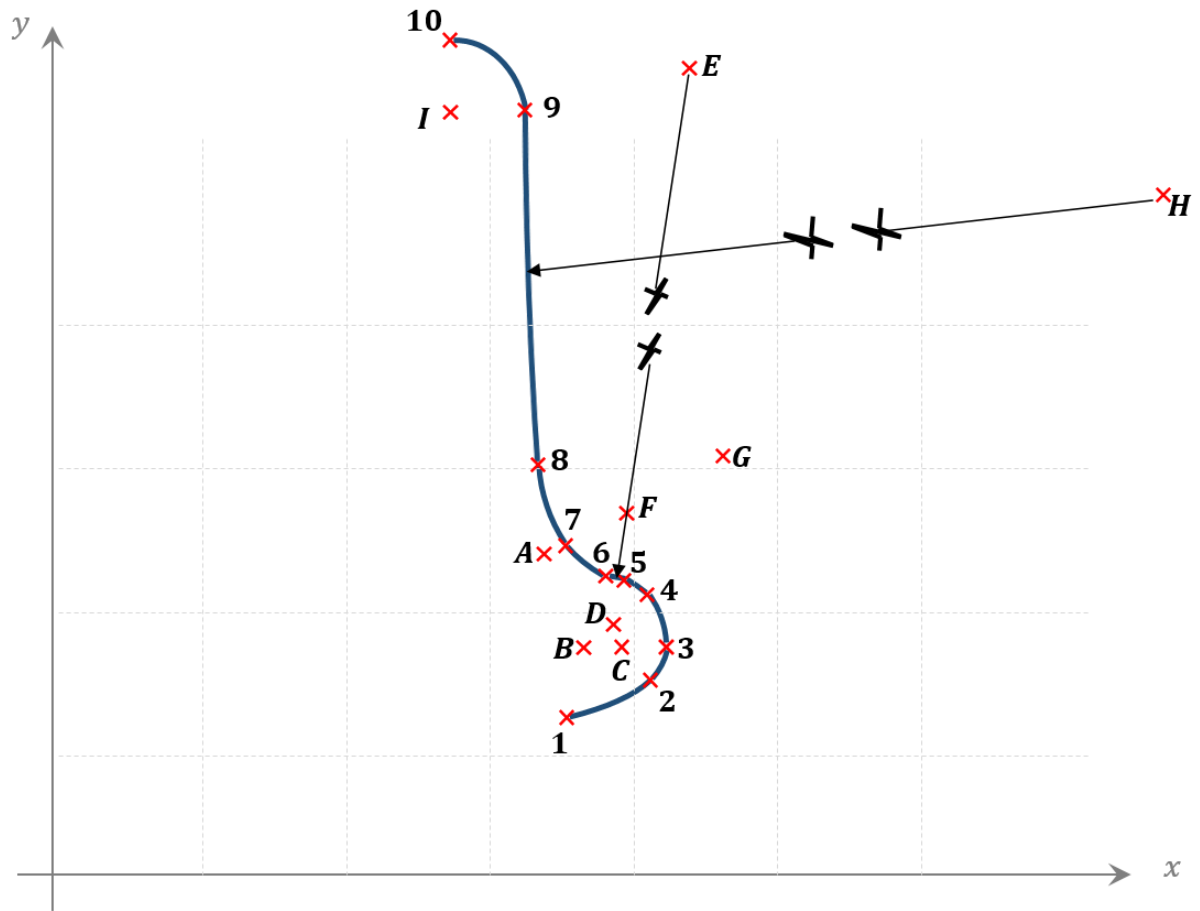
Table 6.3: Wheelset example - Global coordinates of points.

Point	X [mm]	Y [mm]	Z [mm]
N_1	0.000000	0.000000	1.000000
N_2	-1500.000000	542.116031	-518.54463
N_3	150000.000000	542.116031	-518.54463
N_4	-1500.000000	-542.116031	-518.54463
N_5	150000.000000	-542.116031	-518.54463

Source: Author

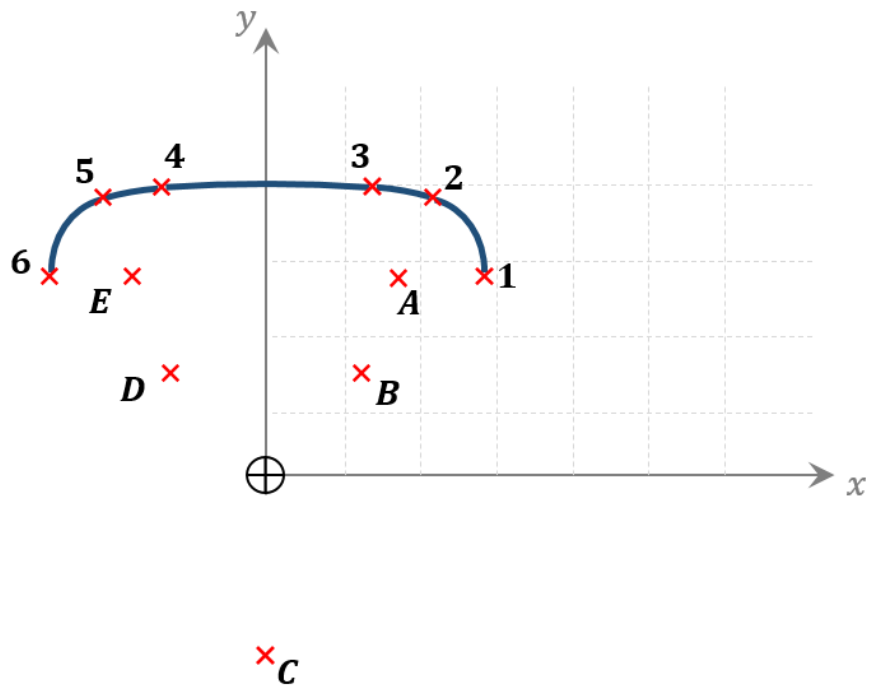
In Figure 6.12 and Figure 6.13, the arcs used to generate contact surfaces are presented. The same approach introduced in section 5 was used, i.e., arcs were defined in local coordinate systems and then positioned in the global model. The arcs used to represent the wheel are revolved about local y axis. Local coordinates of each arc illustrated in Figure 6.12 and Figure 6.13 are provided in Table 6.4 and Table 6.5. Each surface can be easily identified by the nomenclature “S” + “Centre of arc” + “Start point” + “Final point”. For example, the first surface is identified as “SA12”. This will be useful for post-processing purposes.

Figure 6.12: Wheelset example – contact arcs for wheel.



Source: Author

Figure 6.13: Wheelset example – contact arcs for rail.



Source: Author

Table 6.4: Wheelset example - Local coordinates of contact arcs for wheel.

Point	x [mm]	y [mm]
A	420.772324550	493.855724000
B	437.073924550	474.376824000
C	429.139524550	474.376324000
D	435.400024550	479.251124000
E	1195.351924550	3391.247724000
F	438.056924550	503.193124000
G	458.867224550	515.447124000
H	2737.316343850	667.415368146
I	400.805124550	588.677024000
1	425.796324550	459.294424000
2	443.093824550	466.995524000
3	446.598824550	474.376824000
4	442.715724550	485.354124000
5	437.721524550	488.491124000
6	434.369224550	489.368124000
7	425.821324550	495.775524000
8	420.459624550	513.482624000
9	416.660224550	589.469724000
10	400.805124550	604.552024000

Source: Author

Table 6.5: Wheelset example - Local coordinates of contact arcs for rail.

Point	x [mm]	y [mm]
<i>A</i>	22.574561	84.907321
<i>B</i>	16.192500	68.652838
<i>C</i>	0.000000	-254.792096
<i>D</i>	-16.192500	68.652838
<i>E</i>	-22.574561	84.907321
1	36.857598	85.264398
2	27.796247	98.206443
3	17.780000	100.363126
4	-17.780000	100.363126
5	-27.796247	98.206443
6	-36.857598	85.264398

Source: Author

It is important to observe that the coordinates of the points used to generate the wheel surface take into account the position of the wheel already assembled in the axle, i.e., the only necessary operation in GIRAFFE is to properly reflect the points in order to represent right-side or left-side. For the rail, the coordinates used to generate the surface are provided vertically aligned with the local Y axis. Therefore, in addition to the reflect operation, if desired, the surfaces can be inclined to represent practical cant values. In this example, a cant of 1:20 was considered.

The wheelset is initially centred in the track. A vertical load of 186390.0 N (19 tonnes) is statically applied at the start of the analysis and kept constant during the whole simulation. Node N_1 is free in all directions except for the X one, which after 5 s of simulation is prescribed with a constant forward velocity of 1.0 m/s.

After 10 s of simulation, an impulsive load is applied to the centre of mass of the wheelset (node N_1). The force is applied in the global Y direction and its time history is presented in Table 6.6 (linear interpolation is assumed between time-values shown in the table).

Table 6.6: Wheelset example - Force time history.

Time [s]	FY [N]
0.0	0.0
10.0	0.0
10.3	100000.0
10.4	0.0

Source: Author

A coefficient of friction $\mu = 0.3$ was considered. Normal and tangential penalty factors were defined as $5.0e+005 \text{ N/mm}$ and $5.0e+004 \text{ N/mm}$, respectively. A normal damping, equal to 50 N.s/mm , was employed at the contact interface⁵. The analysis was performed using a fixed time step $\Delta_t = 0.001 \text{ s}$, for a total time of 35 s.

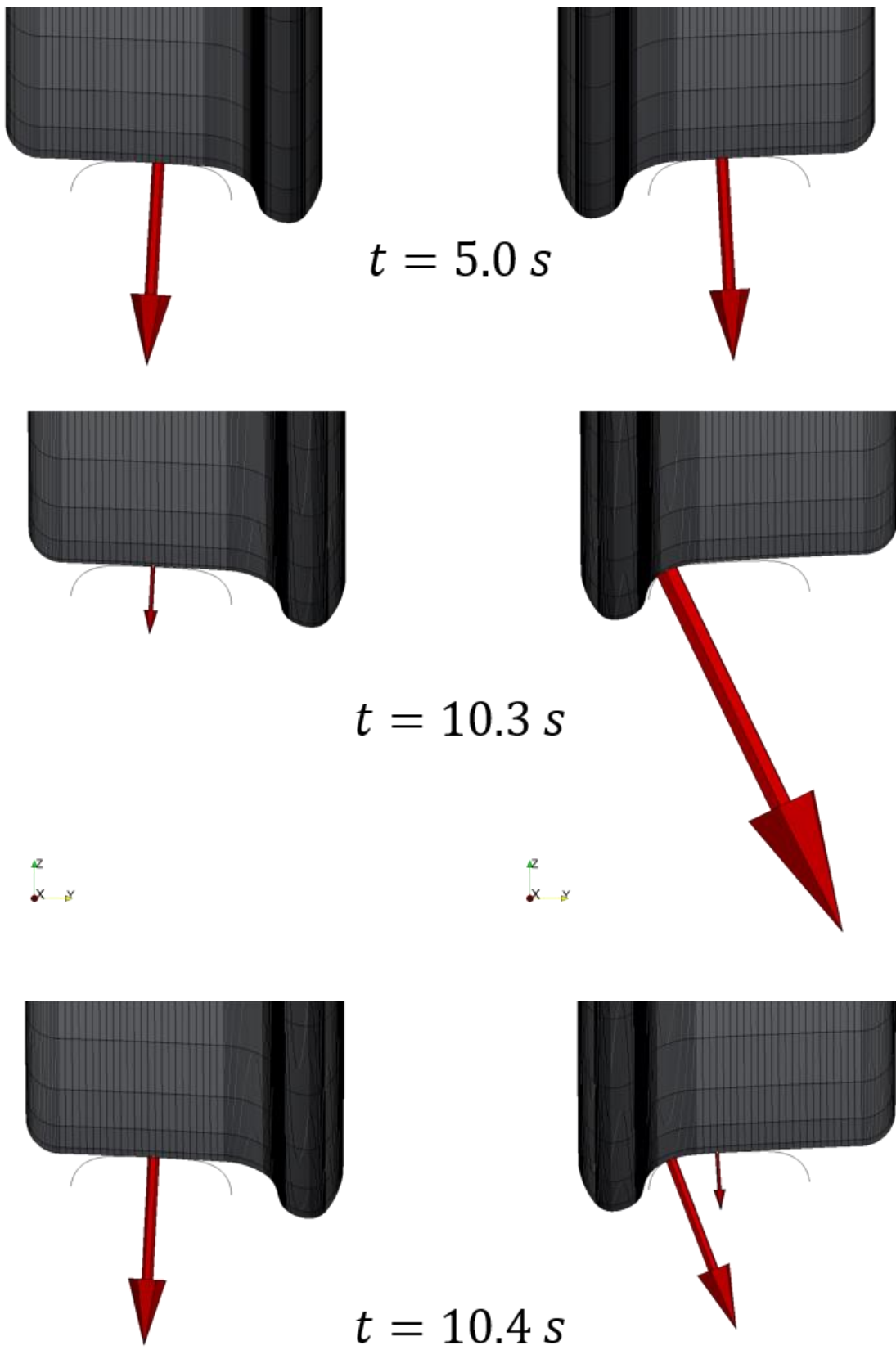
In Figure 6.14 and Figure 6.15 the system is illustrated at different instants of the analysis. As can be observed in Figure 6.14, at the moment in which the wheelset starts rolling (at 5 s) it is laterally positioned in the centre of the track and the vertical load is equally distributed between the two rails. At 10.3 s, when the impulse load is completely applied (see Table 6.6), a very high impact occurs between the flange root and the gauge corner of the right wheel-rail interface. The impact is strong enough to cause the loose of contact in the tread region of the same wheel and the distribution of load between rails is also affected, letting the left-side less loaded. At 10.4 s, when the impulse load is completely removed, the wheelset starts moving laterally to the left (because of the self-centring capacity of conical wheels). It is important to observe that at this instant, two contact points are established in the right-side, one between the wheel tread and the rail crown and the other between the wheel flange root and the rail shoulder. Figure 6.15 also shows the time evolution of the analysis and multiple points of contact are captured as the wheelset oscillates in a search for its equilibrium position.

As mentioned before, there is no suspension elements in such kind of model in GIRAFFE. Therefore the system is unstable for any imposed velocity. Moreover, the penalty factors used here were chosen in a way to avoid large interpenetration between

⁵ The damping model employed is based on a standard linear dissipation with respect to relative speed of surface material points on contact interface. One may see details of application of similar models in the context of rigid balls with surfaces in [72].

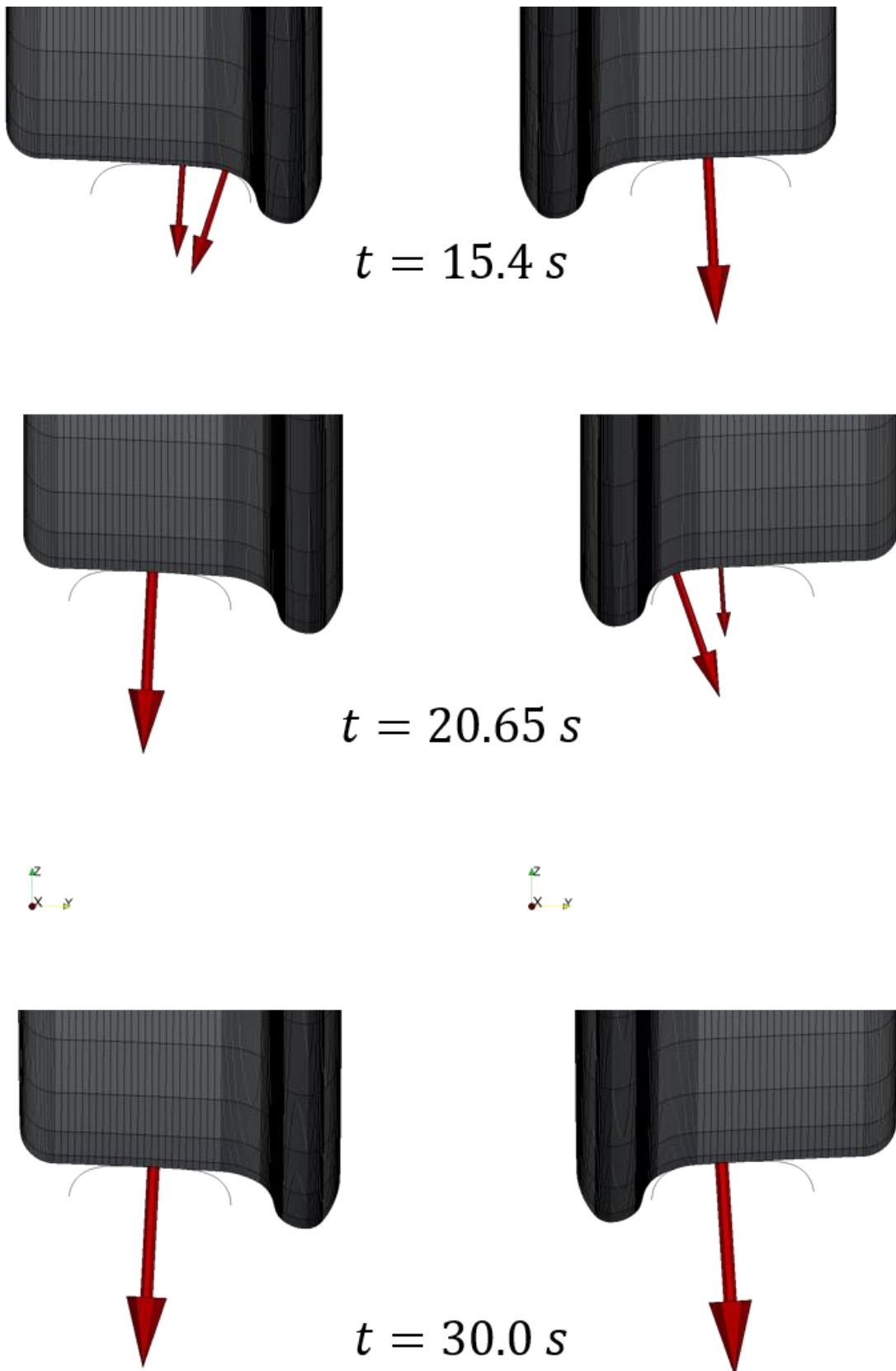
the bodies but the values were not calibrated using theoretical neither experimental data. The purpose of this example was to show an application of the developed models in a more complex scenario, with elaborate contact surfaces and multiple points of contact.

Figure 6.14: Wheelset example – contact detection.



Source: Author

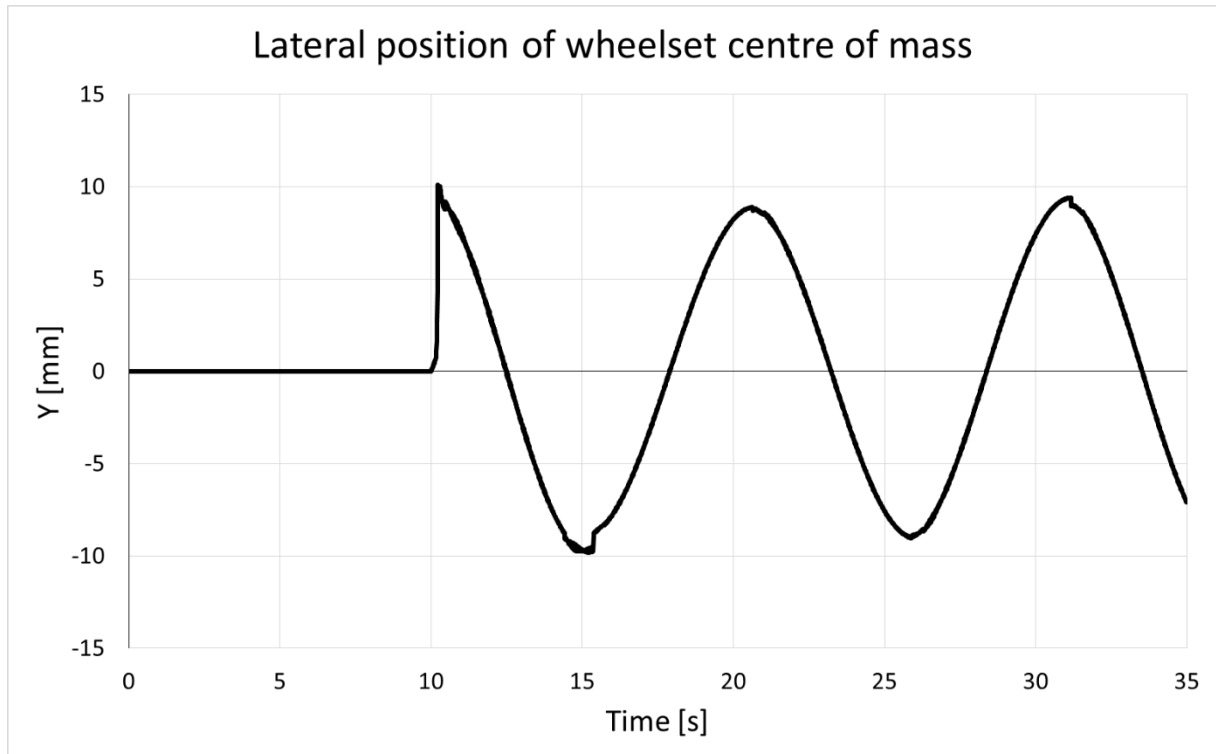
Figure 6.15: Wheelset example – contact detection.



Source: Author

An output of interest of this analysis is the lateral position of the centre of mass of the wheelset along the simulation. It can be seen in Figure 6.16.

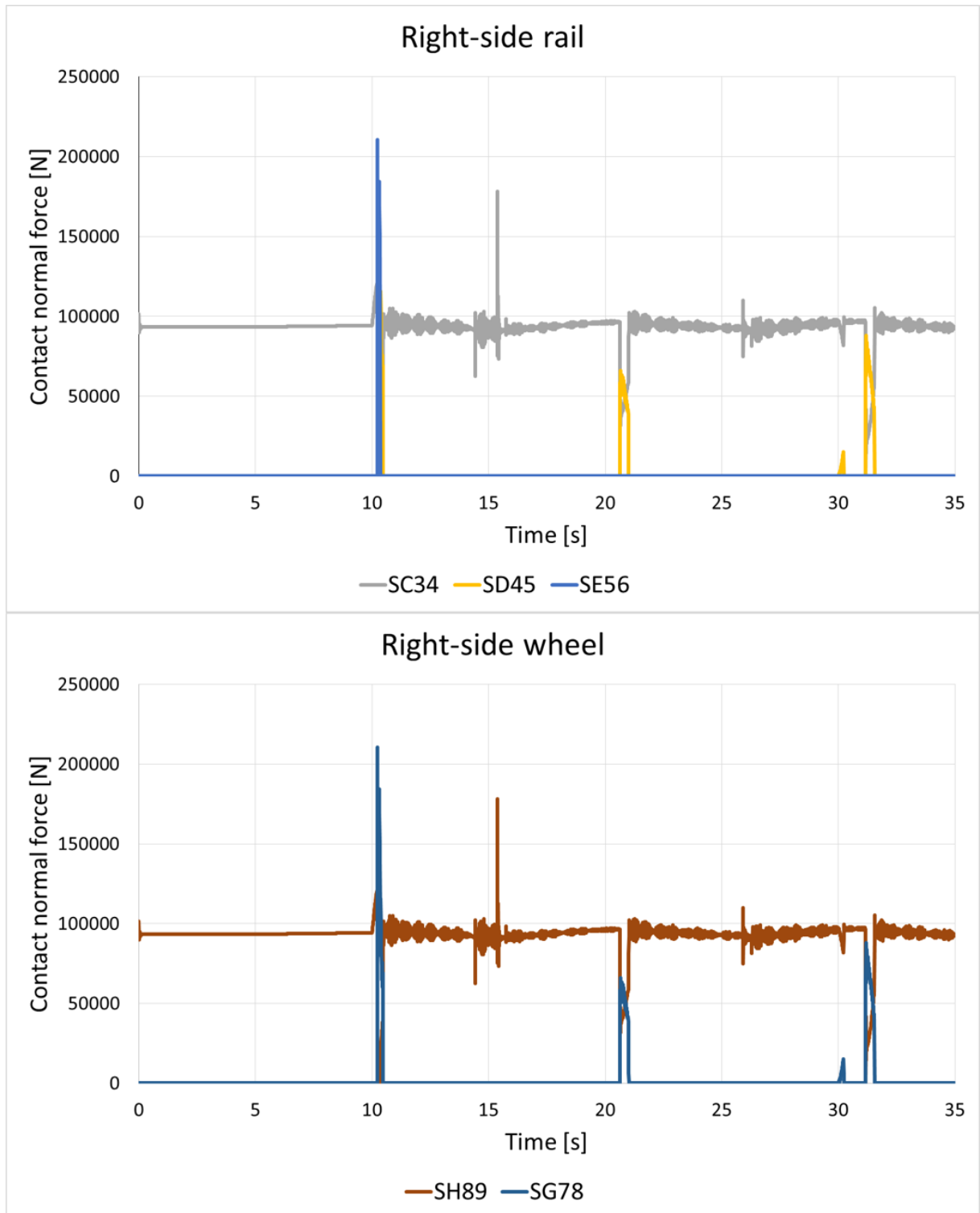
Figure 6.16: Wheelset example – lateral position of centre of mass.



Source: Author

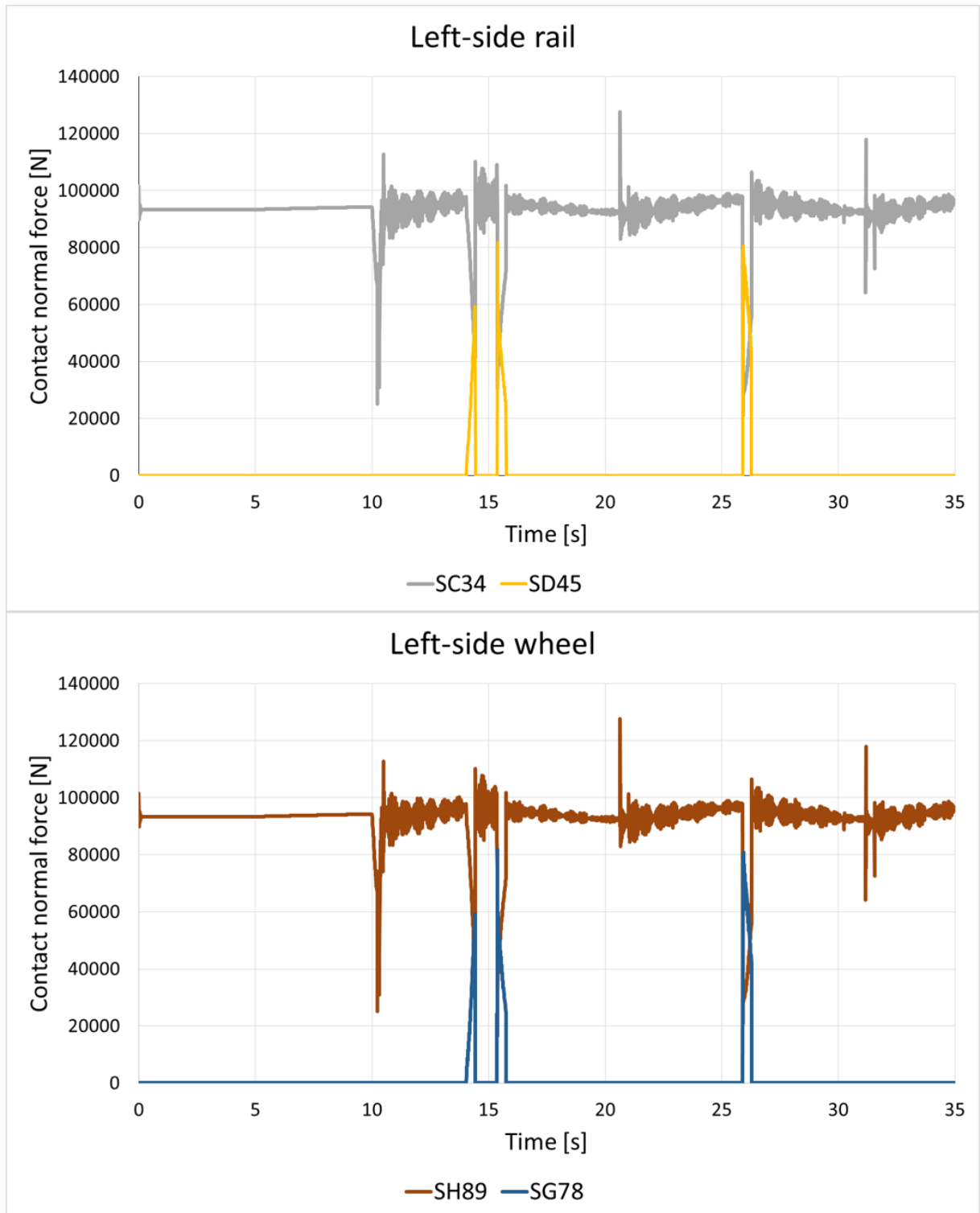
The contact force along the simulation is another example of output that can be obtained from this analysis. Figure 6.17 and Figure 6.18 shows the normal contact forces for both rail and wheel at right and left sides. The absolute value of the contact force for a point in the wheel is the same as that for the corresponding contact point in the rail. However, it is interesting to present both results because the surfaces where the contact is occurring can be identified. In Figure 6.17 the impact occurring at 10.3 s is clearly identified. Moreover, it is possible to see that it occurs between surface “SE56” on the rail side and “SG78” on the wheel side. Checking this with Figure 6.12 and Figure 6.13, it is possible to see that these surfaces correspond to the rail gauge corner and wheel flange root, respectively.

Figure 6.17: Wheelset example – contact normal force for the right side.



Source: Author

Figure 6.18: Wheelset example – contact normal force for the left side.



Source: Author

7. SUMMARY AND OUTLOOK

In this work a formulation to employ rigid bodies together with flexible bodies in the context of a nonlinear finite element solver, with contact interactions, was presented. Inertial contributions due to distribution of mass of a rigid body were fully developed, considering a general pole position associated with a single node, representing a rigid body element. Rodrigues rotation parameters were used to describe finite rotations, by an updated Lagrangian description. In addition, new surface parameterizations were presented to establish contact pairs in a pointwise frictional master-surface to master-surface approach. The versatility and the power of such kind of framework, i.e., a nonlinear finite element environment designed to simulate multibody systems, was explored through numerical examples coming from different contexts.

Both the rigid body and the surface parameterizations developed in this work showed very promising results. The rigid body element represents an efficient way for accounting mass and inertia of a solid body when stresses and strains can be disregarded. The possibility of choosing any generic position for placing the rigid body node, i.e., the pole position does not need to be coincident with the centre of mass of the body, makes the practical use of this kind of element very convenient. Moreover, the use of Rodrigues parameters to describe finite rotations in the rigid body formulation was a key point that allowed the introduction of this element in the same environment of several other finite elements developed previously, such as beams and shells presented in [71] and [77]. Rodrigues parameterization has the main advantage of being simple because it does not involve trigonometric functions. This characteristic makes this formulation computationally efficient. The inherent singularities when rotation approaches $\pm\pi$ can be overcome by employing an updated Lagrangian scheme, as presented in this work.

The new parameterization of an extruded surface based on arcs made it possible to establish contact between beams considering arbitrary cross-sections. This was shown in the overhead conveyor example in this work, where contact was

established between wheels of a trolley and the lower web of an I-shaped beam element. The revolved surface based on arcs is also very general. However, it is designed to be used in conjunction with only one node, for example the node of a rigid body element. Both surfaces together expanded the range of applicability of the master-surface to master-surface contact formulation, which was limited to super-elliptical surfaces in its first version (see [29] and [30]).

The focus of the present work was on the development of the rigid body element and in the application of the master-surface to master-surface contact formulation to the context of multibody dynamics. Therefore, the important subject of time-integration algorithms was not considered in our discussion. However, we recognize this as a necessary enhancement to be applied together with our proposed formulation. The numerical examples here presented were done employing the special version of Newmark method from [14], a more detailed discussion on this subject can be found in [18]. Nevertheless, any other time-integration scheme could be employed together with the developed models, including energy-momentum methods (e.g.: [70] and [78]). Such kind of improvements are going to be addressed in future works.

Regarding the contact formulation, the new surface parameterizations are very versatile and can be used to represent a large range of geometries. However, it is difficult to propose a general initial guess, necessary for solving the local contact problem (equation (3.24)) with the traditional Newton-Raphson method. As a consequence, it is not uncommon to face convergence difficulties during the solution, especially when the geometries are represented by several surfaces with distinct curvatures, for example in the wheel-rail case. A considerable improvement for the method would be achieved by employing the same techniques presented in the ongoing research by Gay Neto [79]. The proposal is to employ an optimization scheme based on trust region methods. This kind of enhancement is expected for future works.

Another point to observe is the need of combining the master-surface to master-surface contact formulation with tangential constitutive laws other than the Coulomb's one. This kind of improvement is of fundamental importance for studying railway systems because creep phenomenon plays a crucial role in this field. However, as presented in this work, the models as developed here can be employed in

preliminary studies satisfactorily. In the early stage of such kind of study, tangential penalty factors can be calibrated to approximate a kind of linear creepage, still using the Coulomb's friction law as a saturation limit for friction.

While developing the railway examples in this work, it was identified the need of formulating an element to represent the suspension system of the railway vehicle. It is a challenging problem since this element must provide the user with the capability of defining stiffness and damping for six degrees of freedom. Moreover, the user has to be able to defined rigid or free behaviour for some directions, if needed. Finite rotations and Rodrigues rotation parameters have to be considered in the formulation to ensure compatibility with all the other developments.

As a conclusion, although some limitations were identified and discussed here, the models developed in this work (also presented in [67]) can be viewed as important contributions to the field of computational mechanics and multibody dynamics based on finite element methods. By author's knowledge, such kind of rigid body element that considers a generic pole position, with finite rotations described by Rodrigues parameters and with the possibility of establishing contact with other rigid or flexible bodies, has not been published by other authors.

A. APPENDIX: VECTORS AND TENSORS

In this appendix, the main mathematical properties used throughout this work are summarized.

The skew-symmetric operator is defined by:

$$\mathbf{A} = \text{skew}(\mathbf{a}) = \begin{bmatrix} 0 & -a_3 & a_2 \\ a_3 & 0 & -a_1 \\ -a_2 & a_1 & 0 \end{bmatrix}, \quad (\text{A.1})$$

where \mathbf{a} is the axial vector given by $[a_1 \ a_2 \ a_3]^T$.

Skew-symmetric tensors have the following properties:

$$\mathbf{A}^T = -\mathbf{A} \text{ and}$$

$$-\mathbf{A}^T = \mathbf{A}. \quad (\text{A.2})$$

This operator provides means of writing the cross-product between two vectors in a matrix form:

$$\mathbf{a} \times \mathbf{b} = \mathbf{A}\mathbf{b} = -\mathbf{B}\mathbf{a}, \quad (\text{A.3})$$

where $\mathbf{B} = \text{skew}(\mathbf{b})$.

Some useful properties of the cross product are listed below:

$$\mathbf{a} \times \mathbf{b} = -\mathbf{b} \times \mathbf{a},$$

$$\mathbf{a} \times (\mathbf{b} + \mathbf{c}) = \mathbf{a} \times \mathbf{b} + \mathbf{a} \times \mathbf{c}, \quad (\text{A.4})$$

$$\mathbf{a} \times (\mathbf{b} \times \mathbf{c}) = \mathbf{b}(\mathbf{a} \cdot \mathbf{c}) - \mathbf{c}(\mathbf{a} \cdot \mathbf{b}).$$

Some useful properties of the dot product are listed below:

$$\mathbf{a} \cdot \mathbf{b} = \mathbf{b} \cdot \mathbf{a},$$

$$\mathbf{a} \cdot (\mathbf{b} + \mathbf{c}) = \mathbf{a} \cdot \mathbf{b} + \mathbf{a} \cdot \mathbf{c}, \tag{A.5}$$

$$\mathbf{a} \cdot \mathbf{b} = \mathbf{a}^T \mathbf{b} = \mathbf{b}^T \mathbf{a}.$$

The following property can be useful when triple products appear:

$$\mathbf{a} \cdot (\mathbf{b} \times \mathbf{c}) = \mathbf{b} \cdot (\mathbf{c} \times \mathbf{a}) = \mathbf{c} \cdot (\mathbf{a} \times \mathbf{b}). \tag{A.6}$$

Some properties of derivatives involving vectors can also be useful:

$$\frac{d(\mathbf{a}(t) \cdot \mathbf{b}(t))}{dt} = \mathbf{a}(t) \cdot \frac{d\mathbf{b}(t)}{dt} + \frac{d\mathbf{a}(t)}{dt} \cdot \mathbf{b}(t),$$

$$\frac{d(\mathbf{a}(t) \times \mathbf{b}(t))}{dt} = \mathbf{a}(t) \times \frac{d\mathbf{b}(t)}{dt} + \frac{d\mathbf{a}(t)}{dt} \times \mathbf{b}(t), \tag{A.7}$$

$$\frac{d(\|\mathbf{a}(t)\|)}{dt} = \frac{\left(\frac{d\mathbf{a}(t)}{dt} \cdot \mathbf{a}(t)\right)}{\|\mathbf{a}(t)\|}.$$

An orthogonal matrix is a matrix that presents the following properties:

$$\mathbf{Q}^T = \mathbf{Q}^{-1} \text{ and}$$

$$\mathbf{Q}^T \mathbf{Q} = \mathbf{I}, \tag{A.8}$$

where \mathbf{I} is the identity matrix.

It is also interesting to remember that the following rules applies to matrices:

$$(\mathbf{F}^T)^T = \mathbf{F},$$

$$(\mathbf{FG})^T = \mathbf{G}^T \mathbf{F}^T.$$

(A.9)

B. APPENDIX: RODRIGUES ROTATION TENSOR

To write the rotation tensor, there are many possible approaches. Particularly, for the present work we are going to use the rotation description by the Rodrigues rotation vector. To define that, let θ_k be the magnitude of the Euler rotation vector, associated with the deformation experienced by a generic material point P_k . With that, one can define the classical Euler rotation vector by $\boldsymbol{\theta}_k = \theta_k \mathbf{e}_k$, where \mathbf{e}_k is a unit-vector, describing the direction of rotation axis. The Rodrigues rotation vector is defined by $\boldsymbol{\alpha}_k = \alpha_k \mathbf{e}_k$, where $\alpha_k = 2 \tan(\theta_k/2)$. With that, one can write the following expression for the rotation tensor:

$$\mathbf{Q}_k = \mathbf{I} + \frac{4}{4+\alpha_k^2} \left(\mathbf{A}_k + \frac{1}{2} \mathbf{A}_k^2 \right), \quad (\text{B.1})$$

where $\mathbf{A}_k = \text{skew}(\boldsymbol{\alpha}_k)$ (this rotation parameter was employed in several works, such as, [18], [71], [80], [69] and [77], which are all examples of Rodrigues' description of finite rotations applied to beam and shell elements). The definition of the Rodrigues rotation parameter as here used implies in singularities for rotations $\theta_k = \pm\pi$. Then, when handling general rigid body movements, rotations approaching such magnitude or larger may be common and represent a limitation. In order to overcome that, we have made a choice of an updated Lagrangian scheme.

BIBLIOGRAPHY

- [1] A. A. SHABANA, "Flexible multibody dynamics: Review of past and recent developments," *Multibody System Dynamics*, vol. 1, pp. 189-222, 1997.
- [2] M. A. PUSO, "An energy and momentum conserving method for rigid–flexible body dynamics," *Int. J. Numer. Meth. Engng*, vol. 53, p. 1393–1414, 2002.
- [3] B. GÖTTLICHER and K. SCHWEIZERHOF, "Analysis of flexible structures with occasionally rigid parts under transient loading," *Computers and Structures*, vol. 83, pp. 2035-2051, 2005.
- [4] W. SCHIEHLEN, "Multibody system dynamics: Roots and perspectives," *Multibody System Dynamics*, vol. 1, pp. 149-188, 1997.
- [5] P. EBERHARD and W. SCHIEHLEN, "Computational dynamics of multibody systems: History, formalisms, and applications," *J. Comput. Nonlinear Dynam*, vol. 1, pp. 3-12, 2005.
- [6] T. M. WASFY and A. K. NOOR, "Computational strategies for flexible multibody systems," *Appl Mech Rev*, vol. 56, pp. 553-613, 2003.
- [7] A. A. SHABANA, *Dynamics of multibody systems*, New York: Cambridge University Press, 2005.
- [8] J. G. DE JALÓN and E. BAYO, *Kinematic and dynamic simulation of multibody systems The real-time challenge*, New York: Springer-Verlag, 1994.
- [9] Dassault Systemes Deutschland GmbH, "SIMPACK," [Online]. Available: <http://www.simpack.com/>. [Accessed 24 07 2017].
- [10] R. SCHWERTASSEK, O. WALLRAPP and A. A. SHABANA, "Flexible multibody simulation and choice of shape functions," *Nonlinear Dynamics*, vol. 20, pp. 361-380, 1999.
- [11] S. DIETZ, O. WALLRAPP and S. WIEDEMANN, "Nodal vs. modal representation in flexible multibody system dynamics," *Multibody Dynamics*, 2003.
- [12] M. GÉRADIN and A. CARDONA, *Flexible multibody dynamics a finite element approach*, John Wiley & Sons, LTD, 2001.

- [13] D. J. BENSON and J. O. HALLQUIST, "A simple rigid body algorithm for structural dynamics programs," *International Journal for Numerical Methods in Engineering*, vol. 22, pp. 723-749, 1986.
- [14] A. IBRAHIMBEGOVIĆ and S. MAMOURI, "On rigid components and joint constraints in nonlinear dynamics of flexible multibody systems employing 3D geometrically exact beam model," *Comput. Methods Appl. Mech. Engrg.*, vol. 188, pp. 805-831, 2000.
- [15] O. BAUCHAU, J. Y. CHOI and C. L. BOTTASSO, "On the modeling of shells in multibody dynamics," *Multibody Systems Dynamics*, vol. 8, pp. 459-489, 2002.
- [16] O. A. BAUCHAU, C. L. BOTTASSO and Y. G. NIKISHKOV, "Modeling rotorcraft dynamics with finite element multibody procedures," *Mathematical and Computer Modelling*, vol. 33, pp. 1113-1137, 2001.
- [17] P. BETSCH and N. SÄNGER, "On the use of geometrically exact shells in a conserving framework for flexible multibody dynamics," *Comput. Methods Appl. Mech. Engrg.*, vol. 198, pp. 1609-1630, 2009.
- [18] A. GAY NETO, "Simulation of mechanisms modeled by geometrically-exact beams using Rodrigues rotation parameters," *Comput. Mech.*, 2016.
- [19] P. WRIGGERS, *Computational contact mechanics*, 2 ed., New York: Springer-Verlag Berlin Heidelberg, 2006.
- [20] A. KONYUKHOV and K. SCHWEIZERHOF, "On some aspects for contact with rigid surfaces: Surface-to-rigid surface and curves-to-rigid surface algorithms," *Comput. Methods Appl. Mech. Engrg.*, vol. 283, pp. 74-105, 2014.
- [21] J. PFISTER and P. EBERHARD, "Frictional contact of flexible and rigid bodies," *Granular Matter*, vol. 4, pp. 25-36, 2002.
- [22] F. PFEIFFER and C. GLOCKER, *Multibody dynamics with unilateral contacts*, Wiley-VCH Verlag GmbH & Co. KGaA, 2004.
- [23] G. HIPPMANN, "An algorithm for compliant contact between complexly shaped surfaces in multibody dynamics," *Multibody Syst Dyn*, vol. 12, pp. 345-362, 2003.
- [24] J. A. C. AMBRÓSIO, "Impact of rigid and flexible multibody systems: Deformation description and contact models," *Schiehlen W., Valášek M. (eds) Virtual Nonlinear Multibody Systems. NATO ASI Series (Series II: Mathematics, Physics and Chemistry)*, vol. 103, 2003.
- [25] M. C. LIN and S. GOTTSCHALK, "Collision detection between geometric models: a survey," University of North Carolina., 1998.

- [26] X. LIM and T. NG, "Contact detection algorithms for three-dimensional ellipsoids in discrete element modelling," *Int. J. for Numerical and Analytical Methods in Geomechanics*, vol. 19, pp. 653-659, 1995.
- [27] C. WELLMANN, C. LILLIE and P. WRIGGERS, "A contact detection algorithm for superellipsoids based on the common-normal concept," *Engineering Computations: International Journal for Computer-Aided Engineering and Software*, vol. 25, pp. 432-442, 2008.
- [28] T. SHINAR, C. SCHROEDER and R. FEDKIW, "Two-way coupling of rigid and deformable bodies," *Eurographics/ ACM SIGGRAPH Symposium on Computer Animation*, 2008.
- [29] A. GAY NETO, P. M. PIMENTA and P. WRIGGERS, "A master-surface to master-surface formulation for beam to beam contact. Part I: frictionless interaction," *Comput. Methods Appl. Mech. Engrg.*, vol. 303, pp. 400-429, 2016.
- [30] A. GAY NETO, P. M. PIMENTA and P. WRIGGERS, "A master-surface to master-surface formulation for beam to beam contact. Part II: frictional interaction," *Comput. Methods Appl. Mech. Engrg.*, vol. 319, pp. 146-174, 2017.
- [31] J. L. ESCALONA, H. SUGIYAMA and A. A. SHABANA, "Modelling of structural flexibility in multibody railroad vehicle systems," *Vehicle System Dynamics*, vol. 51, no. 7, pp. 1027-1058, 2013.
- [32] I. KAISER and K. POPP, "Interaction of elastic wheelsets and elastic rails: modelling and simulation," *Vehicle System Dynamics*, vol. 44, pp. 932-939, 2006.
- [33] N. CHAAR, Wheelset structural flexibility and track flexibility in vehicle-track dynamic interaction - Doctoral thesis, Stockholm, 2007.
- [34] S. ZHONG, X. W. Z. XIAO and X. JIN, "Effect of wheelset flexibility on wheel-rail contact behavior and a specific coupling of wheel-rail contact to flexible wheelset," *Acta Mech. Sin.*, vol. 32, pp. 252-264, 2016.
- [35] S. ZHONG, J. XIONG, X. W. Z. XIAO and X. JIN, "Effect of the first two wheelset bending modes on wheel-rail contact behavior," *Journal of Zhejiang University-SCIENCE A (Applied Physics & Engineering)*, vol. 15, pp. 984-1001, 2014.
- [36] A. GAY NETO, "A computational tool to simulate dynamics of mechanical systems," [Online]. Available: <http://sites.poli.usp.br/p/alfredo.gay/GIRAFFE.pdf>. [Accessed 31 10 2017].
- [37] A. GAY NETO, "Giraffe User's Manual v.1.0.200 – Generic Interface Readily Accessible for Finite Elements," 6 2017. [Online]. Available: http://sites.poli.usp.br/p/alfredo.gay/GIRAFFE_manual.pdf. [Accessed 31 10 2017].

- [38] J. KORELC and P. WRIGGERS, *Automation of finite element methods*, Springer, 2016.
- [39] H. TOURNAY, "The Fundamentals of Vehicle/Track Interaction," in *Guidelines to best practices for heavy haul railway operations: Management of the wheel and rail Interface*, Virginia, Simmons-Boardman Books, Inc., 2015.
- [40] A. ORLOVA and Y. BORONENKO, "The anatomy of railway vehicle running gear," in *Handbook of railway vehicle dynamics*, S. IWNICKI, Ed., Manchester, CRC Press, 2006.
- [41] T. DAHLBERG, "Track issues," in *Handbook of railway vehicle dynamics*, S. IWNICKI, Ed., Manchester, CRC Press, 2006.
- [42] A. A. SHABANA, K. E. ZAAZAA and H. SUGIYAMA, *Railroad vehicle dynamics a computational approach*, Boca Raton: CRC Press, 2007.
- [43] A. H. WICKENS, "A history of railway vehicle dynamics," in *Handbook of Railway Vehicle Dynamics*, S. IWNICK, Ed., Manchester, CRC Press, 2006.
- [44] J. B. AYASSE and H. CHOLLET, "Wheel-rail contact," in *Handbook of railway vehicle dynamics*, S. IWNICKI, Ed., Manchester, CRC Press, 2006.
- [45] R. LEWIS and U. OLOFSSON, "Basic tribology of the wheel-rail contact," in *Wheel-rail interface handbook*, R. LEWIS and U. OLOFSSON, Eds., Boca Raton, CRC Press, 2009.
- [46] J. J. KALKER, *Three-dimensional elastic bodies in rolling contact*, vol. 2, G. M. L. GLADWELL, Ed., Delft: Springer-Science + Business Media, 1990.
- [47] O. POLACH, M. BERG and S. IWNICKI, "Simulation," in *Handbook of railway vehicle dynamics*, S. IWNICKI, Ed., Manchester, CRC Press, 2006.
- [48] S. IWNICKI, *The manchester benchmarks for rail vehicle simulation*, Boca Raton: CRC, 1999.
- [49] VORtech b.v., "Kalker software," VORtech b.v., [Online]. Available: <https://www.kalkersoftware.org/>. [Accessed 31 10 2017].
- [50] J. J. KALKER, "The computation of three-dimensional rolling contact with dry friction," *Int. Journ. for Numerical Methods in Engineering*, vol. 14, p. 1293–1307, 1979.
- [51] P. H. JOST, "Tribology - Origin and future," *Wear*, vol. 136, pp. 1-17, 1990.
- [52] I. M. HUTCHINGS, *Tribology: Friction and wear of engineering materials*, Cambridge: Butterworth Heinemann, 1992.
- [53] D. E. JONES and G. A. SCHOTT, *Miscellaneous papers: By Heinrich Hertz*, London: Macmillan, 1896.

- [54] K. L. JOHNSON, Contact mechanics, Cambridge: Cambridge University Press, 1987.
- [55] T. A. LAURSEN, Computational contact and impact mechanics: Fundamentals of modeling interfacial phenomena in nonlinear finite element analysis, New York: Springer-Verlag Berlin Heidelberg GmbH, 2003.
- [56] V. A. YASTREBOV, Numerical methods in contact mechanics, P. Breitkopf, Ed., New Jersey: John Wiley & Sons, Inc., 2013.
- [57] A. KONYUKHOV and K. SCHWEIZERHOF, Computational contact mechanics: Geometrically exact theory for arbitrary shaped bodies, New York: Springer-Verlag Berlin Heidelberg, 2013.
- [58] K. J. BATHE, Finite element procedures, New Jersey: Prentice Hall, 1996.
- [59] P. WRIGGERS, Non linear finite element methods, Springer-Verlag Berlin Heidelberg, 2008.
- [60] E. A. WILSON and B. PARSONS, "Finite element analysis of elastic contact problems using differential displacements," *International Journal for Numerical Methods in Engineering*, vol. 2, pp. 387-395, 1970.
- [61] S. K. CHAN and I. S. TUBA, "A finite element method for contact problems of solids bodies - Part I. Theory and validation," *Int. J. mech. Sci.*, vol. 13, pp. 615-625, 1971.
- [62] A. FRANCAVILLA and O. C. ZIENKIEWICZ, "A note on numerical computations of elastic contact problems," *International Journal for Numerical Methods in Engineering*, vol. 9, pp. 913-924, 1975.
- [63] J. T. STADTER and R. O. WEISS, "Analysis of contact through finite element GAPS," *Computers & Structures*, vol. 10, pp. 867-873, 1979.
- [64] P. WRIGGERS and J. C. SIMO, "A note on tangent stiffness for fully nonlinear contact problems," *Communications in Applied Numerical Methods*, vol. 1, pp. 199-203, 1985.
- [65] P. WRIGGERS and G. ZAVARISE, "On contact between three-dimensional beams undergoing large deflections," *Commun. Numer. Methods Eng.*, vol. 13, pp. 429-438, 1997.
- [66] P. WRIGGERS and G. ZAVARISE, "Contact with friction between beams in 3-D space," *Internat. J. Numer. Methods Engrg.*, vol. 49, pp. 977-1006, 2000.
- [67] P. R. REFACHINHO DE CAMPOS and A. GAY NETO, "Rigid body formulation in a finite element context with contact," *Comput Mech*, pp. 1-30, 2018.
- [68] H. BARUH, Analytical dynamics, WCB/McGraw-Hill, 1999.

- [69] P. M. PIMENTA and E. M. B. CAMPELLO, "Geometrically nonlinear analysis of thin-walled space frames," in *Proceedings of the second European conference on computational mechanics, II ECCM*, Krakow, 2001.
- [70] J. M. GOICOLEA and J. C. G. ORDEN, "Dynamic analysis of rigid and deformable multibody systems with penalty methods and energy-momentum schemes," *Comput. Methods Appl. Mech. Engrg.*, vol. 188, pp. 789-804, 2000.
- [71] A. GAY NETO, "Dynamics of offshore risers using a geometrically-exact beam model with hydrodynamic loads and contact with the seabed," *Engineering Structures*, vol. 125, pp. 438-454, 2016.
- [72] A. GAY NETO, P. M. PIMENTA and P. WRIGGERS, "Contact between spheres and general surfaces," *Comput. Methods Appl. Mech. Engrg.*, 2017.
- [73] P. R. R. DE CAMPOS, D. N. HIGA and A. GAY NETO, "Lateral stability of railway vehicles and new contact formulations," in *Proceedings of the XXXVIII Iberian Latin-American Congress on Computational Methods in Engineering*, Florianópolis, 2017.
- [74] H. LEIPHOLZ, *Stability theory*, 2 ed., Stuttgart: Springer Fachmedien Wiesbaden, 1987.
- [75] T. WRIGHT, "The contact patch: Transport technology from the ground up," [Online]. Available: <http://the-contact-patch.com/book/rail/r0418-hunting>. [Accessed 12 11 2017].
- [76] A. H. WICKENS, *Fundamentals of rail vehicle dynamics: Guidance and stability.*, Lisse: Swets & Zeitlinger Publishers, 2005.
- [77] N. S. N. OTA, L. WILSON, A. GAY NETO, S. PELLEGRINO and P. M. PIMENTA, "Nonlinear dynamic analysis of creased shells," *Finite Elements in Analysis and Design*, vol. 121, pp. 64-74, 2016.
- [78] J. C. SIMO and K. K. WONG, "Unconditionally stable algorithms for rigid body dynamics that exactly preserve energy and momentum," *Int. J. Numer. Meth. Engng.*, vol. 31, pp. 19-52, 1991.
- [79] A. GAY NETO, "Modelagem computacional do contato pontual entre corpos: Uma visão integrada," in *Tese (Livre-Docência) - Escola Politécnica da Universidade de São Paulo*, São Paulo, 2018, p. 310.
- [80] P. M. PIMENTA, E. M. B. CAMPELLO and P. WRIGGERS, "An exact conserving algorithm for nonlinear dynamics with rotational dof's and general hyperelasticity. Part 1: rods," *Comput Mech*, vol. 42, pp. 715-732, 2008.